



University of  
Massachusetts  
Amherst

## Synthesis and Biological Applications of Heavy-Metal-Free Semiconductor Nanocrystals

Item Type	Dissertation (Open Access)
Authors	Qi, Ying
DOI	<a href="https://doi.org/10.7275/6957033.0">10.7275/6957033.0</a>
Download date	2026-06-08 09:04:02
Link to Item	<a href="https://hdl.handle.net/20.500.14394/19602">https://hdl.handle.net/20.500.14394/19602</a>

**SYNTHESIS AND BIOLOGICAL APPLICATIONS OF HEAVY-METAL-FREE  
SEMICONDUCTOR NANOCRYSTALS**

A Dissertation Presented

by

YING QI

Submitted to the Graduate School of the  
University of Massachusetts Amherst in partial fulfillment  
of the requirements for the degree of  
**DOCTOR OF PHILOSOPHY**  
May 2015  
Department of Chemical Engineering

© Copyright by Ying Qi 2015

All Rights Reserved

**SYNTHESIS AND BIOLOGICAL APPLICATIONS OF HEAVY-METAL-FREE  
SEMICONDUCTOR NANOCRYSTALS**

A Dissertation Presented

by

YING QI

Approved as to style and content by:

---

T. J. Mountziaris, Chair

---

Wei Fan, Member

---

Jessica D. Schiffman, Member

---

Harry Bermudez, Member

---

John Collura, Interim Head  
Department of Chemical Engineering

## **DEDICATION**

To my dear husband, my son and my parents. They make me who I am.

## ACKNOWLEDGMENTS

First I would like to thank my advisor Professor T. J. Mountziaris. He opened the door of nanomaterial to me and guided me through the wonderful journey of my PhD. I am deeply grateful to his support and the wise advices he gave me in every aspect of research and life, they are the great treasure to me.

I would like to thank my committee members, Professor Harry Bermudez, Professor Wei Fan and Professor Jessica Shiffmann, for their generous advices on my thesis proposal and thesis research.

I am grateful to my lab mates: Dr. Jun Wang, Dr. Ryan Reeves, and Dr. Tracy Panzarella, they helped me on variety of projects and gave me lots of great advice.

I would like to thank Professor Christopher Salthouse and Hongtao wang for their collaboration in the fluorescence lifetime measurement of biosensor.

I thank to Professor Curt Conner, Professor Pablo Visconti and Professor James Watkins for allowing my access to various instruments.

I thank to Jack Hirsch, Louis Roboin, Volodymyr Duzhko, for their assistant in material characterization.

I thank to Dauenhauer group, Fan group, Dimitrakopoulos group and Huber group for their help in experiments and sharing lab utensils. Also I thank to Maroudas group, Schiffman Group for the helpful discussions in different projects.

I am grateful to my Chinese friends in Amherst, together we had many great memories. And they helped me and my family go through the hard times.

I thank to all the graduate students, faculties and staffs in UMass Amherst chemical engineering department. Together they created a friendly environment, and the activities organized by CHEGS made my leisure time in Amherst enjoyable.

Last I would like to thank my beloved husband, who gave me enormous support and cheered me up all the time, my parents who is the strength of my heart, and my son who makes me strong and grateful to life.

## ABSTRACT

### SYNTHESIS AND BIOLOGICAL APPLICATIONS OF HEAVY-METAL-FREE SEMICONDUCTOR NANOCRYSTALS

MAY 2015

YING QI, B.S., TIANJIN UNIVERSITY, CHINA

Ph.D., UNIVERSITY OF MASSACHUSETTS AMHERST

Directed by: Professor T. J. Mountziaris

Semiconductor nanocrystals, also called quantum dots (QDs), are an interesting class of materials exhibiting size-tunable optical properties. QDs are attractive for a variety of applications, such as biological sensing and imaging, high color definition display technologies, and photovoltaics. The most widely studied QDs are compound semiconductors of the type CdX and PbX (with X= S, Se, and Te). The absorption and fluorescence emission wavelengths of these QDs span the visible and near infrared (NIR) regions of the electromagnetic spectrum. However, the highly toxic heavy metals Cd and Pb contained in these materials are problematic for their widespread use in commercial applications. Substitution of the heavy metals with Zn and Sn can yield QDs that are less toxic and more environmentally friendly.

ZnSe QDs are highly luminescent in the UV-blue region of the spectrum and can be engineered to emit at longer wavelengths by doping them with transition metals, such as Mn or Cu. Encapsulation of ZnSe QDs with an inorganic shell, such as ZnS, has been shown to increase their stability and fluorescence intensity (quantum yield). However, the thermodynamic stability of such core/shell particles must be studied to understand the feasibility and long-term stability of atomically-abrupt interfaces between the core and the shell. The thermodynamic stability of ZnSe/ZnTe and ZnTe/ZnSe core/shell QDs was explored in this study. It was found that ZnSe/ZnTe core/shell QDs are thermodynamically more stable than ZnTe/ZnSe core/shell QDs. Functionalization of the surface of the QDs with biomolecules enables their use in biological sensing and imaging applications. A ZnSe-based QD-DNA

biosensor was fabricated and characterized using a novel portable time-domain LED fluorimeter that enables nanosecond fluorescence lifetime measurements.

SnSe QDs that absorb near-infrared (NIR) radiation are attractive nano-materials for applications in photovoltaics, photodetectors and photothermal therapy. A new synthesis method for small-size (< 4nm) SnSe QDs was developed that employs an air-stable tin(II) chloride-oleylamine complex and selenium powder dissolved in trioctylphosphine as the precursors. The growth rate and morphology of the nanocrystals were studied as functions of the processing conditions. Optimal synthesis conditions that allow precise control over the final particle size and prevent particle aggregation were identified. The SnSe QDs were coated with a ZnSe shell, capped with 11-mercaptoundecanoic acid and dispersed in aqueous solution to enable bioconjugation with amino-modified biomolecules for biological applications.

To meet the increasing demand for QDs, the development of new, highly-efficient processes for their synthesis is required. A continuous flow reactor was developed that enables efficient synthesis of ZnSe QDs using microemulsions as templates for controlling both the size and size distribution of the particles. The operating conditions of the reactor were optimized to maximize particle quality and conversion of precursors.

## TABLE OF CONTENT

	page
ACKNOWLEDGMENTS .....	v
ABSTRACT.....	vii
LIST OF TABLES.....	xiv
LIST OF FIGURES .....	xv
CHAPTER	
1. INTRODUCTION .....	1
1.1 Quantum Dots (QDs).....	1
1.2 Applications of QDs .....	2
1.3 Heavy-Metal-Free QDs .....	4
1.4 Synthesis of QDs .....	5
1.4.1 Hot injection method .....	5
1.4.2 Microemulsion Template-assisted Synthesis Method .....	6
1.5 Surface modification of QDs for biological applications .....	8
1.6 Core-shell QDs .....	11
1.7 Overview of Research.....	13
2. THERMODYNAMIC STABILITY OF ZnTe/ZnSe AND ZnSe/ZnTe CORE/SHELL	
QUANTUM DOTS.....	15
2.1 Introduction .....	15
2.2 Experimental Section.....	16

2.2.1 Synthesis of ZnSe/ZnTe core/shell QDs.....	16
2.2.2 Synthesis of ZnTe/ZnSe core/shell QDs.....	16
2.2.3 Synthesis of ZnTe <sub>x</sub> Se <sub>1-x</sub> (0<x<1) alloy QDs .....	16
2.2.4 Characterization.....	17
2.3 Results and discussion .....	17
2.3.1 ZnTe QDs.....	17
2.3.2 ZnSe/ZnTe and ZnTe/ZnSe core/shell QDs.....	18
2.3.3 ZnTe <sub>x</sub> Se <sub>1-x</sub> (0<x<1) ternary alloy QDs .....	19
2.3.4 Thermodynamic stability of ZnSe/ZnTe core/shell QDs and ZnTe/ZnSe core/shell QDs .....	21
2.4 Conclusions .....	29
3. SYNTHESIS OF NEAR-INFRARED (NIR) ABSORBING SnSe QUANTUM DOTS USING AIR-STABLE PRECURSORS.....	30
3.1 Introduction .....	30
3.2 Experimental section .....	32
3.2.1 Synthesis of SnSe QDs .....	32
3.2.2 Capping of SnSe QDs with a ZnSe shell .....	32
3.2.3 Surface modification of SnSe/ZnSe core/shell QDs with MUA.....	33
3.2.4 Characterization .....	33
3.3 Results and discussion .....	33
3.3.1 Choice of precursors .....	33
3.3.2 Characterization of SnSe QDs .....	36

3.3.3 The effects of OLA/TOP molar ratio on the morphology of the SnSe QDs .....	40
3.3.4 The effect of OLA/TOP molar ratio on the nucleation and growth rate of SnSe QDs ..	41
3.3.5 The effect of temperature on the morphology of SnSe QDs.....	44
3.3.6 SnSe/ZnSe core/shell QDs .....	45
3.3.7 Surface modification of SnSe/ZnSe core/shell QDs .....	47
3.4 Conclusions .....	48
4. SYNTHESIS OF ZnSe QUANTUM DOTS IN A CONTINUOUS FLOW REACTOR.....	49
4.1 Introduction .....	49
4.2 Experimental Section.....	51
4.2.1 Counter current packed bed reactor design.....	51
4.2.2 Preparation of the microemulsion .....	52
4.2.2 Reactor Operation and Optimization .....	53
4.2.3 Characterization of ZnSe QDs .....	53
4.3 Results and discussion .....	54
4.3.1 Optical properties of ZnSe QDs synthesized in the continuous flow reactor .....	54
4.3.1 Optimization of operating conditions for reactor startup .....	57
4.3.2 Effect of the packing bead diameter on QD concentration .....	59
4.3.3 Optimization of operating conditions for steady state operation .....	61
4.3.4 Analysis of gas streams using gas chromatography.....	62
4.3.5 Effect of H <sub>2</sub> /H <sub>2</sub> Se Flow Rate on the Emission Intensity of ZnSe QDs.....	63
4.3.6 Effect of Storing Conditions on the Stability of Microemulsion ZnSe QDs .....	63

4.4 Conclusions .....	65
5. PORTABLE TIME-DOMAIN LED FLUORIMETER FOR NANOSECOND FLUORESCENCE LIFETIME MEASUREMENTS .....	66
5.1 Introduction .....	66
5.2 Experimental Section.....	68
5.2.1 Synthesis of ZnSe QDs.....	68
5.2.2 Surface modification of ZnSe QDs with mercaptoudecanoic acid.....	68
5.2.3 Bioconjugation of MUA capped ZnSe QDs with ssDNA .....	68
5.2.4 Hybridization of ZnSe-ssDNA with complimentary ssDNA .....	69
5.2.5 Characterization.....	69
5.3 Results and Discussion .....	70
5.3.1 Fluorescence intensity of MUA capped ZnSe QDs, ZnSe-ssDNA complex and ZnSe- dsDNA complex. ....	70
5.3.2 Photoluminescence lifetime measurement of MUA capped ZnSe QDs, ZnSe-ssDNA complex and ZnSe-dsDNA complex. ....	70
5.4 Conclusions.....	71
6. CONCLUSIONS.....	72
APPENDIX: CONTINUOUS FLOW REACTOR PROCESS FLOW CHART.....	74
BIBLIOGRAPHY .....	75

## LIST OF TABLES

Table	Page
3.1 Summary of reported work on the synthesis of SnSe nanostructures .....	31
3.2 Summary of SnSe QDs synthesis conditions in different cases.....	37

## LIST OF FIGURES

Figure	Page
1.1 Quantum confinement in the ideal system and evolution of the energy via density of states from bulk to zero dimension[2].....	1
1.2 Absorption (upper curves) and emission (lower curves) spectra of four CdSe/ZnS QDsamples. The blue vertical line indicates the 488-nm line of an argon-ion laser, which can be used to efficiently excite all four types of QDs simultaneously [3]. ....	2
1.3 Absorbance (dark grey, blue in the color version) and fluorescence (light grey, green in the color version) spectra of an organic dye (fluorescein isothiocyanate, FITC, left) and a CdSe QD (right) with identical emission wavelengths[11]. ....	3
1.4 Hot-injection method for the synthesis of monodisperse nanoparticles[25]. ....	5
1.5 Ternary phase diagram of the PEO-PPO-PEO/water/p-xylene system[23]. ....	6
1.6 Mechanism of ZnSe QDs formation[23]. ....	7
1.7 Emission spectra of ZnSe QDs using template synthesis method. Template composition: (1) 50 wt% PEO–PPO–PEO, 33 wt% p-xylene, and 17 wt% of 1 M zinc acetate dihydrate in water; (2) 58 wt% PEO–PPO–PEO, 32 wt% p-xylene, and 10 wt% of 1 M zinc acetate dihydrate in water. ....	8
1.8 Methods used to prepare water-soluble QDs. (a,b) QDs cap exchanged with MAA and DHLA, respectively. (c) QDs cap exchanged with silanes to form a shell of silica. (d, e) using hydrophobic interactions with native ligands using phospholipids or amphiphilic polymers[34]. ....	10
1.9 Process for capping QDs surface with negative charge MUA. ....	11
1.10 Photoluminescence (PL) spectra for bare (dashed lines) and ZnS overcoated (solid lines) dots with the following core sizes: (a) 23, (b) 42, (c) 48, and (d) 55 Å in diameter[37].	12
1.11 Schematics of the different heterostructure types. The core is represented by the dark boxes and the shell with the lighter boxes[35]. ....	13
2.1 Band gap alignment of bulk ZnTe and ZnSe material. ....	18
2.2 Normalized PL emission spectra of (a) ZnSe QDs and ZnSe/ZnTe core/shell QDs, and (b) ZnTe QDs and ZnTe/ZnSe core/shell QDs. The red shift in the core/shell samples increases with increasing shell thickness. ....	19

2.3	Band gap energy as a function of Te composition for bulk $ZnTe_xSe_{1-x}$ [46].	20
2.4	Band gap energy as a function of Te/Zn molar ratio in precursor solution for $ZnTe_xSe_{1-x}$ alloy QDs.	21
2.5	TEM image of (a) ZnTe QDs, (b) ZnSe QDs, (c) ZnTe/ZnSe core/shell QDs and (d) ZnSe/ZnTe core/shell QDs.	22
2.6	Peak PL emission wavelength of ZnTe/ZnSe core/shell QDs (squares) and ZnSe/ZnTe core/shell QDs (circles) at different shell growth times.	24
2.7	Peak PL emission wavelength of ZnTe/ZnSe core/shell QDs corresponding to different batches. The amount of Se precursor added is 0.9 mmol for batch 1 and 1.35 mmol for batch 2.	24
2.8	XPS wide-scan spectra of ZnTe/ZnSe core/shell QDs.	26
2.9	(a) XPS-derived relative % of Te atoms in group VI part of the ZnSe/ZnTe core/shell QDs at different growth times. (b) XPS-derived relative % of Se atoms in group VI part of the ZnTe/ZnSe core/shell QDs at different growth times. The squares correspond to two-pot synthesis with intermediate purification of the cores and the circles to one-pot synthesis.	27
2.10	XPS-derived relative % of Te atoms in group VI part of the ZnSe/ZnTe core/shell QDs at different annealing times (circles) and XPS-derived relative % of Se atoms in group VI part of the ZnTe/ZnSe core/shell QDs at different annealing times (square).	29
3.1	X-ray diffraction pattern of a SnSe nanostructure synthesized from tin acetate- stearic acid and TOPSe.	35
3.2	Absorption spectrum of SnSe nanocrystals synthesized from tin acetate-stearic acid and TOPSe.	35
3.3	TEM image of SnSe dendritic structure synthesized from tin acetate-stearic acid and TOPSe.	36
3.4	TEM image and size distribution (inset) of SnSe QDs grown under conditions corresponding to case 1 (Table 1) for 10 minutes after precursor injection.	38
3.5	Absorption spectrum of SnSe QDs dispersed in chloroform. The inset shows a plot of the square of the absorption coefficient versus photon energy and has been used to determine the direct band gap of SnSe QDs. The growth conditions are the same as in Figure 3.4.	39
3.6	X-ray diffraction pattern of SnSe QDs grown under conditions corresponding to case 2 (Table 3.2) and a growth time of 10 min.	39
3.7	TEM images of SnSe samples obtained under growth conditions corresponding to case 1 and case 2 (Table 3.2) at different times after precursor injection. (a) case 1 at 10 min, (b) case 2 at 10 min, (c) case 1 at 20 min, (d) case 2 at 20 min.	40

3.8	The effect of the OLA to TOP molar ratio on the absorption spectra of SnSe QDs grown for 10 min under conditions listed in Table 3.2 (case 1 and case 2). .....	41
3.9	Temporal evolution of the direct band gap of SnSe QDs grown under conditions corresponding to (a) case 1 and (b) case 2 (Table 3.2). For growth times up to 10 min, both samples consist of individual particles. At 20 min, particles in both cases have aggregated, as shown in Fig.3.7. ....	42
3.10	TEM image of SnSe QDs prepared under conditions corresponding to case 3 (Table 3.2) one hour after precursor injection. Lower precursor concentrations than case 1 and 2 and higher OLA/Sn and TOP/Se molar ratios delay particle aggregation. ....	43
3.11	Temporal evolution of the direct band gap energy of SnSe QDs grown under conditions corresponding to case 2 (squares) and case 4 (circles), listed in Table 3.2. Lower precursor concentrations and higher OLA/Sn ratio in case 4 lead to fewer nuclei, resulting in larger particles. ....	44
3.12	TEM image of a SnSe aggregate obtained under conditions corresponding to case 5 (Table 3.2) and growth time of 4 min. Increasing the precursor injection and growth temperature in comparison to case 2 leads to particle aggregation at an earlier growth time. 3.14 Absorption spectra of (1) as-grown SnSe QDs; (2) SnSe QDs annealed at 150 °C for 10min. ....	45
3.13	Absorption spectra of (1) as-grown SnSe QDs dispersed in chloroform and (2) SnSe QDs dispersed in tetrahydrofuran after the ligand exchange process. ....	46
3.14	Absorption spectra of (1) as-grown SnSe QDs; (2) SnSe QDs annealed at 150 °C for 10min. ....	47
3.15	XPS spectrum of SnSe/ZnSe core/shell QDs that are capped with MUA. ....	48
4.1	Schematic representation of mass transfer of H <sub>2</sub> Se gas from the gas phase to a Zn-containing aqueous nanodroplet in the microemulsion-gas synthesis method. ....	51
4.2	(a) Experimental reactor; (b) schematic drawing of the reactor. ....	52
4.3	Absorption spectra of the ZnSe QDs synthesized using the continuous flow reactor. ....	54
4.4	Emission spectra of ZnSe QDs samples taken at different processing times. ....	55
4.5	Absorbance at 355 nm, 370 nm and 400 nm for ZnSe QD loaded microemulsion samples collected at different processing times. ....	56
4.6	Comparison of the time evolution of the absorbance for QDs synthesized using a gas stream flow of 2 sccm and 3 sccm H <sub>2</sub> /H <sub>2</sub> Se. ....	57
4.7	Absorbance at 370 nm as a function of the processing time for the reaction that starts with the blank microemulsion. ....	58

4.8	Absorbance at 370 nm as a function of the processing time for the reaction that start with the ZnSe QDs loaded microemulsion. The flowrate of H <sub>2</sub> Se after establishing continuous flow is 1 sccm and 3sccm. ....	59
4.9	Absorbance at 370 nm as a function of the processing time for samples synthesized in a packed bed reactor containing a uniform size of glass beads with diameter of 3 mm and 2mm. ....	60
4.10	Absorbance at 370 nm as a function of processing time from ZnSe QD-loaded microemulsion samples collected during continuous flow processing. The flow rates of the H <sub>2</sub> /H <sub>2</sub> Se gas streams used are: 1.5 sccm and 2 sccm. ....	61
4.11	(a) GC spectra from gas samples taken from the inlet (solid line) and outlet (dotted line) of the reactor. (b) The zoom in view of the GC spectra. ....	62
4.12	Emission spectra of the sample synthesized under H <sub>2</sub> /H <sub>2</sub> Se flow rate of 1.5 sccm (solid line) and 4 sccm (dotted line). ....	63
4.13	Emission spectra of microemulsion ZnSe QDs before adding NaHCO <sub>3</sub> (solid line) and after adding NaHCO <sub>3</sub> (dotted line) ....	64
5.1	Schematic of the separation free homogeneous immunoassay based on ZnSe QDs[63].	67
5.2	Portable LED Fluorimeter[78] . ....	68
5.3	Absorption spectra of MUA capped ZnSe Qdots dispersed in PBS buffer. ....	69
5.4	Fluorescence emission spectra of MUA capped (1) ZnSe QDs, (2) QDs-ssDNA conjugates, and (3) QD-dsDNA conjugates dispersed in PBS buffer. ....	70
5.5	Fluorescence lifetime of ZnSe QDs capped with MUA, conjugated with ssDNA, and conjugated with dsDNA resulting from hybridization of the ssDNA with complementary free ssDNA target. ....	71

# CHAPTER 1

## INTRODUCTION

### 1.1 Quantum Dots (QDs)

Quantum dots (QDs) are semiconductor nanocrystals with size comparable or smaller than its Bohr exciton radius, which is the average distance between electrons and hole pairs[1]. As the material is confined in three-dimensions, the energy levels lose their continuity and become discrete (Figure 1.1). As a result, the band gap energy of QDs is size-dependent. The band gap absorption and emission shift to smaller wavelength (blue-shift) with the descending size (Figure 1.2).

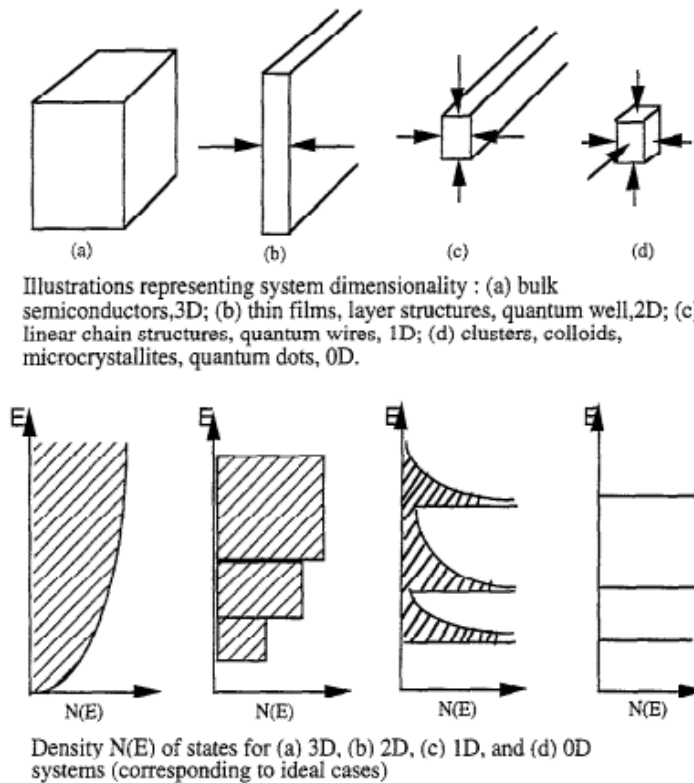


**Figure 1.1: Quantum confinement in the ideal system and evolution of the energy via density of states from bulk to zero dimension[2].**

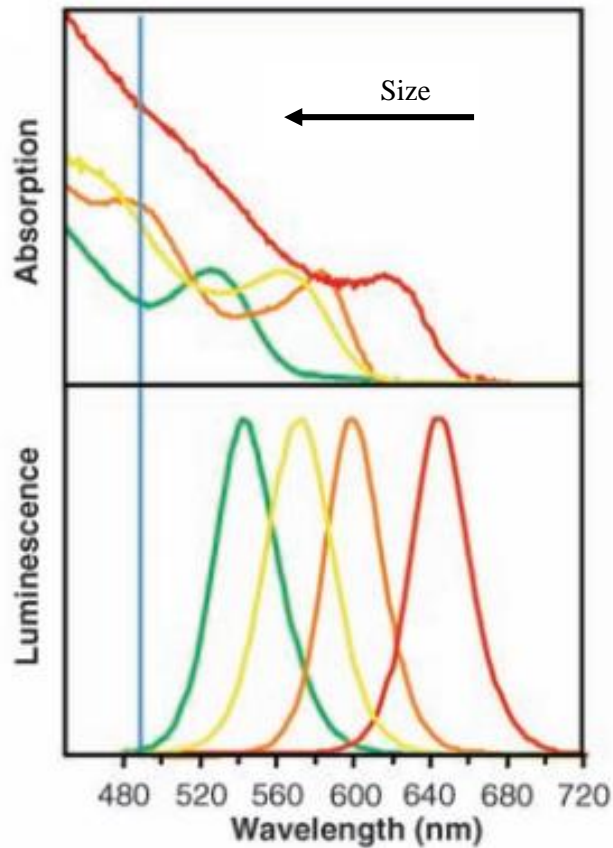


**Figure 1.2: Absorption (upper curves) and emission (lower curves) spectra of four CdSe/ZnS QD samples. The blue vertical line indicates the 488-nm line of an argon-ion laser, which can be used to efficiently excite all four types of QDs simultaneously [3].**

## 1.2 Applications of QDs

The special optical properties of QDs make them useful for a variety of applications. Major TV makers such as Sony[4], LG, Samsung, and TCL[5] have adopted QD-based technology for enhanced color definition in their high-end products. QDs that emit at different colors can be added above the backlight layer on LED TVs, they absorb the blue LED light and emit a richer white light that contains all the colors of the spectrum. This light provides a better picture quality with darker blacks and more vibrant non-blue colors. The energy savings can also be significantly reduced, by eliminating the red and green LEDs and utilizing only a blue LED and QDs emitting red and green colors by absorbing part of the blue light. The other important application of QDs is photovoltaic application. The tunable band gap of QDs is attractive for multi-junction solar cells, where QDs with different band gap energy could be used to

improve power conversion efficiency by harvesting multiple portions of the solar spectrum[6]. QDs can be dispersed as colloidal solution, which enable the simple processing of QDs based solar cell[7]. The QDs can be spun coated on a substrate, and large-scale production could use spray-on or roll-printing systems. The solution processable QDs allow the convenient integration with different substrates and provide an alternative to the expensive thermal process.

QDs have also been used as luminescence tags for biomolecules and offer several advantages over the conventional organic fluorophores. CdSe QDs have broad absorption but narrow and symmetric emission (Figure 1.3), which allows the simultaneously excitation of QDs emitting at different colors. By varying the particle size, morphology and composition of different QDs, their emission and absorption cover the light spectrum from the ultraviolet (UV) to the infrared (IR). Also, the long fluorescence lifetime of QDs can separate their signal from that of shorter lived species, such as background auto-fluorescence in cells. In addition, they resist to both photo and chemical degradation and exhibit quantum yields as high as 90%. With all these unique properties, QDs have gained enormous attention for a variety of applications, such as cellular imaging [8], biosensors[9], and solid state lighting[10].

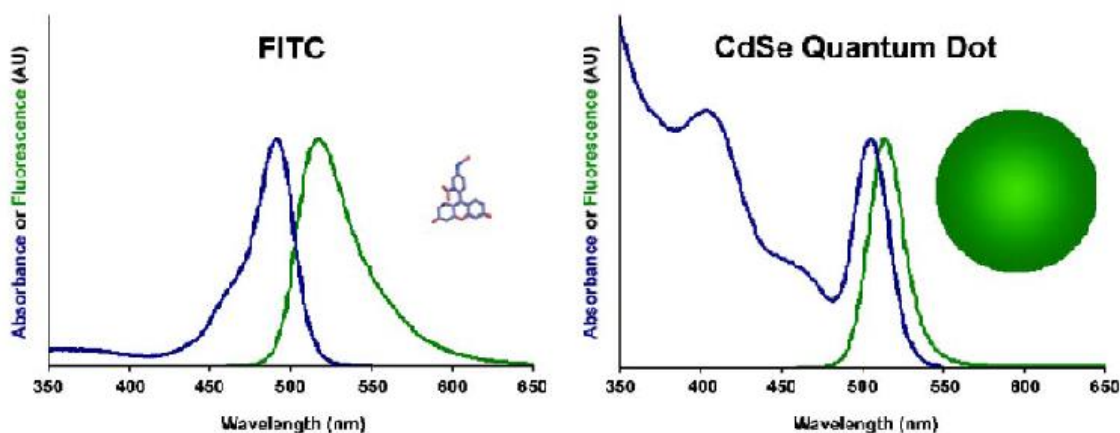


**Figure 1.3: Absorbance (dark grey, blue in the color version) and fluorescence (light grey, green in the color version) spectra of an organic dye (fluorescein isothiocyanate, FITC, left) and a CdSe QD (right) with identical emission wavelengths[11].**

The research on near-infrared (NIR) QDs has grown explosively in the past decade. These nanocrystals absorb/emit NIR light that has the wavelength between 700 and 1400 nm, which corresponds to the band gap of 0.9-1.8 eV. According to the Shockley-Queisser limit [12], the conversion of solar light energy to usable electrical power in solar cells is highest when bandgap energies are in the NIR region. PbS QDs have been dispersed in organic solvents and used in the fabrication of high efficiency solar cells[13]. Another potential application of NIR QDs is photothermal therapy[14], because the biological tissue has a low absorbance in the NIR spectral region. A NIR laser that penetrates deep into tissues can be used to trigger conversion of the incident electromagnetic radiation to heat by the NIR absorbing QDs. NIR absorbing QDs can be engineered to selectively bind cancer cells. The resulting moderate local hyperthermia (41 to 46 °C) can kill the cancer cells, because they are more sensitive to elevated temperatures in comparison to normal cells.

### **1.3 Heavy-Metal-Free QDs**

The most widely studied QDs are CdX and PbX (X= S, Se, Te) materials. Their absorption and emission cover the visible and NIR region of the electromagnetic spectrum. However, the highly toxic heavy metals Cd and Pb limit their biological application. Also, production and waste treatment of these heavy metals are expensive and harmful to the environment. Low toxic Zn- based and Sn-based QDs appear as promising candidates for environmentally friendly applications. ZnSe QDs exhibit intense UV-luminescence because of their relatively large band gap. This unique spectral range restricted their application as they can absorb or emit in a very narrow region of the visible spectrum[15]. Band gap engineering provides multiple choices to broaden their spectral window. In the last decades, different groups have developed various ways of expanding the emission window of Zn-based QDs to the visible range by growing heterogeneous shell[16] and doping with transition metals such as Mn<sup>2+</sup>, Cu<sup>2+</sup> [17]. SnSe QDs belong to the narrow band gap material, with the direct band gap of 1.3 eV and indirect band gap of 0.9 eV[18]. SnSe QDs absorb NIR light and could be potentially used in the application of photovoltaics, NIR photodetectors and photothermal therapy applications.

## 1.4 Synthesis of QDs

### 1.4.1 Hot injection method

There are several techniques for synthesizing QDs, including arrested precipitation[19], vapor-phase synthesis[20], precipitation in the presence of stabilizers[21], hot injection method[22], synthesizing in reverse-micelle[23], and heating up method[24]. Among those methods, the hot injection method produces QDs with the highest quality and narrow size distribution.

The hot injection method was first applied to the synthesis of CdSe QDs[22]. The reaction starts with the fast injection of the cold organometallic precursor to the hot coordinating solvent (300°C), which is critical to obtain the discrete homogeneous nucleation. The subsequent growth of the nuclei is performed under lower temperature, and the ligands in the coordinating solvent prevent particles from growing too fast. The size of the QDs was affected by several factors such as the injection temperature, precursor concentration, precursor ratio, growth time, and the growth temperature. This process enables good control of the size distribution mainly because of the well control of the nucleation and growth process. After injecting the room temperature precursor, the drop of the temperature and the precursor concentration prevents further nucleation. During the growth stage, the population of the small particles would decrease due to Ostwald ripening, where the material in the small particles with higher surface energy would diffuse to larger particles. The synthesis process is schematically shown in Figure 1.4.

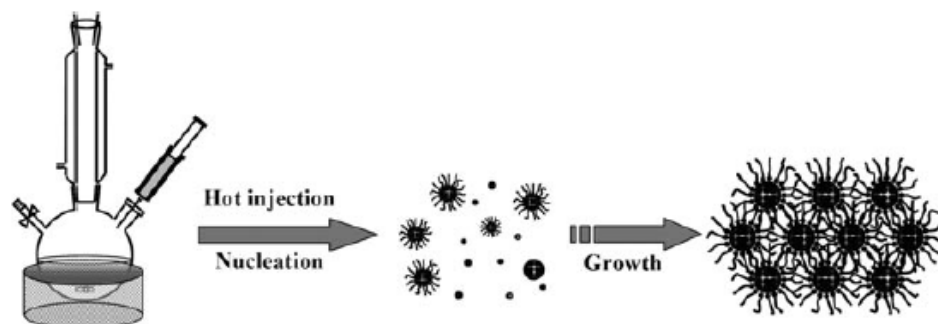
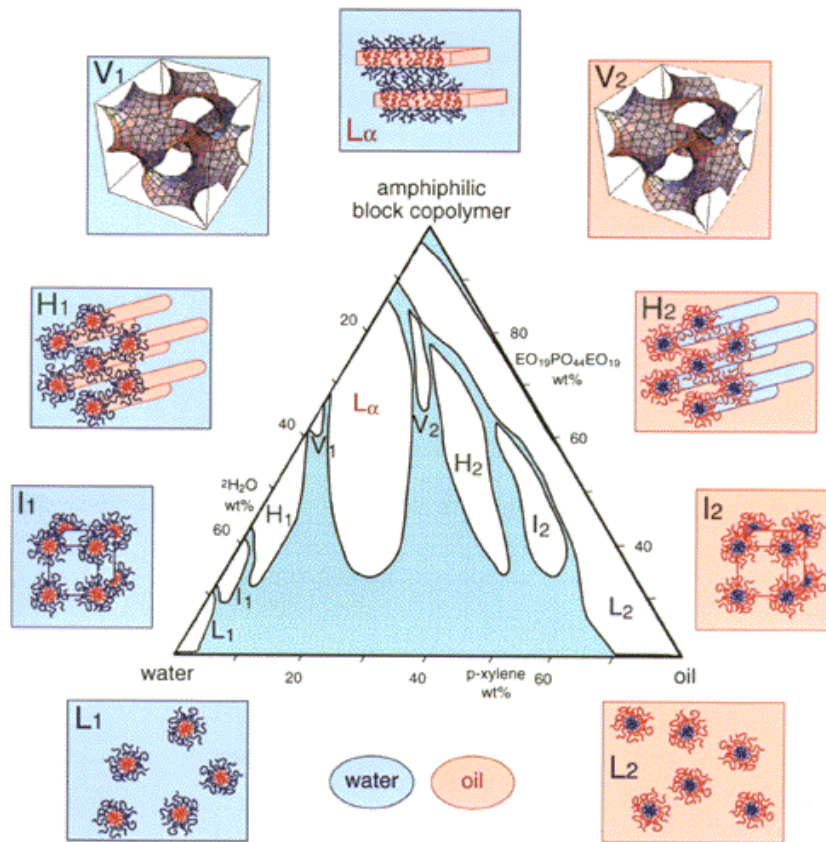


**Figure 1.4: Hot-injection method for the synthesis of monodisperse nanoparticles[25].**

### 1.4.2 Microemulsion Template-assisted Synthesis Method

The traditional hot injection method of synthesizing QDs requires high injection temperatures followed by rapid cooling to separate the nucleation and growth process. This method is difficult to scale up because of the heat transfer and mixing issues. Another method of synthesizing QDs is using microemulsions as template[23]. The microemulsion is formed by the self-assembly of poly(ethylene oxide)–poly(propylene oxide)–poly(ethylene oxide)(PEO–PPO–PEO) amphiphilic block copolymer, water and p-xylene. Figure 1.5 illustrates the phase diagram of the PEO-PPO-PEO/water/p-xylene ternary system. By varying the composition of three components, a variety of thermodynamically stable microstructures, including spherical, cylindrical, planar domains, or interconnected (bi-continuous) topology could be obtained.

**Figure 1.5: Ternary phase diagram of the PEO-PPO-PEO/water/p-xylene system[23].**



To synthesize ZnSe nanostructures, zinc acetate (ZnAc) was dispersed in the aqueous phase, and the microemulsion was brought into contact with H<sub>2</sub>Se gas. The H<sub>2</sub>Se gas diffuses through the continuous p-xylene phase to the aqueous nanodomains and reacts with ZnAc in the aqueous phase irreversibly to form single ZnSe QDs. The size of the ZnSe QDs was controlled by the concentration of the ZnAc in the aqueous phase. The formation process is shown schematically in Figure 1.6.

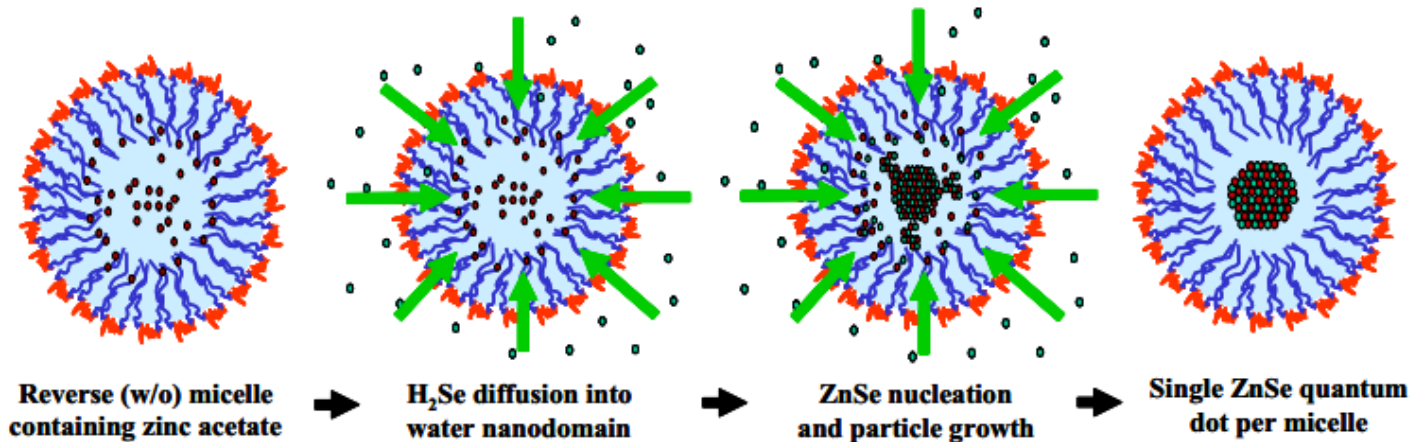
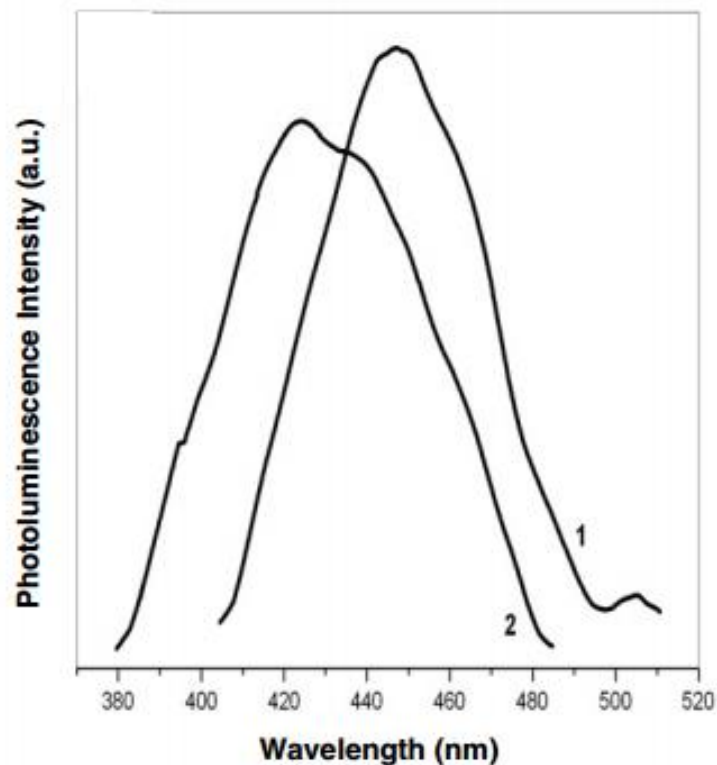


Figure 1.6: Mechanism of ZnSe QD formation[23].

In comparison with the hot injection method, the template synthesis method is much easier to scale up and enables the precise control of the particle size simply by varying the metal salt concentration in the dispersed phase. As shown in Figure 1.6, as the weight percentage of the ZnAc salt increases, the emission spectra shift to larger wavelengths, indicating that the particle size increases. In addition, the template synthesis method uses commercially available precursors other than the pyrophoric and expensive precursors used in the hot injection synthesis method.



**Figure 1.7: Emission spectra of ZnSe QDs using template synthesis method. Template composition: (1) 50 wt% PEO–PPO–PEO, 33 wt% p-xylene, and 17 wt% of 1 M zinc acetate dihydrate in water; (2) 58 wt% PEO–PPO–PEO, 32 wt% p-xylene, and 10 wt% of 1 M zinc acetate dihydrate in water**

### 1.5 Surface modification of QDs for biological applications

QDs synthesized from hot injection method are capped with surfactant such as hexadecylamine (HDA), trioctylphosphine (TOP), oleic acid, etc. The polar head group of those surfactant coordinate with the dangling bond on the QDs surface, while the hydrophobic alkyl tail protrudes outward to protect QDs from aggregation as well as allows them to disperse in the polar solvent. However, the biological application requires the QDs to be water soluble.

Several surface modification strategies have been developed (Figure 1.8). One of the most widely used methods of generating water soluble QDs involves exchange of the hydrophobic surfactant with mercapto ligands [26]. These ligands are easy to make and commercially available. The thiol end anchors to the QDs surface and a hydrophilic end, such as a carboxyl group, would lose a proton and become

negatively charged when the  $\text{pH} > 5$ . QDs functionalized with those ligands repel each other and get dispersed in the aqueous solution. The drawback of this method is the short shelf life and the limited dispersion in acidic solution [27]. The second method of developing more stable water soluble QDs is surface salinization[28]. Mercaptopropyl silanols are used to form a crosslinked shell on the QD surface. The silica shell functionalized with polar groups insulates the QDs from the solvent environment, thus improving the stability of the water soluble QDs. The third method uses amphiphilic polymer[29], where the hydrophobic end of the polymer interacts with the hydrophobic surfactant on top of the QD surface, while the hydrophilic end allows the QDs to disperse in the aqueous environment. Although the second and third methods improve the stability of the water soluble QDs, the final hydrodynamic diameter (HD) of the QDs increases from 4-8 nm to 20-30 nm after the surface modification, which is larger than the HD of the QDs modified using the mercapto ligand exchange method (4.6-16nm)[30, 31]. The large hydrodynamic size of the QDs would limit their intracellular mobility and the application using fluorescence resonance energy transfer (FRET). Furthermore, the complete renal clearance of the QDs require the HD to be less than 5.5 nm[30].

This thesis would focus on the mercapto ligand exchange method as it yields QDs with small HD. There have been several reports on making water soluble CdSe, ZnSe, PbSe, and InP QDs [17, 26, 32, 33] using mercapto ligand exchange method. For a typical ligand exchange process, the QDs are purified from the excess amount of hydrophobic surfactants by adding methanol and hexane, the QDs would precipitate and collected by centrifugation. Then the excess amount of mercapto ligands will be added to the purified QDs to exchange the hydrophobic surfactant left on the surface of QDs. The other end of the mercapto ligand is a carboxyl group, which enables the QDs to be dispersed in polar solvents, such as methanol and tetrahydrofuran. Finally, a certain amount of base would be added to the QDs to deprotonate the carboxyl group, and the QDs with the negative charge surface repel each other and dispersed in water phase. The process is schematically shown in Figure 1.9.

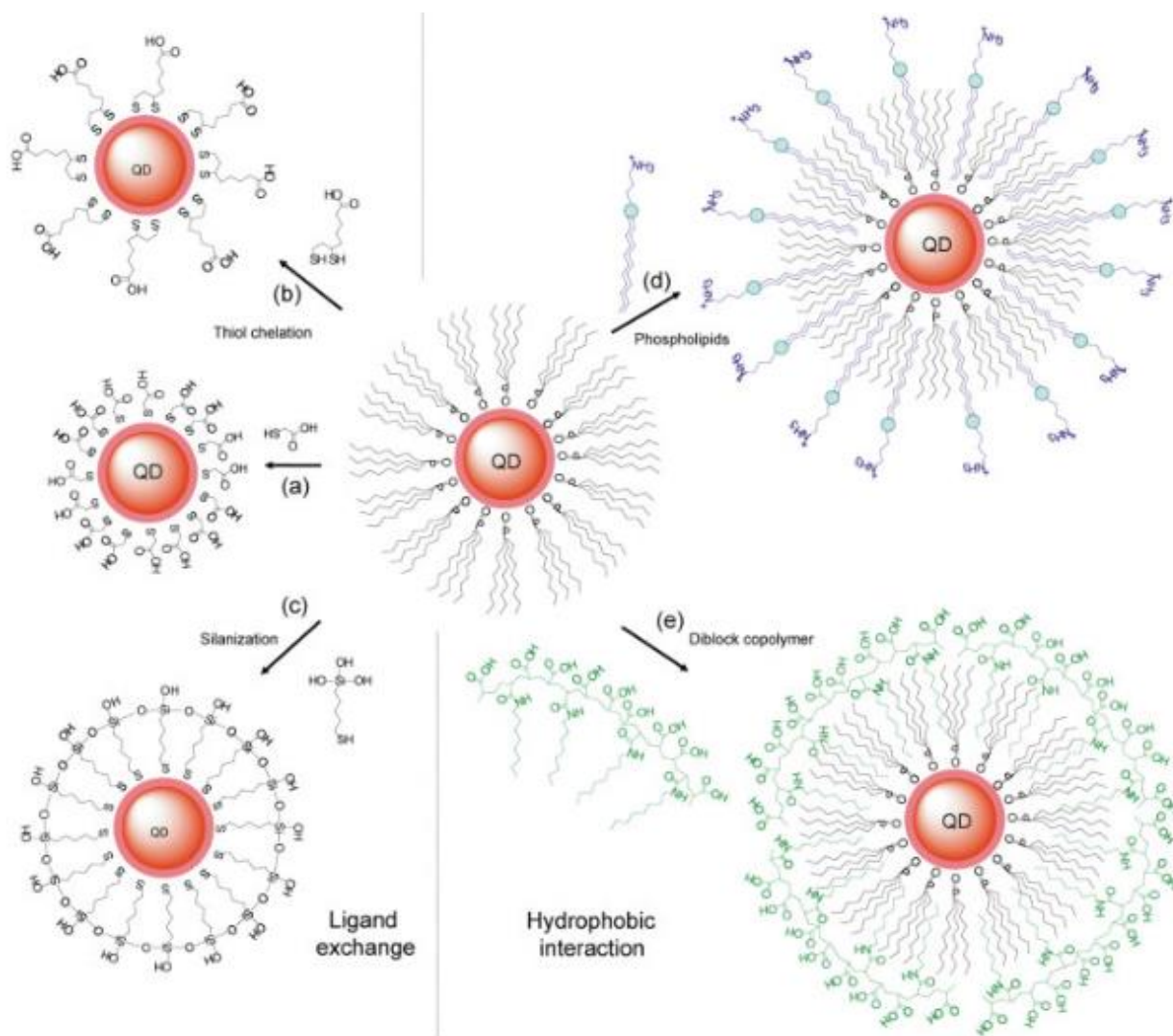


**Figure 1.8: Methods used to prepare water-soluble QDs. (a,b) QDs cap exchanged with MAA and DHLA, respectively. (c) QDs cap exchanged with silanes to form a shell of silica. (d, e) using hydrophobic interactions with native ligands using phospholipids or amphiphilic polymers[34].**

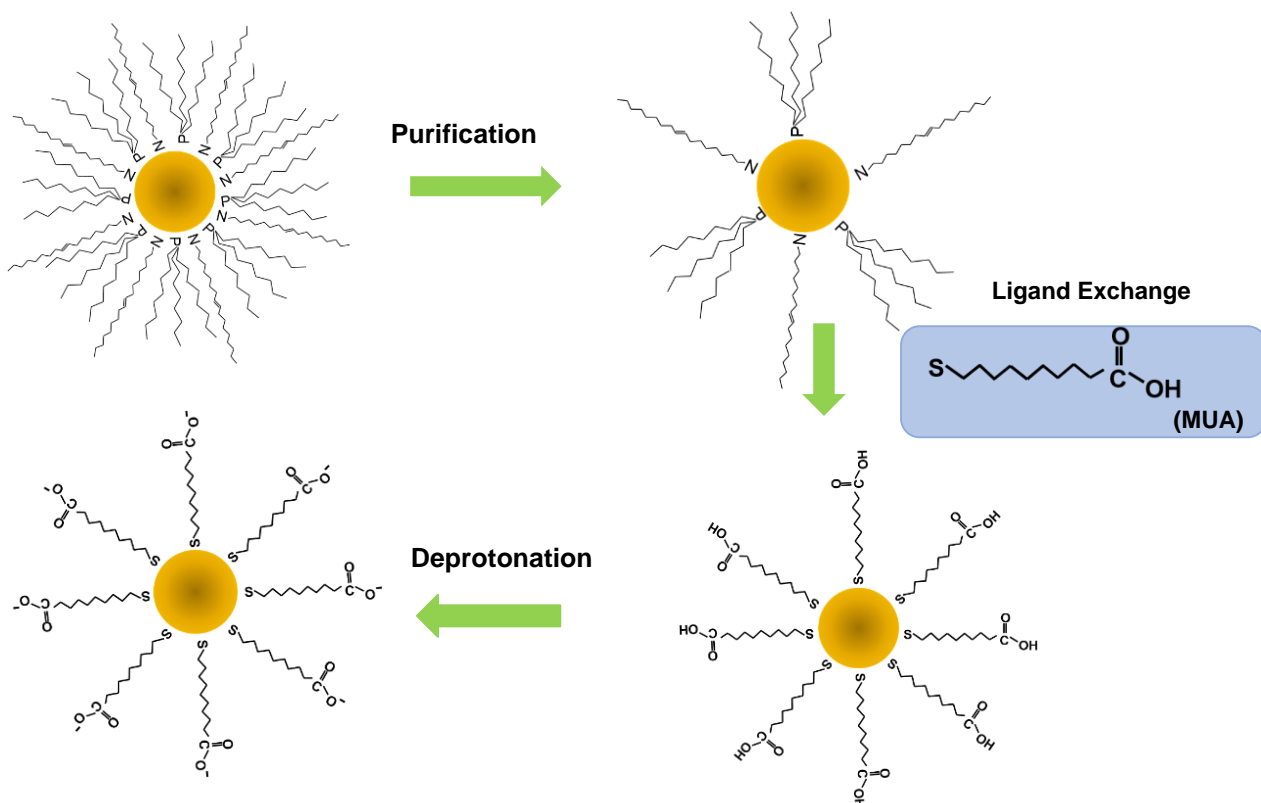


**Figure 1.9: Process for capping QDs surface with negative charge MUA.**

## 1.6 Core-shell QDs

The surface to volume ratio of QDs is very high because of their small size. As a consequence the surface of QDs affects their properties significantly. QDs release photons when an electron directly combines with a hole in the conduction band. Bare core structure cannot achieve high quantum yield and photoluminescent stability when the electrons or holes are trapped in surface states [1]. These surface states are generated from the surface atoms that are not fully incorporated into the lattice. In the hot-injection method, ligands would passivate the QD surface, however, it is not a stable protection as ligands may be desorbed from the surface [35].

Growing inorganic shell structures was demonstrated to provide an effective passivation. For the type I core shell material, the band gap of shell material is larger than that of core material. Consequently, the electrons and holes are confined in the core which effectively eliminates the non-radiative recombination and improves luminescence to a large extent (Figure 1.10). For type-II core-shell structures, both of the conduction band and valence band are lower or higher than that of core structure. So for the holes and electrons of Type-II, one is confined in the core, the other is confined in the shell (Figure 1.11). As a result, the emission wavelength of type II QDs is larger than that of the single material. Type-II core/shell QDs provide the possibility of tuning the band gap by manipulating the shell thickness. It was found that the absorption/emission spectra exhibit red-shift as the shell thickness increases [36].

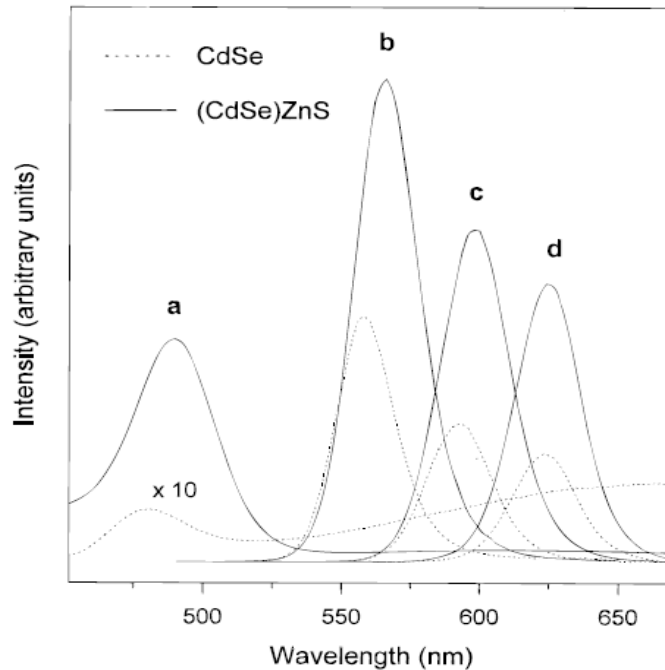


**Figure 1.10: Photoluminescence (PL) spectra for bare (dashed lines) and ZnS overcoated (solid lines) CdSe QDs with the following core sizes: (a) 23, (b) 42, (c) 48, and (d) 55 Å in diameter[37].**

In contrast to the formation mechanism of the core, which is based on homogeneous nucleation, shell growth follows the mechanism of heterogeneous nucleation. Growth temperature, concentration and rate of shell precursor added are critical to the shell formation[35]. The shell growth temperature needs to be carefully controlled. On one hand, it should be low enough to prevent the growth of the core material. On the other hand, the complete deposition of the shell material requires relatively high temperature. The concentration of the shell precursor and the injection rate is also very important. To lower the chance of homogeneous nucleation, the concentration of the shell precursor needs to be controlled at low level. The epitaxial growth of shell is realized by dropwise addition of the precursor. Li et al. [38] developed the Successive Ion Layer Adsorption and Reaction (SILAR) method for the synthesis of QD core/shell structures. In this method, the cationic and anionic precursor is alternatively injected dropwise into the reaction system. Sufficient annealing time after each injection is necessary to allow full deposition of the precursor. The alternate injection reduces the independent nucleation of the shell precursor.

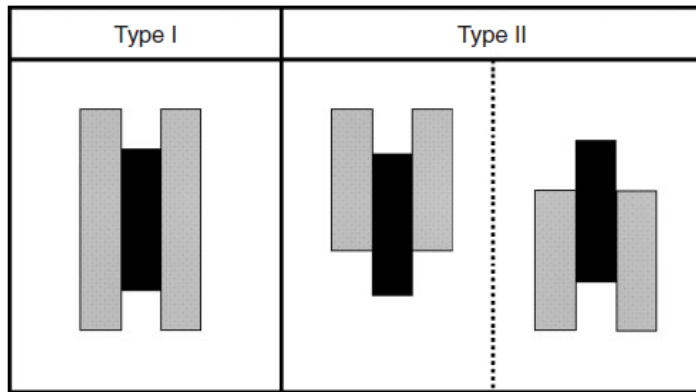


**Figure 1.11: Schematic representation of the band gap structure in Type I and Type II of core/shell QDs. The core is represented by the dark boxes and the shell with the lighter boxes[35].**

## 1.7 Overview of Research

In Chapter 2, the stability of colloidal ZnSe/ZnTe and ZnTe/ZnSe core/shell QDs during shell growth and thermal annealing was explored. The core/shell QDs were synthesized by growing ZnTe or

ZnSe cores first and followed by the deposition of ZnSe or ZnTe shells, respectively. X-ray photoelectron spectroscopy and photoluminescence spectroscopy were employed to investigate the surface composition and optical properties of the core/shell QDs at progressively increasing annealing times.

In Chapter 3 we present a new synthesis method for small size (< 4nm) SnSe QDs that employs an air-stable tin(II) chloride-oleylamine (OLA) complex and selenium powder dissolved in trioctylphosphine (TOP) as precursors. The growth rate and final morphology of the nanocrystals were studied by TEM as functions of the processing conditions. Operating conditions that enable precise control over the final particle size and prevent particle aggregation were identified. The SnSe QDs were further coated with ZnSe shell, which enable them to be modified with 11-mercaptodecanoic acid and dispersed in aqueous phase.

Chapter 4 focuses on the development of a continuous flow reactor for template-assisted synthesis of semiconductor nanocrystals. The growth of ZnSe nanocrystals is used as the example. The reactor startup conditions and the flow rates of the liquid and gas streams were used as variables for optimizing H<sub>2</sub>Se conversion efficiency and enabling steady operation. The effects of process parameters on the optical properties of the synthesized ZnSe QDs were studied.

In Chapter 5 we discuss a results from a collaboration with the group of Professor C. Salthouse of the Electrical and Computer Engineering Department aiming at developing a novel portable time-domain LED fluorimeter. ZnSe-based DNA biosensors consisting of single-stranded DNA (ssDNA) molecules conjugated with a ZnSe QD were constructed and characterized using the new fluorimeter. The biosensors were subsequently hybridized with free complementary ss-DNA and the sensor-target hybridized complexes were characterized. Both fluorescence emission intensity and fluorescence lifetime measurements were performed to study the behavior of the QDs in these biosensors.

## CHAPTER 2

# THERMODYNAMIC STABILITY OF ZnTe/ZnSe AND ZnSe/ZnTe CORE/SHELL QUANTUM DOTS

### 2.1 Introduction

During the synthesis of core/shell QDs, the deposition of an inorganic shell of a compatible semiconductor over core QD typically requires temperatures in the range of 90°C to 300°C. Depending on the processing temperature and materials composition of the core/shell QD, solid-state diffusion may occur that can prevent the formation of an atomically-abrupt interface between the core and shell material during shell growth and post-growth annealing [39, 40]. It has been reported that when the annealing temperature is high (e.g., 300°C), core/shell structures may transform into random alloy structures through solid-state diffusion [41, 42]. It has also been reported that during the synthesis of core/shell Au/CdSe nanoparticles, solid-state diffusion would result in phase segregation [43]. To understand the role of solid-state diffusion in determining the final atomic structure of ternary alloy and core/shell nanocrystals, the equilibrium structures of such materials must be understood. Identifying the most thermodynamically stable structures of ternary QDs is essential for fabricating reliable, high-performance optical and electronic devices. In this part of our work, ZnTe/ZnSe core/shell QDs and ZnSe/ZnTe core/shell QDs were synthesized and the evolution of their atomic structure was monitored as function the growth and annealing time using photoluminescence (PL) and X-ray photoelectron spectroscopy (XPS). The results of our study show that ZnSe/ZnTe core/shell QDs are more stable than ZnTe/ZnSe core/shell ones, thus demonstrating the existence of a thermodynamic driving force that can leads to surface segregation of Te.

## 2.2 Experimental Section

### 2.2.1 Synthesis of ZnSe/ZnTe core/shell QDs

ZnSe QDs were synthesized using the method reported by Hines[15]. The core precursor mixture was prepared by dissolving 0.9 mmol selenium powder and 1.35 mmol diethylzinc ( $\text{Et}_2\text{Zn}$ ) in 2.5 mL trioctylphosphine (TOP). The mixture was injected into 1-hexadecylamine (HDA) kept at  $300^\circ\text{C}$  and the growth temperature was adjusted to  $270^\circ\text{C}$  immediately after precursor injection. After allowing the QDs to grow for 30 minutes, 0.15mmol  $\text{Et}_2\text{Zn}$  was added to the reactor to ensure that the Se precursor was depleted and the growth of ZnSe was terminated. Samples were collected at 10-minute intervals and their PL spectra were compared until no red shift was detected between consecutive samples. Then, the temperature was decreased to  $235^\circ\text{C}$  and a ZnTe shell was grown by adding dropwise 0.45mmol Se and  $\text{Et}_2\text{Zn}$  dispersed in 1.3ml TOP into the reactor over a period of 5 to 7 minutes. Samples were collected from the reactor at specific time intervals and stored for further processing and characterization. For the two-pot synthesis of the core/shell structure, the core QDs were purified by methanol/hexane extraction method and dispersed in hexane. The purified QDs were injected into the hot solvent containing HDA and TOP, and vacuum was applied to evaporate the hexane. The shell growth conditions were kept the same as in the one-pot synthesis.

### 2.2.2 Synthesis of ZnTe/ZnSe core/shell QDs

The synthesis steps used for growing ZnTe/ZnSe core/shell QDs were similar to those used for growing ZnSe/ZnTe QDs. In this case, the Te precursor was injected into the growth solution at  $275^\circ\text{C}$  and the ZnTe cores were grown at  $260^\circ\text{C}$ .

### 2.2.3 Synthesis of $\text{ZnTe}_x\text{Se}_{1-x}$ ( $0 < x < 1$ ) alloy QDs

The reactor containing HDA was heated to  $300^\circ\text{C}$ . In a separate vial, mixtures of selenium and tellurium in TOP were prepared containing different ratios of the two elements to create a total of 1.0

mmol of solution in each case. Then, 1 mL of Et<sub>2</sub>Zn (1 M) was added to the mixture of TOPSe and TOPTe. The resulting precursor solution was quickly injected into the reactor at 300 °C and samples were collected at specific times. An initial drop in temperature to 260 °C occurred due to the injection, but the temperature was quickly adjusted and kept constant at 270 °C during the growth of the nanocrystals.

#### **2.2.4 Characterization**

Samples of the reacting mixture were collected at specific times and dispersed in butanol. The photoluminescence (PL) analysis of the samples was performed using a JOBIN YVON Horiba Fluorolog-3 fluorimeter. The near-surface composition of the nanocrystals was determined by X-ray photoelectron spectroscopy (XPS) using a ThermoElectron ESCALAB 250 spectrometer equipped with a monochromatic Al X-ray source (1486.6 eV) at 49.6W. For the XPS analysis, a purified sample was dispersed in hexane and drop cast on glass slides. The pass energy for the spectra was 46.95 eV.

High-resolution Transmission Electron Microscopy (HR-TEM) was performed using a JEOL 2010F HR-TEM microscope and the images of the QDs were used to determine their average size of QDs. The TEM samples were prepared by dispersing the purified QDs in hexane and drop casting them on carbon-coated copper grids.

### **2.3 Results and discussion**

#### **2.3.1 ZnTe QDs**

There are few studies on the synthesis of ZnTe QDs that have been reported in the literature [16, 44], but none has reported the emission spectra of bare ZnTe QDs. The low PL intensity of ZnTe QDs could be due to oxidation of the ZnTe QDs. In this study, the PL emission spectra of ZnTe QDs were recorded and the PL emission intensity was found to be much lower than that of ZnSe QDs. ZnTe QDs were stored under an inert atmosphere to avoid oxidation. For the two-pot method of synthesizing ZnTe/ZnSe core/shell QDs, in addition to processing ZnTe QDs under inert conditions, it was found that

the introduction of TOP during the redispersion of ZnTe QDs in coordinating solvent to prevent the oxidation, since TOP is a reducing agent.

### 2.3.2 ZnSe/ZnTe and ZnTe/ZnSe core/shell QDs

According to the band gap alignment of ZnSe and ZnTe, ZnSe/ZnTe and ZnTe/ZnSe core/shell QDs are type II structures (Figure 2.1). A core/shell QD can undergo alloying due to diffusion of elements across the core-shell interface. On the other hand, a ternary QD can exhibit surface segregation leading to uneven composition, as shown schematically in Figure 2.1. The actual band gap of core and shell combined would be smaller than that of a bare core consisting of either material. As a result, the emission peak of the core/shell QDs is expected to shift towards longer wavelengths, compared to the emission peaks of cores made of either material, as the thickness of the shell in the core/shell structure is increased. As shown in Figure 2.2, the emission peak of ZnSe QDs and ZnTe QDs are 425 nm and 450 nm, respectively, both in the blue region of the electromagnetic spectrum. When cores of these materials are encapsulated by a shell consisting of the other material, the observed emission peaks are expected to shift towards the green part of the spectrum as the shell grows thicker. This is the behavior observed in the PL emission spectra of ZnTe/ZnSe and ZnSe/ZnTe core/shell QDs. The red tail in the PL spectra of ZnTe QDs is caused by deep surface traps and it disappears after the surface is passivated by a ZnSe shell.

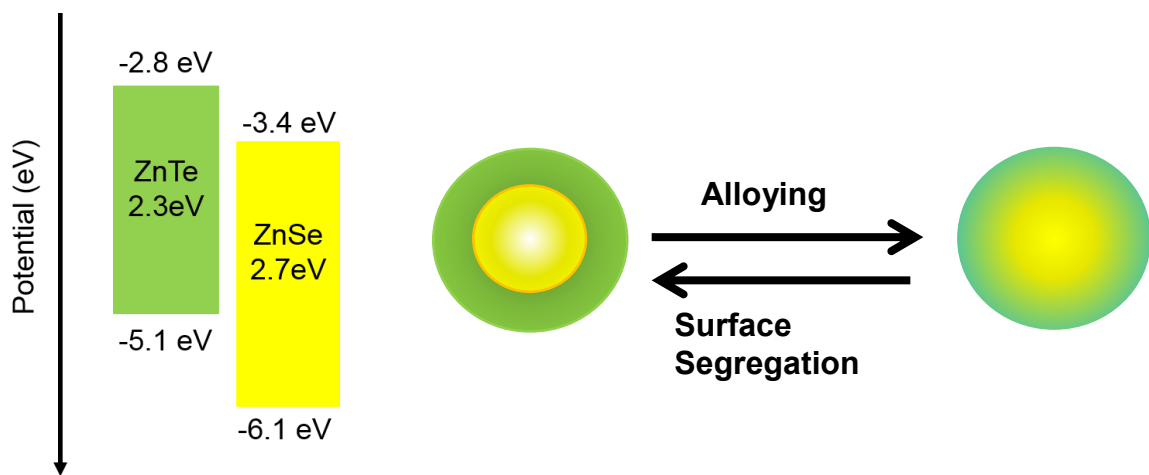


**Figure 2.1** Band gap alignment of bulk ZnTe and ZnSe (left). Schematic representation of alloying and surface segregation in core/shell and ternary QDs (right).

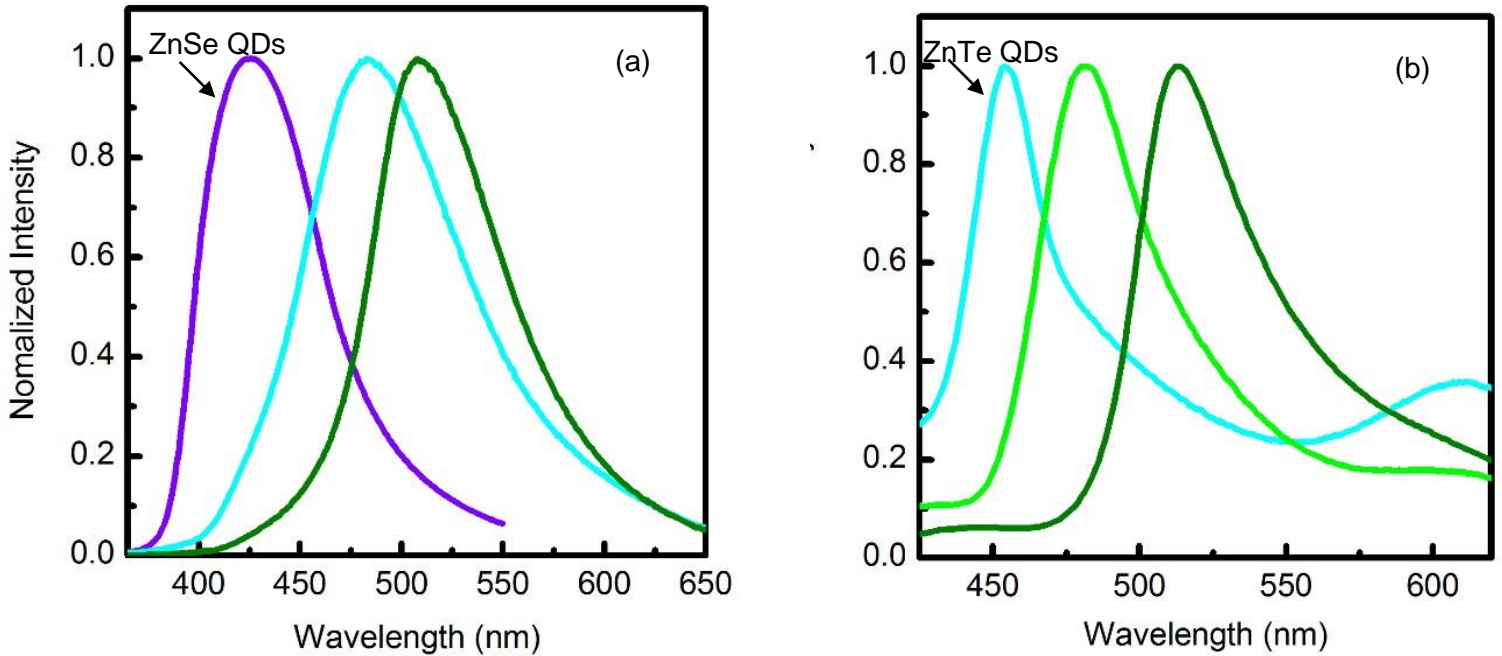


**Figure 2.2. Normalized PL emission spectra of (a) ZnSe QDs and ZnSe/ZnTe core/shell QDs, and (b) ZnTe QDs and ZnTe/ZnSe core/shell QDs. The red shift in the core/shell samples increases with increasing shell thickness.**

### 2.3.3 ZnTe<sub>x</sub>Se<sub>1-x</sub> (0 < x < 1) ternary alloy QDs

Brasil et al.[45] studied the optoelectronic properties of ZnTe<sub>x</sub>Se<sub>1-x</sub> alloys grown by Molecular Beam Epitaxy. The band gap energy of the ternary alloy is a nonlinear function of the Te content and passes through a minimum when  $x=0.65$  (Figure 2.3). This phenomenon is called the bandgap bowing effect. In our study, the ZnTe<sub>x</sub>Se<sub>1-x</sub> alloy QDs were synthesized by injecting Se and Te precursors simultaneously with the Zn precursor. QDs were grown under the same experimental conditions using different ratios of Te to Zn in the precursor mixture. The growth of QDs was monitored by collecting and analyzing samples from the reacting mixture at specific times, until there was no obvious change in the peak PL wavelength. The latter state was typically reached after about 30 minutes of growth time. When

the relative amount of Te is increased with respect to Zn in the precursor mixture, the Te content ( $x$ ) of the alloy QDs is also expected to increase resulting in a reduction of the band gap energy of the alloy QD. As shown in Figure 2.4, the band gap of the  $\text{ZnTe}_x\text{Se}_{1-x}$  QDs decreases as the molar ratio of Te/Zn in the precursor mixture increases. The lack of a minimum in the observed band gap energy of  $\text{ZnTe}_x\text{Se}_{1-x}$  QDs over the range of Te/Zn molar ratios in the precursor solution that were used in our study, indicates that the incorporation efficiency of Se into the alloy QDs is higher than that of Te and, as a result, the Te/Zn ratio in the ternary QD that corresponds to minimum band gap energy was not reached.

The lack of a minimum in the observed band gap energy of the precursor solution over the range of Te/Zn molar ratios in the precursor solution used in our study, indicates that the incorporation efficiency of Zn into the alloy QDs is higher than that of Te.

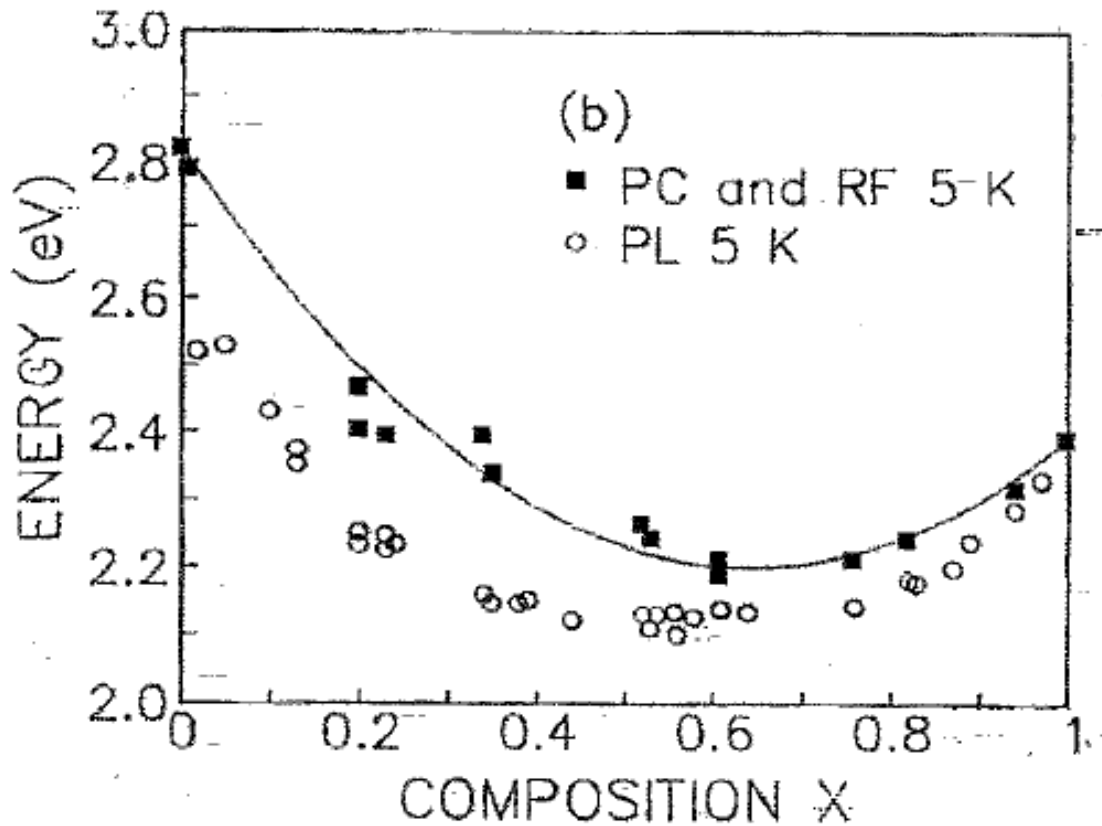
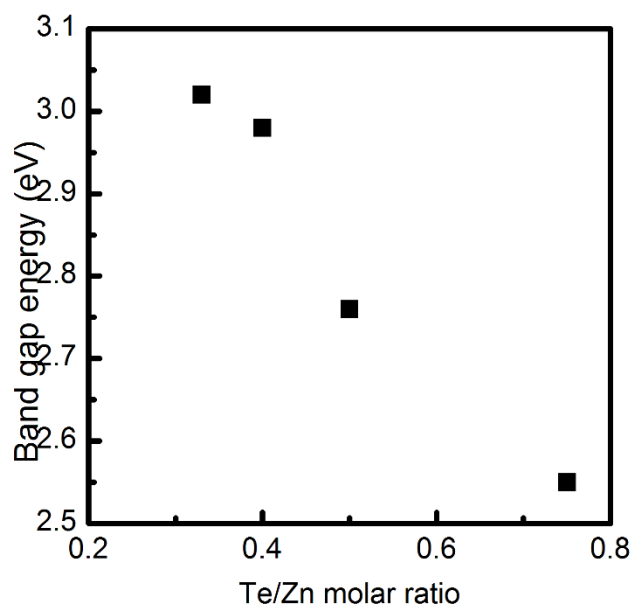


Figure 2.3: Band gap energy as a function of Te composition for bulk  $\text{ZnTe}_x\text{Se}_{1-x}$ [46].



**Figure 2.4: Band gap energy as a function of Te/Zn molar ratio in precursor solution for  $\text{ZnTe}_x\text{Se}_{1-x}$  alloy QDs.**

### 2.3.4 Thermodynamic stability of ZnSe/ZnTe core/shell QDs and ZnTe/ZnSe core/shell QDs

#### 2.3.4.1 Morphology of the ZnSe/ZnTe core/shell and ZnTe/ZnSe core/shell QDs

To study the thermodynamic stability of ZnTe/ZnSe and ZnSe/ZnTe core/shell structures, cores were initially grown under identical condition in a coordinating solvent solution consisting of HDA and TOP. Then, shells were grown under the same experimental conditions, including core size, amount of shell precursors, growth temperature, and coordinating solvent concentration. Shell deposition was performed at 235°C, which is the lowest temperature at which both ZnSe and ZnTe shells can be grown. Figure 2.5 shows TEM images of bare core and core/shell QDs for a shell growth time of 25 minutes. The average size of QDs was obtained using the ImageJ<sup>TM</sup> software, and the average diameter of (a) ZnTe and (b) ZnSe QDs were determined to be 2.3nm. For both types of core /shell QDs, ZnTe/ZnSe (c) and ZnSe/ZnTe (d), the average diameter was estimated to be 2.5nm. The identical size of the core and shell thickness in these QDs enables direct the comparison of XPS data.

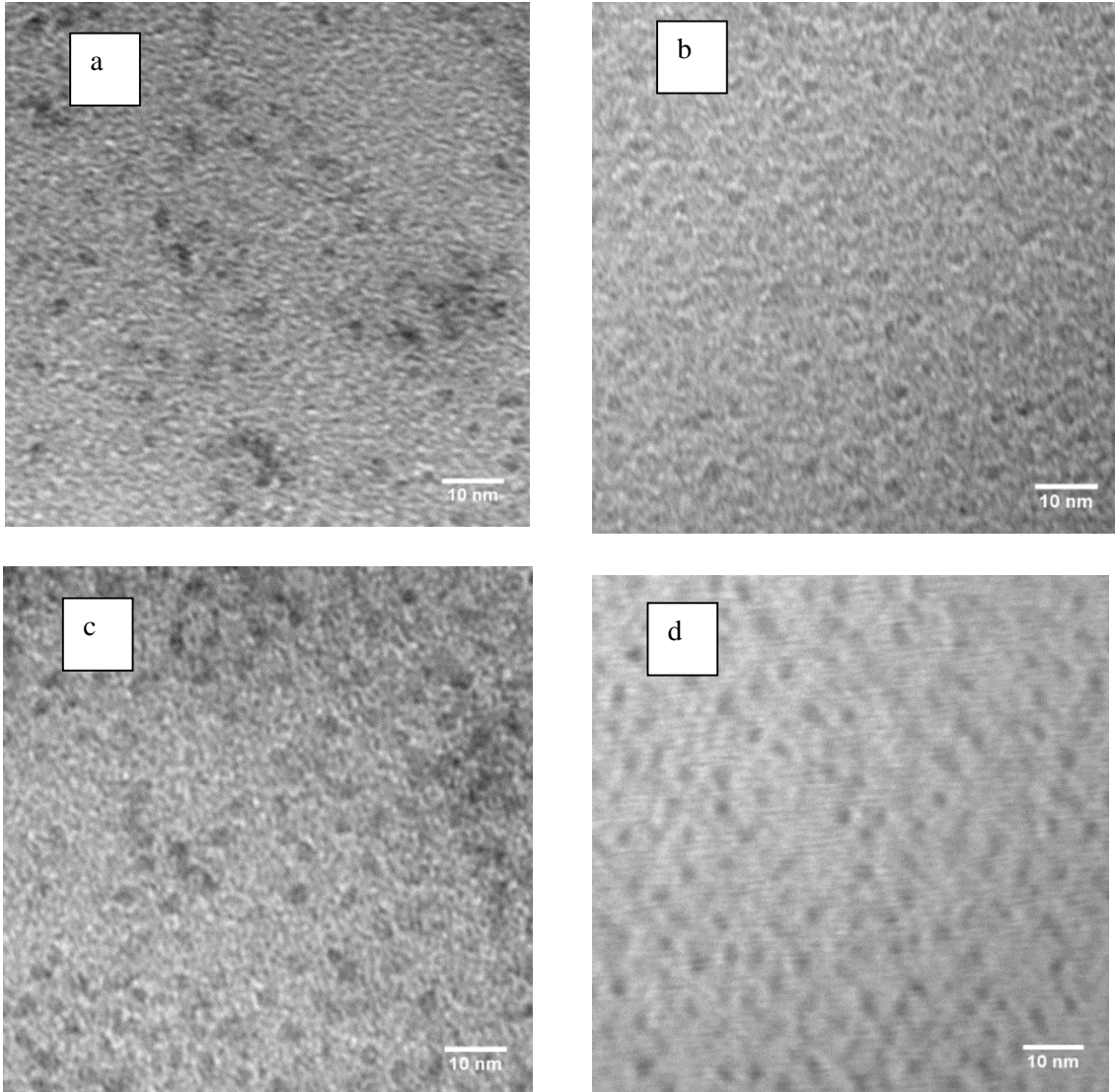


**Figure 2.5: TEM image of (a) ZnTe QDs, (b) ZnSe QDs, (c) ZnTe/ZnSe core/shell QDs and (d) ZnSe/ZnTe core/shell QDs.**

#### **2.3.4.2 Comparison of the peak PL wavelength shift for ZnTe/ZnSe and ZnSe/ZnTe core/shell QDs**

During shell growth performed at 235°C, samples were collected from the growth mixture immediately after the injection of the shell precursors and at short time intervals, typically 5-10 minutes, thereafter. Figure 2.6 illustrates the evolution of the PL emission peak as function of the shell growth

time. The data was obtained by averaging the emission peaks of samples from two batches synthesized under the same experimental condition. For both types of core/shell QDs, the PL peaks shift to larger wavelength as the shell growth time increase, as expected for a type II core/shell structure. The PL peak emission of ZnSe/ZnTe core/shell QDs exhibited a redshift of 48 nm after 5 minutes of shell growth. In comparison, the ZnTe/ZnSe core/shell QDs exhibited 20 nm redshift after 5 minutes of shell growth. For a shell growth time of 25 min and for the same average diameter and shell thickness, the PL peak emission wavelength shift exhibited by the ZnSe/ZnTe core/shell QDs is larger than that of ZnTe/ZnSe core/shell QDs.

There are two possible reasons for the difference in the peak emission wavelength shift between ZnSe/ZnTe and ZnTe/ZnSe core/shell QDs. The shift results from the separation of electrons and holes in the core/shell material. For ZnTe/ZnSe core/shell QDs the electrons are trapped in the shell while for ZnSe/ZnTe core/shell QDs, it is the holes that are trapped in the shell. Since an electron is lighter than a hole, it requires a deeper potential well (greater shell thickness) to achieve the same level of separation between an electron and a hole [47]. The change of the structure during shell growth might also contribute to the change in the spectra. The sharp core/shell interface would disappear if alloying took place, which might lead to a blue shift of the peak PL emission wavelength, in comparison to that of the core/shell structure[48]. If the shell growth does not lead to significant diffusion of Zn and Te across the core-shell interface, a large red shift would be observed.

For ZnTe/ZnSe core/shell QDs, the rate of diffusion of Zn and Te across the core-shell interface can be comparable to the rate of shell growth, thus reducing the expected red shift in the peak PL wavelength and even leading to a blue shift in some cases. This effect is observed after 15 min of shell growth for ZnTe/ZnSe core/shell QDs. Photo-oxidation can be excluded as the reason for the blue shift, since the QDs were synthesized and stored under a nitrogen atmosphere. This discontinuity in the red shift has been observed in several batches of ZnTe/ZnSe core/shell QDs, grown using different amount of shell precursors, as illustrated in Figure 2.7.

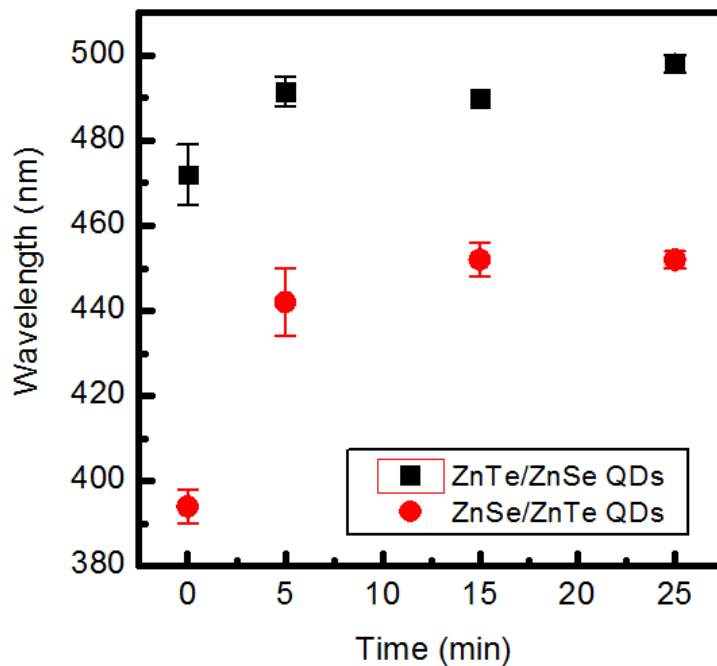


Figure 2.6: Peak PL emission wavelength of ZnTe/ZnSe core/shell QDs (squares) and ZnSe/ZnTe core/shell QDs (circles) at different shell growth times.

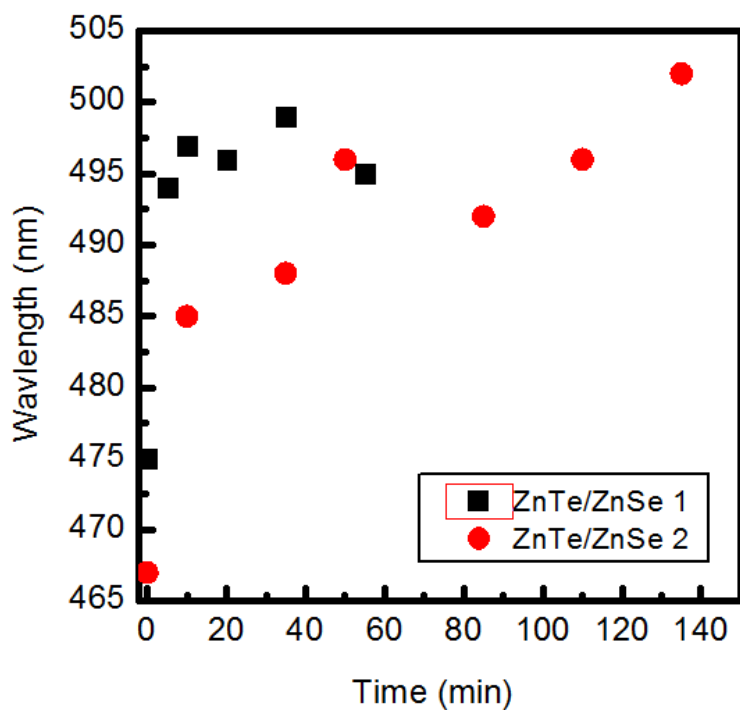


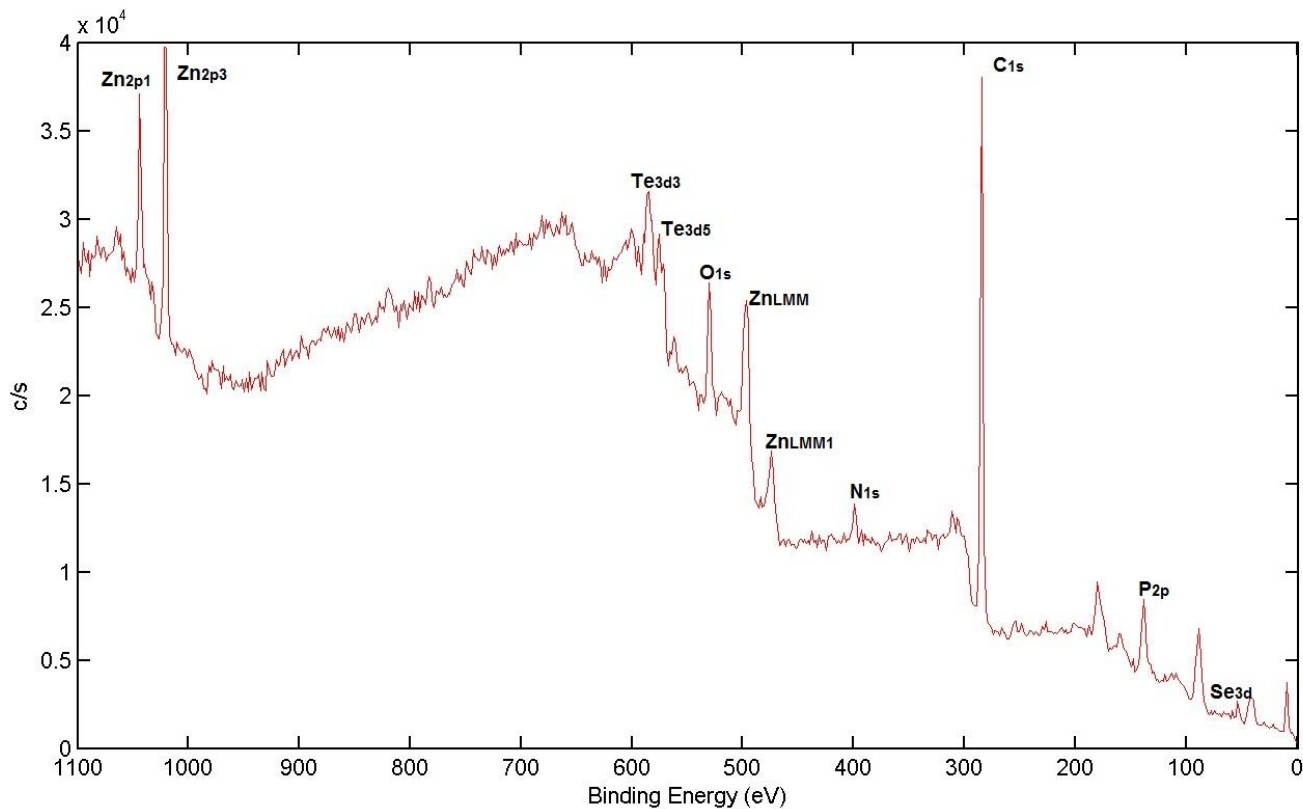
Figure 2.7: Peak PL emission wavelength of ZnTe/ZnSe core/shell QDs corresponding to different batches. The amount of Se precursor added is 0.9 mmol for batch 1 and 1.35 mmol for batch 2.

### 2.3.4.3 XPS characterization of ZnTe/ZnSe and ZnSe/ZnTe core/shell QDs

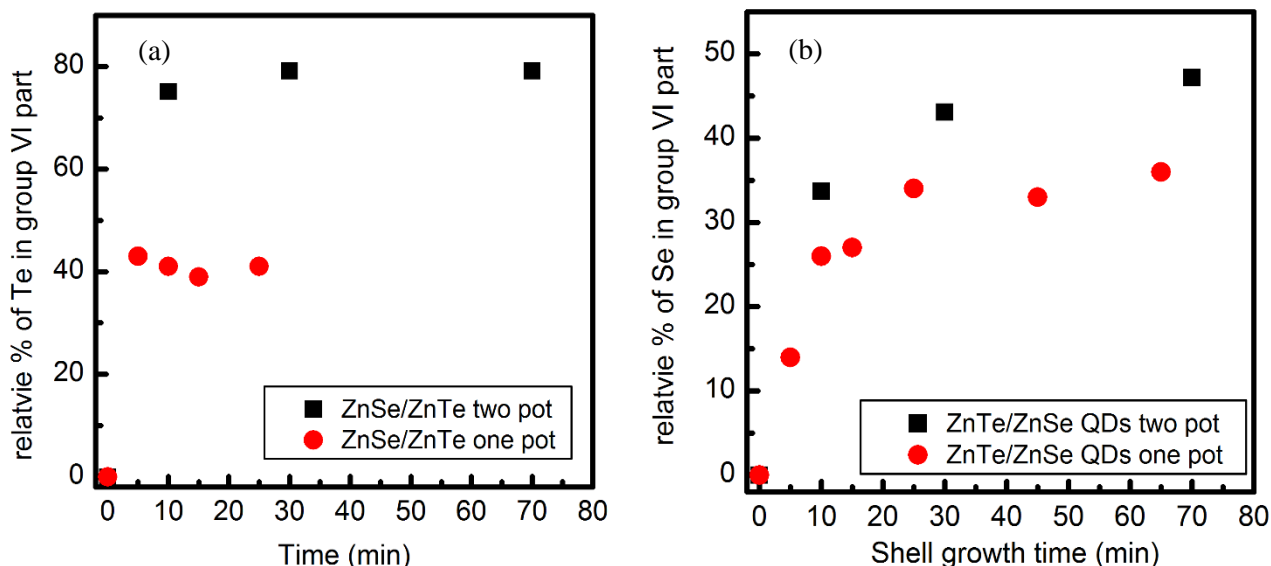
The core/shell QDs were characterized using XPS. Figure 2.8 shows a wide-scan XPS spectrum of ZnTe/ZnSe core/shell QDs. The elements detected in the sample are Zn, Te, Se, N, P, C, and O. Oxygen most likely came from the environment, while C, N, and P from the surfactants, HDA and TOP. The relative atomic concentration of Te and Se was compared by integrating the high resolution spectra of  $\text{Te}_{3d5}$  and  $\text{Se}_{3d3}$  peaks using the MultiPak™ software. XPS is a surface sensitive technique and the intensity of the XPS signal decays exponentially with the distance from the surface of the material. According to the TPP-2M formula[49], the inelastic mean free path (IMFP) of ZnTe and ZnSe are 2.0 and 2.5nm, respectively. Since the IMFP is of the same order as the QDs size, the XPS measurements contain contributions from the core as well. Thus, for thin shell thickness (0.2nm), it is reasonable to expect that the XPS spectrum will show a concentration of the core group VI element that is larger than that of the group VI element in the shell. The XPS-derived atomic concentration ratio of (N+P) to Zn was in the range of 3.5-4.5 for all samples, supporting the assumption that both N and P are on the surface and contained in the HDA and TOP surface capping molecules, respectively.

Figure 2.9 shows the XPS-derived relative % atomic concentration of Te and Se for the ZnSe/ZnTe QDs and ZnTe/ZnSe core/shell QDs at different shell growth times. The relative % atomic concentration of the Te atoms in group VI part of ZnSe/ZnTe core/shell QDs and Se atoms in group VI part of ZnTe/ZnSe core/shell QDs is estimated to be 13.5%, which is calculated using the core size and shell thickness obtained from TEM image. As XPS is a surface sensitive technique, at the end of the shell growth the XPS-derived relative % atomic concentration of the Se in ZnTe/ZnSe QDs is 41% and the XPS-derived relative % atomic concentration of Te in ZnSe/ZnTe QDs is 35%. As expected, the composition of elements in the shell increases with shell growth time, and appears to reach a plateau. In the case of ZnSe/ZnTe QDs, the plateau is reached more rapidly. These trends were retained in the core/shell QDs grown by two-pot synthesis with purification of the cores before shell growth. The

increase in the concentration of the shell elements in the two-pot samples is most likely due to the larger amount of shell precursor used.



**Figure 2.8: XPS wide-scan spectra of ZnTe/ZnSe core/shell QDs.**



**Figure 2.9: (a) XPS-derived relative % of Te atoms in group VI part of the ZnSe/ZnTe core/shell QDs at different growth times. (b) XPS-derived relative % of Se atoms in group VI part of the ZnTe/ZnSe core/shell QDs at different growth times. The squares correspond to two-pot synthesis with intermediate purification of the cores and the circles to one-pot synthesis.**

The differences between ZnTe/ZnSe and ZnSe/ZnTe QDs in the XPS atomic concentration evolution can be attributed to differences in the shell growth kinetics and thermodynamic stability of the structures. The rate of shell growth was manipulated by the binding of ligands to the surface of the core and the precursors [20]. The weaker binding of TOP to the Se precursor, or lower surface coverage of HDA and TOP to the surface of the ZnSe core will lead to higher growth rate for the ZnTe shell. To maximize stability, the materials will attempt to form a structure that corresponds to the lowest possible free energy. The observed evolution of the atomic concentration of Se and Te suggests that the ZnSe/ZnTe core/shell structure is more stable than its inverse structure. Both the surface energy and lattice strain would affect the distribution of the atoms. If the surface energy of ZnSe is higher than that of ZnTe QDs, the growth of a ZnTe shell on a ZnSe core would increase stability. Due to differences in the lattice constant of ZnSe and ZnTe and in the size of Te and Se atoms, defects that facilitate diffusion form at the core-shell interface. It is possible that slower shell growth and increased interdiffusion of Se and Te

lead to the slower increase in the XPS-derived concentration of the shell element, Se, in ZnTe/ZnSe core/shell QDs. This hypothesis is also supported by the PL data.

To isolate the thermodynamic effects from the kinetics of shell growth, ZnSe/ZnTe and ZnTe/ZnSe QDs were extracted from the growth solution at a growth time of 15 minutes and purified by washing with hexane and methanol. The 15 minute shell growth time is essential to reduce the possibility of incomplete shell growth. The QDs were subsequently dispersed in HDA and TOP and heated to 235°C with the mixture reaching that temperature in about 10 minutes. The variations in the XPS-derived concentrations during the 10-minute ramping of the temperature from ambient to 235°C were less than 1%. The effects of annealing at 235°C on the XPS-derived concentrations of Se and Te were subsequently studied as function of annealing time at 235°C. Samples were collected from the mixture after 20 minutes and 50 minutes of annealing time at 235°C. Figure 2.9 shows the XPS-derived atomic concentrations of Te and Se in the core/shell QDs as functions of annealing time. For the ZnTe/ZnSe QDs, the Te concentration increased by 4.7% after 20 minutes. The increase in the Te concentration implies that diffusion of Se and Te across the core-shell interface occurred and, as a result, there are more Te atoms distributed near the surface of QDs. Partial dissolution of the ZnSe shell during annealing could also cause the observed increase in Te concentration, but in such a case the XPS-derived Te concentration would further increase after annealing for a longer time. This is not supported by the XPS data, because the Te concentration only slightly changed with annealing time. For ZnSe/ZnTe QDs, the 3% decrease of the Te concentration might arise from diffusion of Se and Te across the core-shell interface, the Te concentration raised back at longer annealing time indicates the Te rich structure is the most stable configuration.

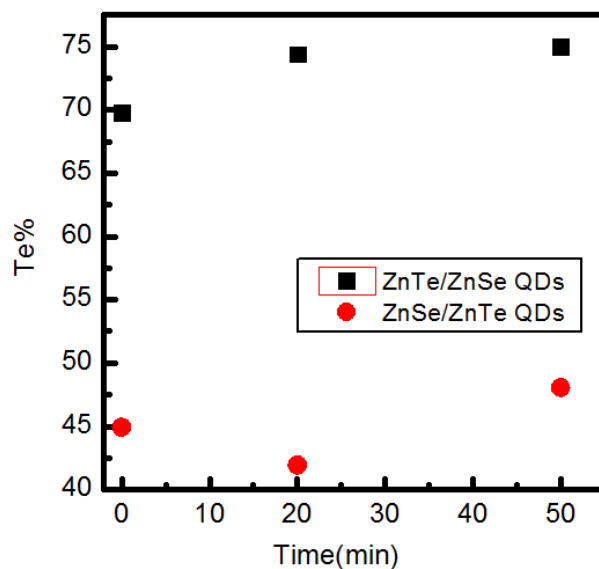


**Figure 2.10: XPS-derived relative % of Te atoms in group VI part of the ZnSe/ZnTe core/shell QDs at different annealing times (circles) and XPS-derived relative % of Se atoms in group VI part of the ZnTe/ZnSe core/shell QDs at different annealing times (square).**

## 2.4 Conclusions

In conclusion, colloidal ZnSe/ZnTe and ZnTe/ZnSe core/shell QDs having the same average core size and shell thickness were synthesized. The evolution of the PL peak emission wavelength as function of the shell growth time indicates that both structures correspond to are type II QDs. It was found that the emission peak of ZnSe/ZnTe QDs exhibits a larger red shift than the one corresponding to ZnTe/ZnSe QDs. The relatively slower and discontinuous red shift in the PL spectra of ZnTe/ZnSe QDs could be caused by diffusion of Se and Te atoms across the core-shell interface. This hypothesis is supported by observations of XPS-derived concentrations of shell elements in the ZnSe/ZnTe QDs. The XPS-data reach a plateau with respect to processing time faster for ZnSe/ZnTe QDs than for ZnTe/ZnSe QDs. The atomic concentration of Te obtained by XPS during post-growth annealing was found to increase with annealing time, indicating that structures with Te rich surfaces are thermodynamically more stable.

## CHAPTER 3

### SYNTHESIS OF NEAR-INFRARED (NIR) ABSORBING SnSe QUANTUM DOTS USING AIR-STABLE PRECURSORS

#### 3.1 Introduction

Colloidal quantum dots (QDs) that are optically active in the near infrared region have shown great potential for applications in photovoltaics[50-52] , near infrared (NIR) photodetectors [53], and photothermal therapy [54]. SnSe has emerged as a promising and environmentally friendly NIR material because it does not contain toxic heavy metals, such as Pb, Cd, or Hg. In addition, it consists of earth-abundant elements that can lower the cost of QD production as well as ensure the long-term availability of the materials.

Franzman et al.[55] reported the synthesis of elongated anisotropic SnSe nanocrystals (19.5 nm wide and polydisperse in length) by injecting di-tert-butyl diselenide into a solution containing anhydrous tin(II) chloride, dodecylamine and dodecanethiol. Baumgardner et al.[56]synthesized SnSe QDs with an average diameter of 4-10 nm by injecting bis[bis(trimethylsilyl)amino]tin(II) into a mixture of hot trioctylphosphine selenide ( TOPSe) and oleylamine (OLA). In both cases, toxic and pyrophoric organometallic precursors were used. As “green chemistry” has become one of the major objectives of the nanotechnology process development efforts, several research groups started looking into the synthesis of SnSe nanostructures using safer starting materials. SnSe nanosheets were synthesized [57]by slowly heating a reaction mixture of SnCl<sub>2</sub>, oleylamine, trioctylphosphine selenide (TOPSe), and hexamethyldisilazane (HMDS) to 240 °C. Another study focused on SnSe nanosheet synthesis from mixtures of SnCl<sub>4</sub> · 5H<sub>2</sub>O, SeO, oleylamine and 1,10-phenanthroline at 260 °C [58]. Ma et al. obtained SnSe nanoparticles with an average size of 30 nm by pulsed electrochemical deposition, using an electrolyte containing Na<sub>2</sub>SeO<sub>3</sub>, SnCl<sub>2</sub> · 2H<sub>2</sub>O, C<sub>6</sub>H<sub>5</sub>Na<sub>3</sub>O<sub>7</sub> · 2H<sub>2</sub>O, DI water and glycerol [59]. SnSe QDs with a diameter of 4nm and a band gap of 3.89 eV were synthesized from SnCl<sub>2</sub> · 2H<sub>2</sub>O and sodium

selenite precursors [60]. Ning et al. synthesized SnSe nanocrystals with diameters of 7.2, 19.5 and 24 nm using  $\text{Sn}_6\text{O}_4(\text{OH})_4$  and selenourea as precursors[61]. The reported work is summarized in Table 3.1

Author	Precursors	Growth media	Structure and size
Franzman, M.A., et al., 2010	anhydrous tin(II) chloride, di-tert-butyl diselenide	dodecylamine, dodecanethiol	nanoparticle 4-10 nm
Baumgardner, W.J., et al., 2010	bis[bis(trimethylsilyl)amino] tin(II), trioctylphosphine selenide	oleylamine	elongated, anisotropic nanocrystals 19.0 ± 5.1 nm wide
Vaughn, D.D., et al., 2010	tin(II) chloride, trioctylphosphine selenide	hexamethyldisilazane , oleylamine	nanosheet 500 nm by 500 nm, thickness 10-40 nm
Li, Z., et al., 2011	tin (II) chloride dihydrate, sodium selenite	hexadecyl trimethyl ammonium bromide, isopropanol	nanoparticle 4 nm
Ning, J., et al., 2011	tin oxide hydroxide, selenourea	oleylamine	nanoparticle 7-24 nm
Li, L., et al., 2013	selenium dioxide, tin(IV) chloride pentahydrate	oleylamine, 1,10-phenanthroline	nanosheet 300 nm by 300 nm, thickness 1 nm
Ma, L.L., et al., 2013	sodium selenite pentahydrate, tin (II) chloride dihydrate	sodium citrate dihydrate, DI water and glycerol	nanoparticle 30 nm

**Table 3.1 Summary of reported work on the synthesis of SnSe nanostructures**

There is no reported study on the synthesis of small-size (< 4nm) NIR-absorbing SnSe QDs using air-stable precursor. The small particle sizes are necessary for applications using Förster resonance energy transfer (FRET). Furthermore, for in-vivo applications the complete renal clearance of QDs requires that the hydrodynamic size, including all capping layers, is less than 5.5 nm[30]. Our study was focused on the development of a method for growing small-size NIR-absorbing SnSe QDs using  $\text{SnCl}_2$ -oleylamine and trioctylphosphine-Se complexes as precursors. The effects of the oleylamine (OLA) to trioctylphosphine (TOP) ratio on the growth kinetics of the SnSe QDs were investigated.

## 3.2 Experimental section

### 3.2.1 Synthesis of SnSe QDs

The synthesis of SnSe QDs was performed under N<sub>2</sub> environment. For a typical synthesis, 0.4 mL OLA (1.2 mmol) and 0.8 mL octadecene (ODE) (2.4 mmol) were added to 1.2 mmol of SnCl<sub>2</sub> in a small vial to form the stock solution of the Sn precursor. ODE was used to reduce the viscosity of the precursor solution. Sonication was applied to the mixture until most of the larger SnCl<sub>2</sub> crystals were broken into smaller pieces and the mixture became a gel-like liquid. Then, the vial was heated to 70 °C and kept at a temperature of 70-100 °C for 1 h. The resulting SnCl<sub>2</sub>-OLA complex was a highly viscous light-yellow solution. TOPSe was prepared by dissolving 0.36 mmol of Se powder in 0.45 mL of TOP. The as-prepared TOPSe was premixed with 0.3 mL of the Sn precursor solution at room temperature, while a reaction medium containing 3.2 mL of pure OLA or a mixture of OLA and TOP with a total volume of 3.2 mL was heated to 135 °C. After injection of the precursor solution into the reaction medium, the temperature of the mixture was kept at 90-100 °C for 20 minutes to 1 hour to enable growth of SnSe QDs.

### 3.2.2 Capping of SnSe QDs with a ZnSe shell

A Zn precursor solution was prepared by adding 2.4 mL Et<sub>2</sub>Zn to 2 mL of TOP at room temperature. A 15 mL solution of as-prepared SnSe QDs, synthesized from 1.2 mmol of SnCl<sub>2</sub>-OLA complex and 1.44 mmol of TOPSe, was heated to 80 °C. The Zn precursor solution was injected into the reaction flask in doses of 0.2 mL over a period of 20 min. The temperature of the reacting mixture was increased from 80 °C to 150 °C during that period. After the last injection, the reaction mixture was kept at 150 °C for 10 min, then cooled to 100 °C and kept at this temperature for 4 hours under continuous stirring. Samples were collected and stored in a dark environment.

### **3.2.3 Surface modification of SnSe/ZnSe core/shell QDs with MUA**

A chloroform/acetone mixture was added to the as-prepared SnSe/ZnSe QDs, and the QDs were collected as a precipitant after centrifuging the mixture at 4500 rpm for 20 min. The QDs were subsequently modified with mercapto-undecanoic acid (MUA) and dispersed in DI water using the protocol reported by Wang [62, 63].

### **3.2.4 Characterization**

The absorption spectra of the QDs were collected with a UV-VIS-NIR spectrophotometer (Shimadzu, UV-3600) from samples prepared by dispersing as-grown QDs in chloroform. Transmission electron microscopy (TEM) was performed on a JEOL 2000 FX electron microscope operating at 200KV. The TEM samples were prepared by drop casting dispersions of as-grown or purified QDs in chloroform. To remove the excess amount of precursors, OLA and TOP, a chloroform/methanol or chloroform/acetone mixture was added to the QD solution and the mixture was centrifuged at 4200 rpm/min for 10 min. The precipitate containing the QDs was redispersed in chloroform. The crystalline structure of the SnSe QDs was characterized by X-ray diffraction using a PANalytical X'Pert Diffractometer.

## **3.3 Results and discussion**

### **3.3.1 Choice of precursors**

The commercially available tin precursors such as tin acetates, tin oxide and tin chloride were tested. Those precursors were dispersed in different coordinating solvents, such as fatty acids and alkylamines. It was found that tin acetate forms a clear complex with the coordinating solvent while tin oxide is only partially dispersed.

The reactivity of tin acetate – stearic acid/ lauric acid/ OLA complex was studied first. The reaction solvent would turn from yellow to black after heating the reaction mixture for 4-20 minute at

temperatures ranging from 170 -250 °C, indicating that the precursors were reacted. XRD patterns of the sample produced peaks characteristic of orthorhombic SnSe crystal structures (Figure 3.1). The as-prepared samples were dispersed in chloroform for absorption characterization. The black SnSe material would precipitate from the chloroform solution during storage, suggesting that the colloidal dispersion of SnSe crystals in chloroform is not stable. However, the SnSe could be redispersed by sonicating the solution for few minutes. As shown in Figure 3.2, a typical SnSe sample exhibited absorbance from the UV to the NIR region of the spectrum. An absorption shoulder was recorded at 600 nm. Such a feature was not present in the absorption spectra of SnSe QDs reported in [56]. The SnSe nanoparticles were further characterized using TEM. As shown in Figure 3.2, nanoparticle with sizes between 1 and 4 nm aggregate to form a dendritic structure. The absorption shoulder at 600 nm can be attributed to the aggregates. The aggregation could be due to the insufficient passivation of the coordinating solvent.

The use of SnCl<sub>2</sub>-OLA as precursor enables nucleation to take place at temperatures as low as 130 °C immediately after the injection of the precursor. For all subsequent SnSe synthesis, a SnCl<sub>2</sub>-OLA complex and TOPSe were used as precursors for SnSe QDs. The SnCl<sub>2</sub>-OLA complex and the reaction medium containing OLA needed to be prepared separately, because the reaction would not take place at 130 °C if the SnCl<sub>2</sub> was dispersed directly in a reaction medium consisting of OLA. It is possible that an excess amount of OLA hinders the adsorption and subsequent reaction between SnCl<sub>2</sub>-OLA complex and TOPSe.

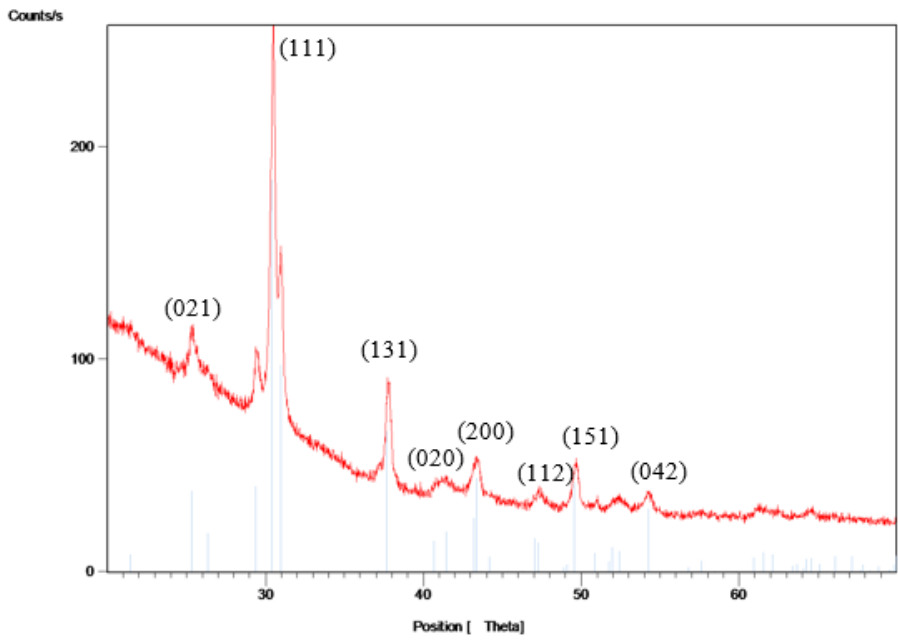


**Figure 3.1: X-ray diffraction pattern of a SnSe nanostructure synthesized from tin acetate- stearic acid and TOPSe.**

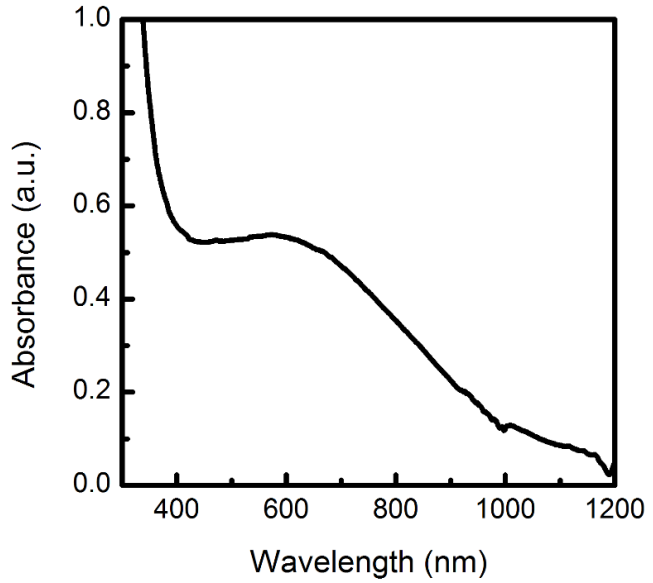


**Figure 3.2: Absorption spectrum of SnSe nanocrystals synthesized from tin acetate-stearic acid and TOPSe.**

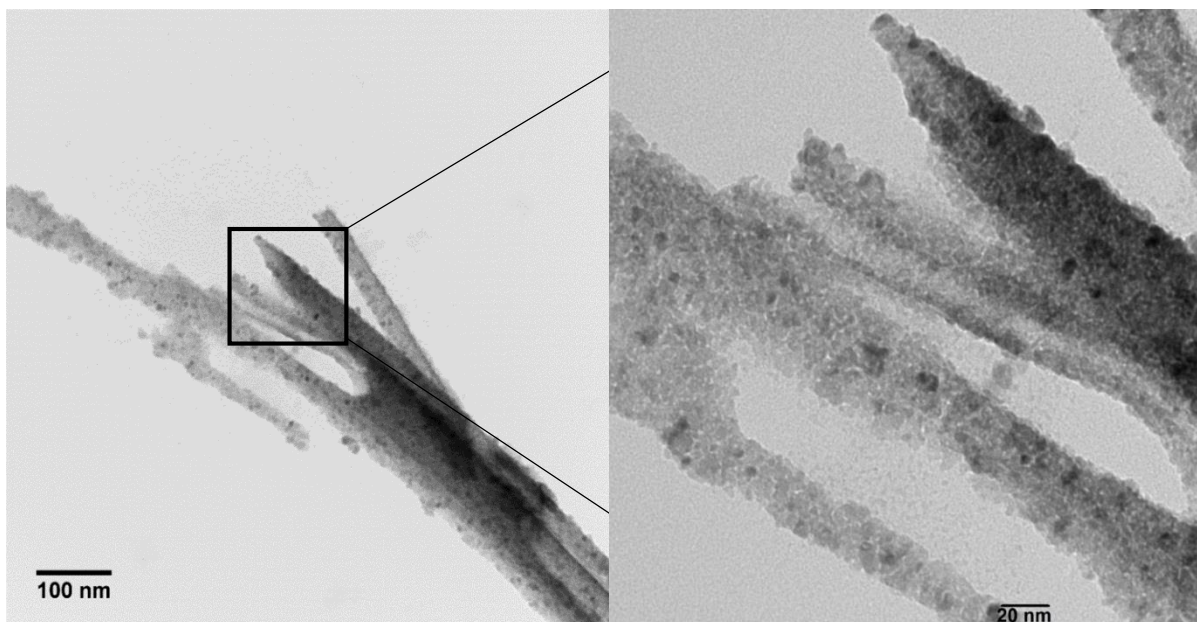


**Figure 3.3: TEM image of SnSe dendritic structure synthesized from tin acetate-stearic acid and TOPSe.**

### 3.3.2 Characterization of SnSe QDs

The six different growth conditions for synthesizing SnSe nanocrystals used in this study are summarized in Table 3.2.

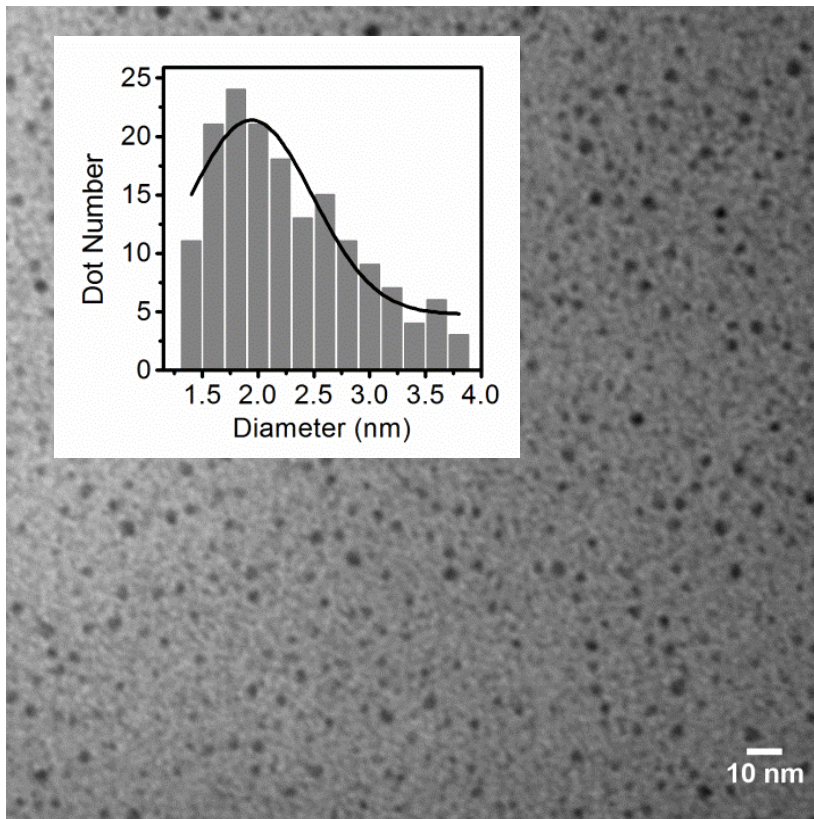
Figure 3.4 shows the TEM image of SnSe QDs grown under the growth conditions corresponding to case 1. The size distribution of the QDs is shown in the inset of Figure 3.4. The QDs size ranges from 1.4 to 3.8 nm with an average size of 2.5 nm. The absorption spectrum of the SnSe QDs corresponding to Figure 3.3 is shown in Figure 3.5. The absorption spectrum obtained from a QD dispersion in chloroform shows that the particles absorb across the UV-VIS-NIR wavelength range. The inset of Figure 3.5 shows the square of the absorption coefficient as function of the photon energy. The direct band gap energy of the QDs was estimated by extrapolating the linear part of this curve to the energy axis and was found to be 1.7 eV. This value is blue shifted when compared to the direct band gap energy of bulk SnSe (1.3 eV) indicating quantum confinement. It should be mentioned that the value of the direct band gap energy estimated by this method depends not only on the average particle size but also on the particle size

distribution and shape. For example, a band gap energy of 1.7 eV was obtained from SnSe QDs with average size of 4.2nm ( $\pm 0.8$  nm) [56] and from elongated SnSe nanocrystals that are  $19 \pm 5$  nm wide and polydisperse in length [55].

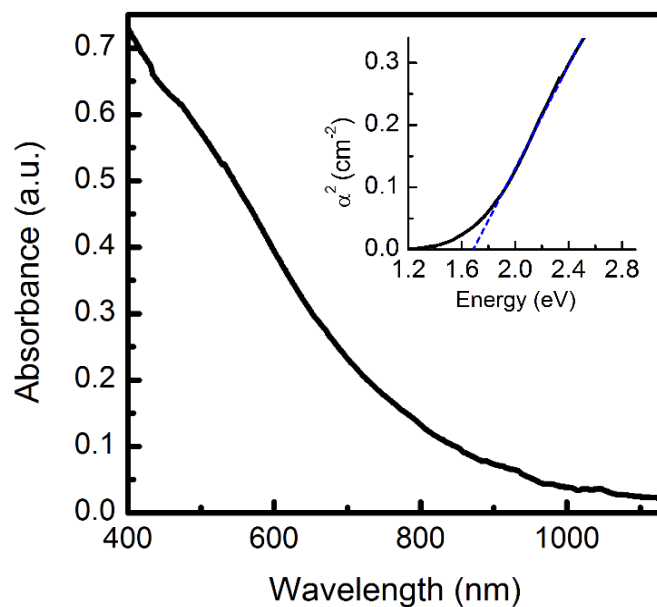
Figure 3.6 shows the X-ray diffraction (XRD) pattern of SnSe QDs grown under conditions corresponding to case 2. The XRD pattern exhibits peaks at  $26.4^\circ$ ,  $29.8^\circ$  and  $52.0^\circ$ , which correspond to the (210), (111) and (402) planes of orthorhombic SnSe, respectively.

**Table 3.2 Summary of SnSe QDs synthesis conditions in different cases.**

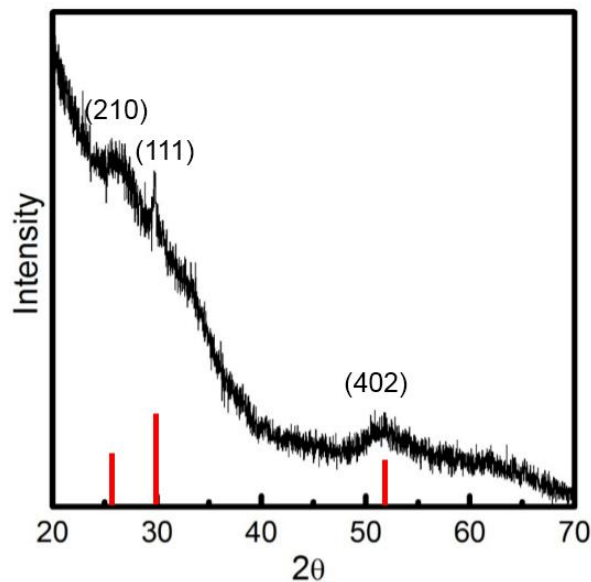
	Sn-OLA (mol/L)	TOPSe (mol/L)	OLA (mol/L)	TOP (mol/L)	OLA/TOP molar ratio	OLA/Sn molar ratio	TOP/Se molar ratio	Injection Temp ( $^\circ\text{C}$ )	Growth Temp ( $^\circ\text{C}$ )
case 1	0.19	0.23	1.33	0.91	1.46	7.00	3.96	135	90-100
case 2	0.19	0.23	1.71	0.63	2.71	9.00	2.74	135	90-100
case 3	0.08	0.09	1.90	0.70	2.71	25.33	7.78	135	90-100
case 4	0.05	0.06	2.48	0.17	14.59	49.60	2.83	135	90-100
case 5	0.19	0.23	1.71	0.63	2.71	9.00	2.74	150	120- 130
case 6	0.08	0.09	1.90	0.70	2.71	25.33	7.78	170	100- 110



**Figure 3.4: TEM image and size distribution (inset) of SnSe QDs grown under conditions corresponding to case 1 (Table 1) for 10 minutes after precursor injection.**



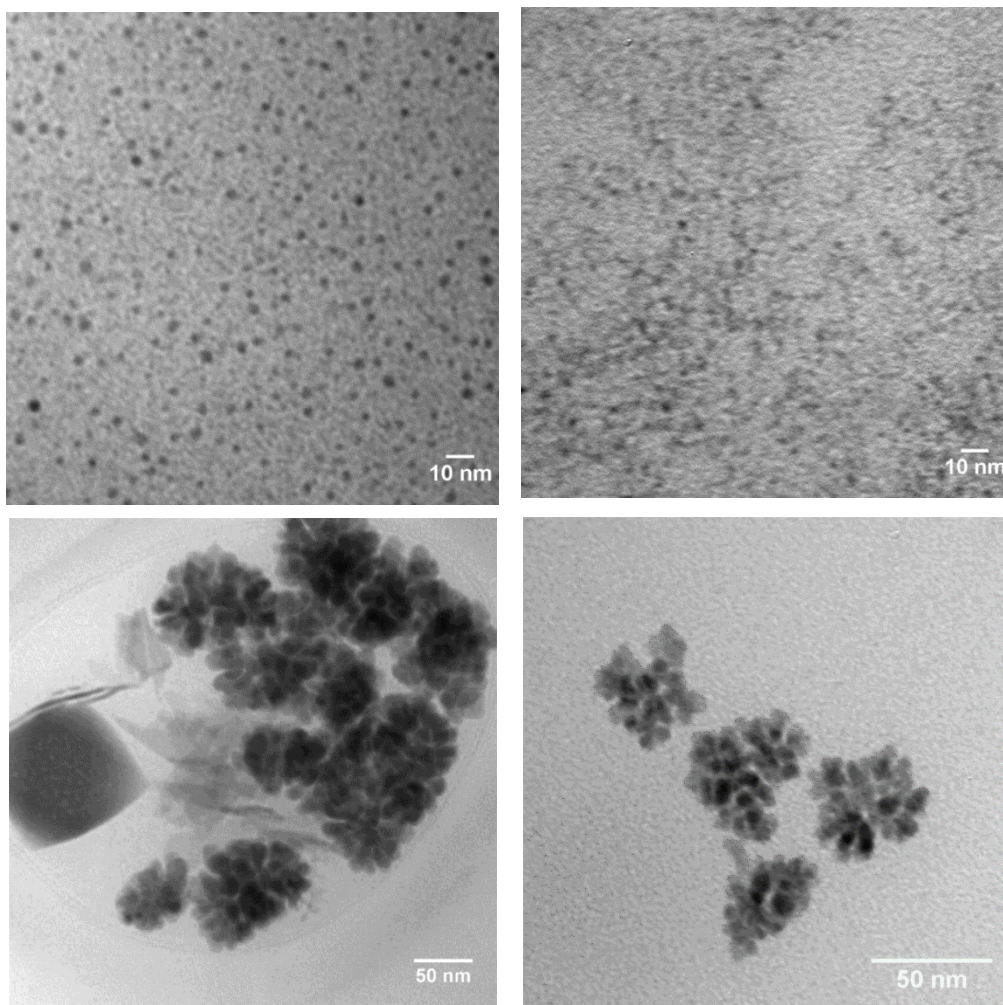
**Figure 3.5: Absorption spectrum of SnSe QDs dispersed in chloroform. The inset shows a plot of the square of the absorption coefficient versus photon energy and has been used to determine the direct band gap of SnSe QDs. The growth conditions are the same as in Figure 3.4.**



**Figure 3.6: X-ray diffraction pattern of SnSe QDs grown under conditions corresponding to case 2 (Table 3.2) and a growth time of 10 min.**

### 3.3.3 The effects of OLA/TOP molar ratio on the morphology of the SnSe QDs

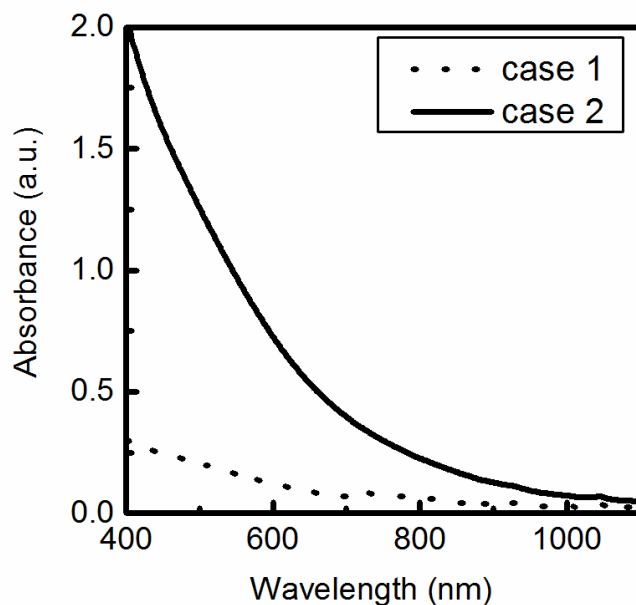
Figure 3.7 shows TEM images of particles grown under conditions corresponding to case 1 and case 2 for 10 and 20 minutes from precursor injection. At 10 minutes, both samples consist of individual particles. In case 1 (Figure 3.7a), the estimated particle size is 2.5 nm. In case 2 (Figure 3.7b), the estimated particle size is 1.7 nm, indicating that changing the OLA to TOP ratio in the growth mixture can be used to control the particle size. At 20 minutes, both samples exhibit aggregation, with case 1 corresponding to larger aggregates and nanosheets (Figure 3.7c) in comparison to case 2 (Figure 3.7d).



**Figure 3.7.** TEM images of SnSe samples obtained under growth conditions corresponding to case 1 and case 2 (Table 3.2) at different times after precursor injection. (a) case 1 at 10 min, (b) case 2 at 10 min, (c) case 1 at 20 min, (d) case 2 at 20 min.

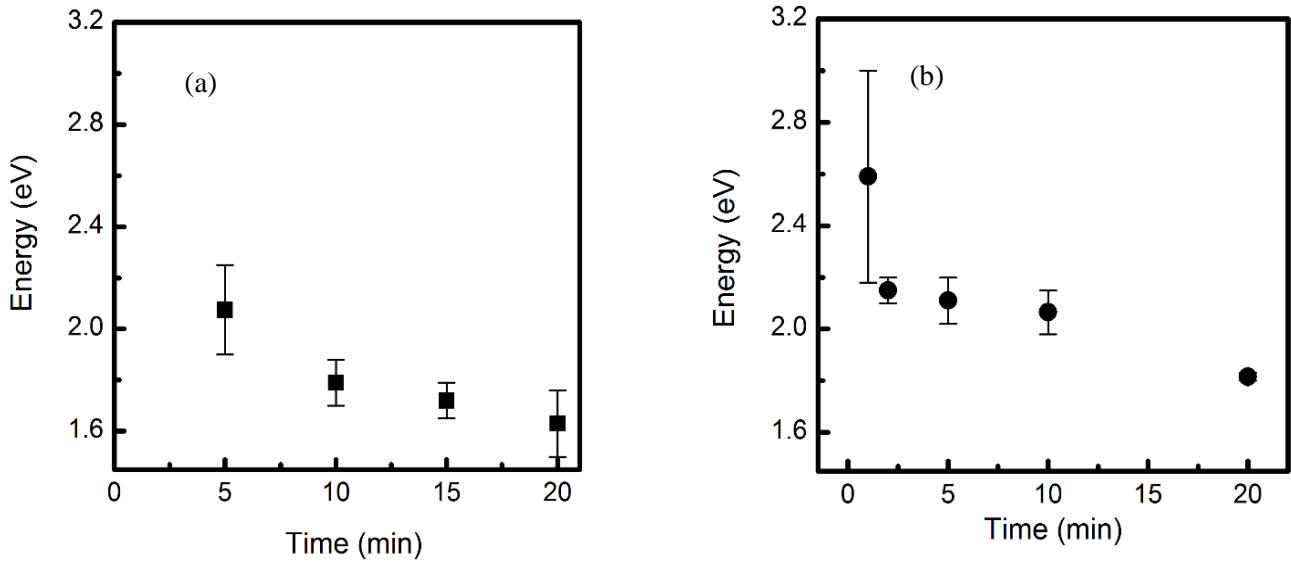
### 3.3.4 The effect of OLA/TOP molar ratio on the nucleation and growth rate of SnSe QDs

Figure 3.8 shows a comparison of the absorption spectra of SnSe QDs grown under conditions corresponding to case 1 and case 2 (Table 3.2), at 10 minutes after the injection of the precursors. In case 1, the ratio of OLA to TOP is smaller in comparison to case 2. The comparison of the absorption spectra shows that the sample corresponding to case 2 exhibits stronger absorbance. Since the sample volume taken from the reaction mixture and dispersed in chloroform is the same in both cases, the stronger absorbance indicates a higher particle number density for the case 2 sample. This could be the result of a higher nucleation rate in case 2, when compared to case 1. This hypothesis is supported by the observation of a color change in the solution corresponding to case 2, one minute after precursor injection. For samples grown under conditions corresponding to case 1, color change was observed after five minutes from precursor injection.



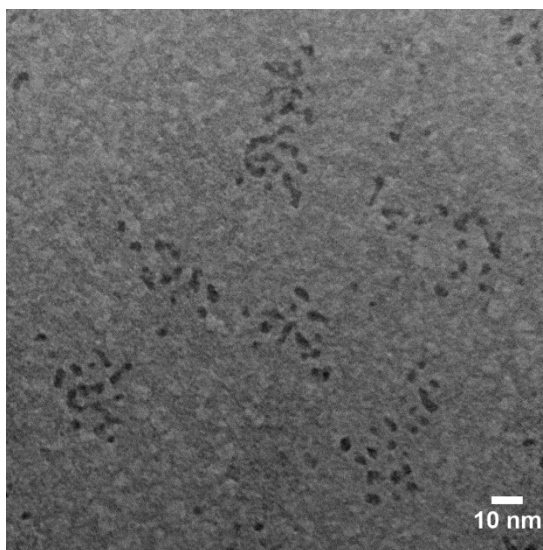
**Figure 3.8:** The effect of the OLA to TOP molar ratio on the absorption spectra of SnSe QDs grown for 10 min under conditions listed in Table 3.2 (case 1 and case 2).

Figure 3.9 shows the temporal evolution of the direct band gap energy of SnSe samples corresponding to case 1 and 2. The large error at 1 min could be due to the change of the temperature right after the precursor injection and the fast nucleation process. The sample corresponding to case 1 exhibits a continuous decrease in the band gap energy during a period of 20 minutes after precursor injection. On the other hand, the sample corresponding to case 2 exhibits a faster rate of change in the direct band gap energy at early growth times reaching a plateau at about 2 minutes from precursor injection. The value of direct band gap energy decreases again at 20 minutes from precursor injection, due to aggregation (Figure 3.7d). Since the difference between the two cases is the OLA to TOP ratio, it can be concluded that a lower OLA to TOP ratio decreases the nucleation rate of SnSe and leads to the formation of larger particles that grow by surface deposition of unreacted precursors. In both case 1 and case 2, particle aggregation was observed at 20 minutes from precursor injection due to insufficient surface protection by OLA and TOP ligands.



**Figure 3.9: Temporal evolution of the direct band gap of SnSe QDs grown under conditions corresponding to (a) case 1 and (b) case 2 (Table 3.2). For growth times up to 10 min, both samples consist of individual particles. At 20 min, particles in both cases have aggregated, as shown in Fig. 3.7.**

In case 3, the amounts of OLA and TOP in the mixture were increased and the amount of Sn and Se precursors was decreased. As expected, particle growth rate decreased and the onset of aggregation was delayed. Figure 3.10 shows a TEM image of SnSe particles after one hour from precursor injection. The onset of aggregation is observed with some particles forming rod-like structures.



**Figure 3.10: TEM image of SnSe QDs prepared under conditions corresponding to case 3 (Table 3.2) one hour after precursor injection. Lower precursor concentrations than case 1 and 2 and higher OLA/Sn and TOP/Se molar ratios delay particle aggregation.**

In case 4, the amounts of Sn and Se precursors are further decreased and the amount of OLA is increased in comparison to TOP used in case 2. Figure 3.11 shows a comparison of the direct band gap energy of SnSe QDs corresponding to case 4 and case 2 as functions of growth time. QDs corresponding to case 4 exhibit lower band gap energy in comparison to QDs corresponding to case 2 and the same growth time after precursor injection, indicating that case 4 produces larger average particle sizes. This is most probably due to the suppressed nucleation rate because of the precursor dilution and increased OLA concentration in case 4. Fewer nuclei grow to become larger particles by surface deposition of unreacted precursors. For case 4, the rate of change of the band gap energy is similar to the one observed in case 2. The observations thus far indicate that a low OLA to TOP ratio can delay particle nucleation.

Furthermore, substituting the OLA in the growth mixture by ODE prevents particle nucleation. This indicates that the presence of OLA in the growth mixture is essential for the nucleation of SnSe particles. Alkylamine has been used in the synthesis of several quantum dot materials as an activation reagent [17, 64, 65].

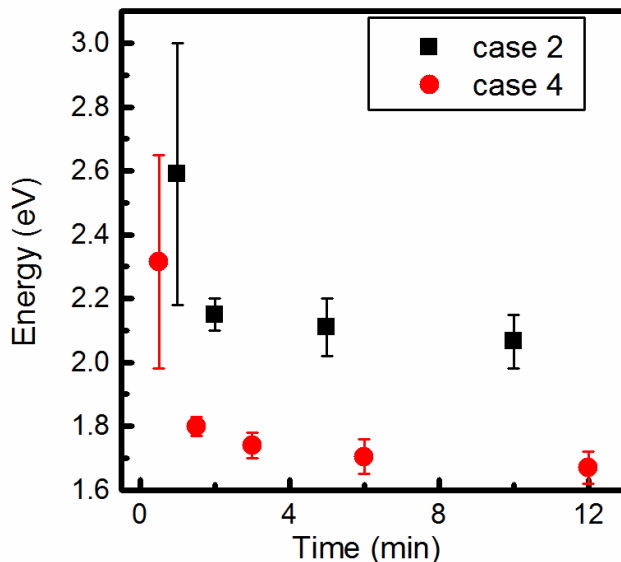


**Figure 3.11. Temporal evolution of the direct band gap energy of SnSe QDs grown under conditions corresponding to case 2 (squares) and case 4 (circles), listed in Table 3.2. Lower precursor concentrations and higher OLA/Sn ratio in case 4 lead to fewer nuclei, resulting in larger particles.**

### 3.3.5 The effect of temperature on the morphology of SnSe QDs

The effects of precursor injection and growth temperature were also studied. Case 5 corresponds to case 2 with a higher precursor injection temperature of 150 °C and growth temperature of 120-130 °C. Under such conditions, the particle growth rate was accelerated and aggregation occurred as early as 4 minutes from precursor injection (Figure 3.12). In case 6 the same conditions as in case 3 were used except for the precursor injection and growth temperatures. By setting the precursor injection temperature to 170 °C and the growth temperature to a value higher than 110 °C, particle nucleation was not observed

within the first 10 minutes of the experiment. When the growth temperature was lowered to 100-110 °C, particle nucleation and growth was observed.

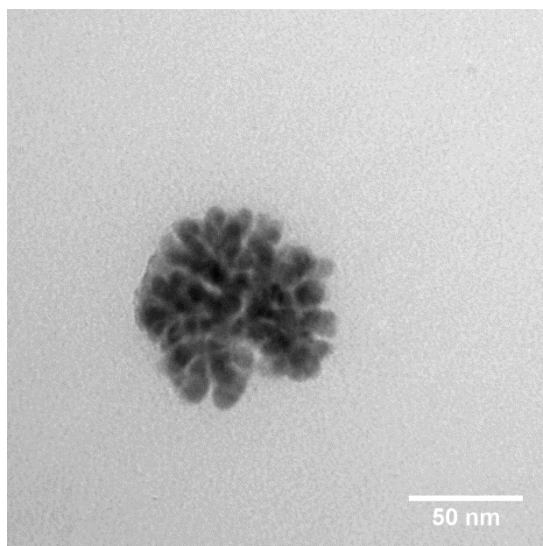


**Figure 3.12: TEM image of a SnSe aggregate obtained under conditions corresponding to case 5 (Table 3.2) and growth time of 4 min. Increasing the precursor injection and growth temperature in comparison to case 2 leads to particle aggregation at an earlier growth time.**

It appears that the nucleation rate is controlled by the precursor and the dissolution of sub-critical clusters. The rate of reaction between the precursors increases with increasing growth temperature and decreases with lower concentrations. The rate of dissolution of the clusters increases at higher temperatures. At low precursor concentrations, there is a temperature above which particle nucleation will be controlled by the high rate of cluster dissolution which limits the formation of nuclei that can grow into particles.

### 3.3.6 SnSe/ZnSe core/shell QDs

SnSe QDs were modified with MUA to make them water soluble. There are three potential issues with the mercapto ligand exchange method. First, in a preliminary experiment, the absorption of the SnSe solution would shift to larger wavelengths after the ligand exchange process (Figure 3.13), indicating the formation of aggregates. This is most likely due to the insufficient ligand protection after the purification

step. Second, the thiol ligand might etch the QDs surface [66]. Finally, the mercapto ligand passivation of the SnSe surface might be less efficient in comparison to other QD materials.

It was found that when forming a self-assembled  $\text{COOH}(\text{CH}_2)_{15}\text{SH}$  monolayer on indium-tin oxide, the carboxylic acid end preferentially adsorbs instead of the thiol end[67]. It is possible that the Sn-S bond is not strong enough to keep the mercapto ligand stable on the QD surface. A potential solution to these issues is to grow a stable inorganic shell, such as ZnSe on the bare SnSe QDs. The shell material would protect the SnSe core from etching and the thiol ligand would be preferentially anchored on the ZnSe surface by forming strong Zn-S bonds.

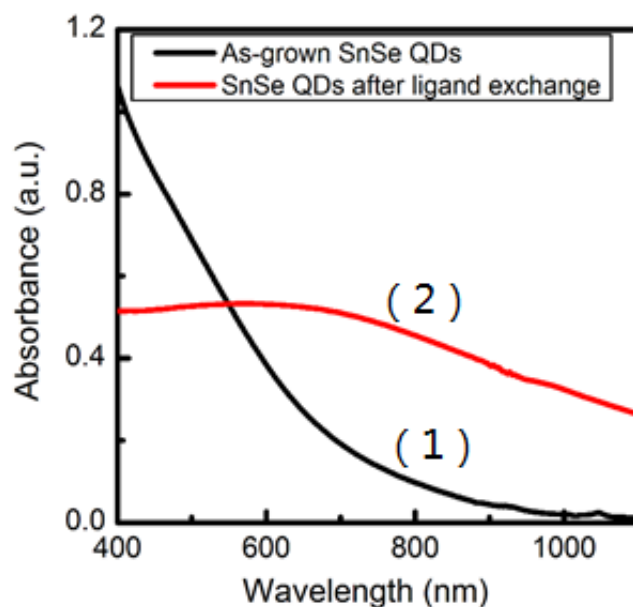


**Figure 3.13: Absorption spectra of (1) as-grown SnSe QDs dispersed in chloroform and (2) SnSe QDs dispersed in tetrahydrofuran after the ligand exchange process**

ZnSe has been used as a shell material for coating CdSe [68], InAs[69] and other QDs. The deposition of the ZnSe shell has been usually carried out at a temperature between 150 °C and 230 °C when coating II-VI and III-V QDs. However, in a preliminary experiment (Figure 3.14), the absorption

of the SnSe QDs almost disappears after annealing at 150 °C for 10 min. This is most likely due to the dissolution of the QDs. To grow a ZnSe shell on the SnSe QD cores, the temperature needed to be lower than 150 °C. Such a low temperature can lead to a low shell growth rate. To resolve this issue, an excess amount of the precursor was added to the mixture and the shell growth time was increased.

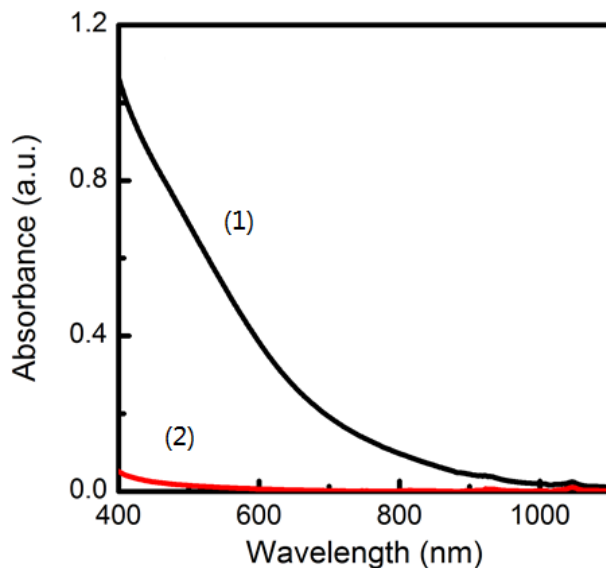


**Figure 3.14: Absorption spectra of (1) as-grown SnSe QDs; (2) SnSe QDs annealed at 150 °C for 10min.**

### 3.3.7 Surface modification of SnSe/ZnSe core/shell QDs

After the surface of the SnSe QDs was coated with a ZnSe shell, an established surface modification strategy was applied to coat the core/shell QDs with MUA [63, 70]. Figure 3.15 shows the XPS spectrum of the SnSe/ZnSe core shell QDs that are capped with MUA. The Zn3p3 and Zn3p1 peaks demonstrate the presence of Zn at and near the surface of the QDs. The S2p peak comes from the thiol group of MUA.

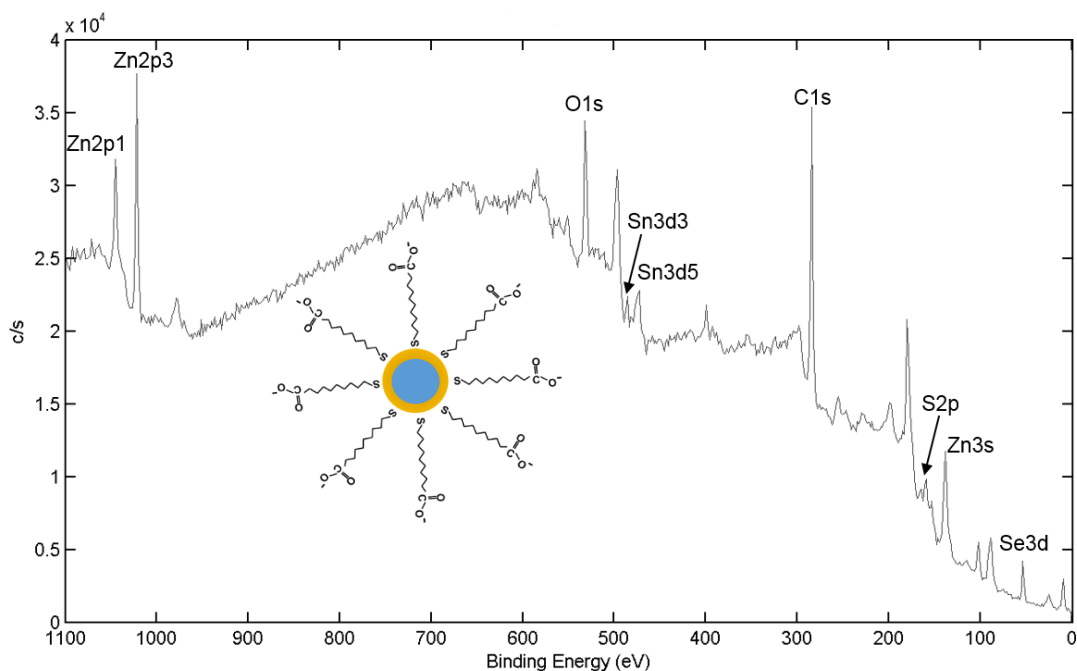


**Figure 3.15: XPS spectrum of SnSe/ZnSe core/shell QDs that are capped with MUA.**

### 3.4 Conclusions

NIR absorbing SnSe QDs with average sizes between 1.7 and 2.5 nm were synthesized in a mixture of OLA and TOP coordinating solvents using the air-stable precursors tin (II) chloride-oleylamine (OLA) complex and trioctylphosphine selenide (TOPSe), which are readily available commercially. The presence of OLA in the mixture was found to be essential for particle nucleation to occur at 135 °C and high OLA concentration enabled QD synthesis at a lower reaction temperature of 100 °C. An increased amount of TOP in the growth mixture was found to lower the nucleation rate and yield larger particles. Optimal operating conditions that prevent QD aggregation for several minutes after precursor injection were identified. This enabled the controllable synthesis of non-aggregated small SnSe QDs that were subsequently capped with a ZnSe shell. The surface of the SnSe/ZnSe core/shell QDs was modified with MUA to enable their dispersion in DI water.

## CHAPTER 4

### SYNTHESIS OF ZnSe QUANTUM DOTS IN A CONTINUOUS FLOW REACTOR

#### 4.1 Introduction

The increasing demand for quantum dots (QDs) for a variety of commercial applications, including high color definition displays, biological sensors and fluorescent tags, and photovoltaics, requires the development of efficient methods for mass production of QDs. The traditional method of synthesizing QDs using batch colloidal synthesis is operator-intensive and difficult to scale up.

Continuous flow processes have distinct advantages over batch processes when it comes to minimizing production costs. They enable high production rates from small reactor volumes, are more amenable to process automation and can improve heat and mass transfer. Microfluidic reactors using the same reacting mixtures as the ones employed in the hot injection batch process have been studied extensively for the synthesis of QDs in a continuous process [71-73]. However, controlling the particle size distribution in such systems is difficult due to broad residence time distributions that lead to polydisperse particle populations. Furthermore, the use of expensive, toxic and pyrophoric precursors increases the production cost.

The template-assisted synthesis method allows nanoparticle to be synthesized at room temperature and their size to be controlled by the precursor concentration in the dispersed nanodomains of the template [23]. This process is easy to scale up without sacrificing the narrow particle size distribution, which is controlled by the size distribution of the self-assembled nanodomains in which the particles are grown. One limitation of this technique, when used in batch mode, is the large excess of H<sub>2</sub>Se gas required. A continuous counter-current process has the potential of maximizing precursor utilization and

can be integrated with particle extraction, shell growth and annealing steps to yield highly luminescent core/shell nanocrystals.

As shown in Figure 4.1, during template-assisted growth of ZnSe QDs the H<sub>2</sub>Se gas must diffuse through the continuous p-xylene phase and block copolymer layer before reaching the aqueous nanodomain. If the flux of H<sub>2</sub>Se that enters the dispersed nanodomains of the template is not rate limiting (i.e. sufficiently high) and the rate of nucleation of ZnSe is equal to the collision rate of Zn and Se ions in the aqueous dispersed phase, Lattice Monte Carlo simulations of ZnSe cluster formation and coalescence kinetics predict a very short time (microseconds) for the formation ZnSe QDs [74, 75]. Since the solubility of H<sub>2</sub>Se in the p-xylene continuous phase of the microemulsion is very small, the mass transfer rate of H<sub>2</sub>Se from the gas bubbles to the aqueous droplets is probably the rate-limiting step in the growth of ZnSe QDs by this technique.

The template-assisted synthesis of ZnSe QDs was first performed in a batch reactor[76], where H<sub>2</sub>Se gas was bubbled through a vial containing a microemulsion having Zn precursor in the dispersed nanodroplets. The drawback of the batch reactor is the limited contacting area and time between the microemulsion and H<sub>2</sub>Se containing gas phase. This limits the mass transfer rate H<sub>2</sub>Se to the nanodroplets resulting in very low conversion of this material. A continuous counter-current process can overcome this disadvantage and add the additional advantage of high throughput from a small reactor volume. The main goal of developing the continuous process discussed in this chapter is the increase in the conversion of the toxic H<sub>2</sub>Se gas, which would greatly reduce the cost of waste treatment and raw materials.

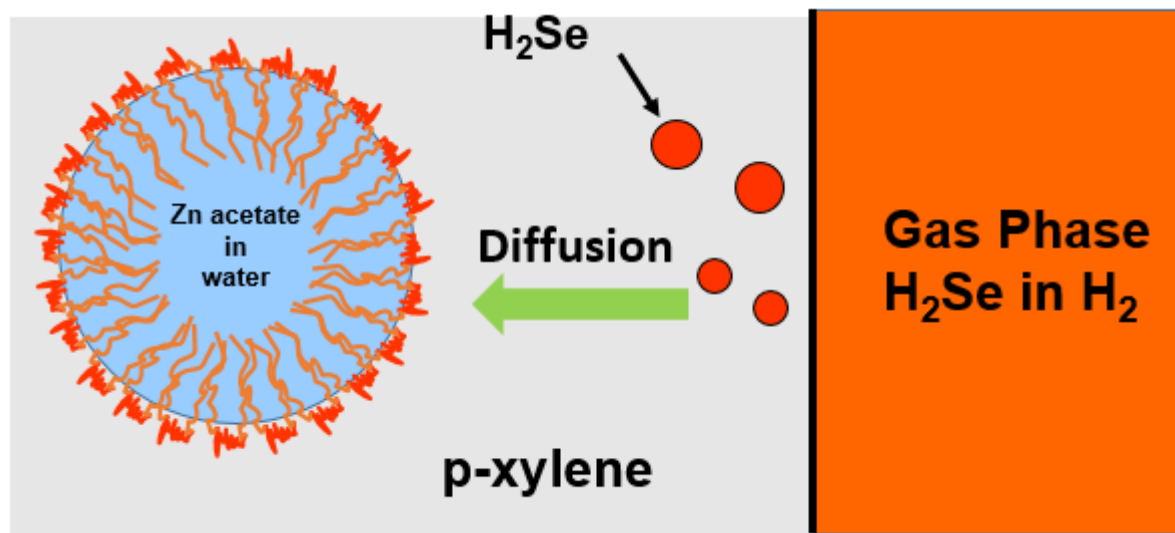


**Figure 4.1 Schematic representation of mass transfer of  $H_2Se$  gas from the gas phase to a Zn-containing aqueous nanodroplet in the microemulsion-gas synthesis method.**

## 4.2 Experimental Section

### 4.2.1 Counter current packed bed reactor design

The experimental reactor is shown schematically in Figure 4.2. The reactor is a glass column with three glass prongs in the bottom. A stainless steel sieve with mesh size of 0.8 mm was fitted to the bottom of the reactor to support the glass beads used for packing. The glass column is 203 mm in height and 24 mm in inner diameter with a total volume of approximately 90 mL. The volume between the liquid outlet and bottom of the packed bed was 40 mL. Glass beads with diameters of 3 mm, 2 mm and 1 mm were used to pack the column. The microemulsion was stored in a reservoir, whose pressure was kept at 2.5-3.5 psi by connecting it to a  $N_2$  line. The microemulsion was introduced from the top of the reactor and its flow rate was controlled using a needle valve and the pressure difference between the reservoir and the reactor column. Liquid samples were collected from the outflowing stream which was also controlled by a needle valve. The gas was introduced from the bottom of the reactor through a quartz frit gas distributor and was removed from the top of the reactor. The flow rate of the gas was controlled by a mass flow

controller. The inlet and outlet gas lines were equipped with sampling port for withdrawing gas samples using locking syringes. The schematic of the process flow diagram is shown in Appendix A.

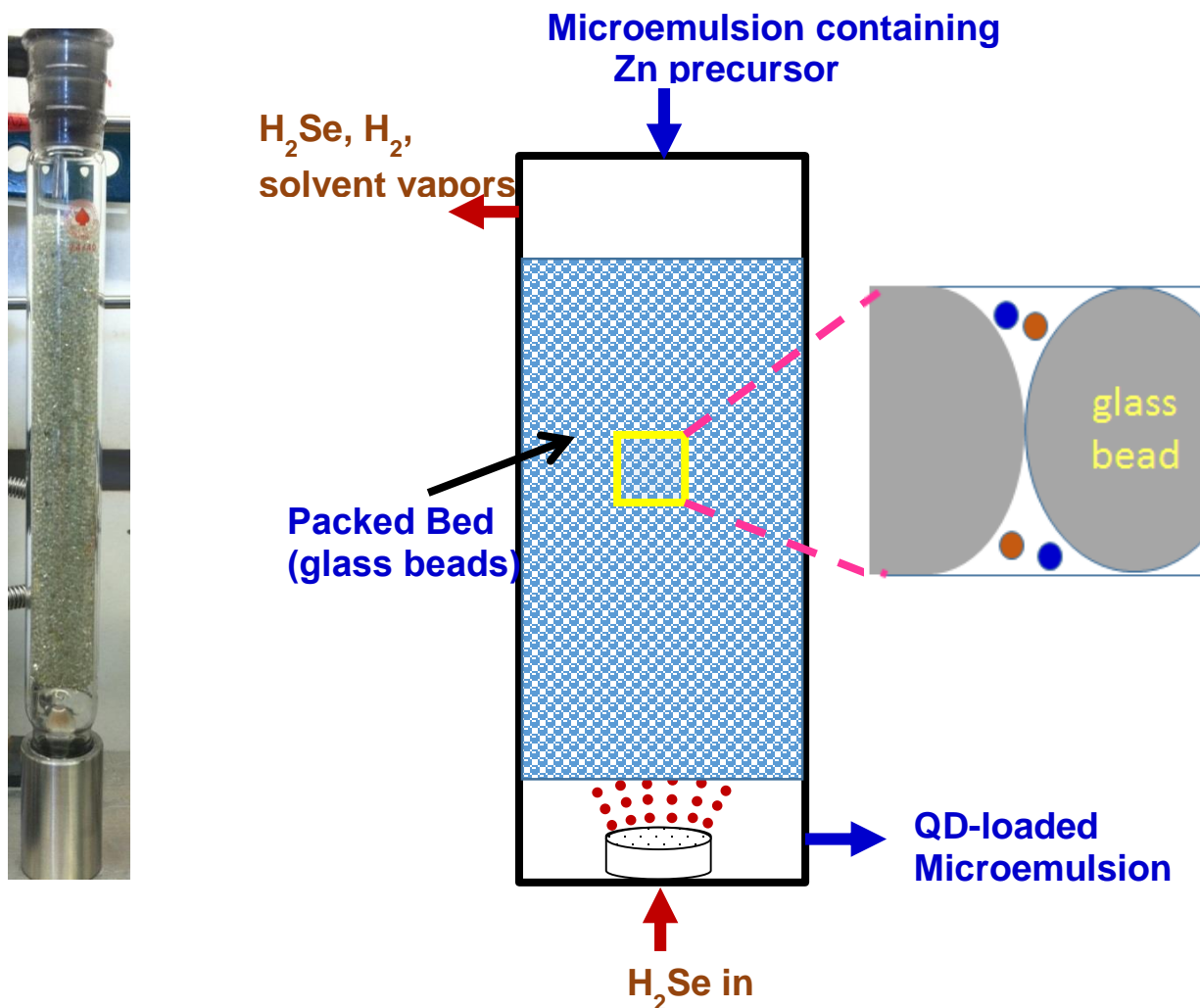


**Figure 4.2:** (a) Experimental reactor; (b) schematic drawing of the reactor.

#### 4.2.2 Preparation of the microemulsion

The microemulsion was formed by the mixing of 82.1 wt % p-xylene, 15.5 wt % Pluronic P105, and 2.4 wt % aqueous solution containing the Zn precursor. The aqueous phase consisted of a 0.3 M ZnAc solution in water. The mixture was stirred overnight to form a single transparent phase consisting of a microemulsion.

#### 4.2.2 Reactor Operation and Optimization

First the reservoir flask was filled with ~ 60 mL QDs loaded microemulsion. Both the reactor and reservoir flask were purged with N<sub>2</sub> for 15 min to remove O<sub>2</sub> from the system. Then the needle valve connected to the top of the reactor was opened so that the QDs loaded microemulsion could fill the reactor. The empty reservoir flask was subsequently filled with unreacted microemulsion and purged with N<sub>2</sub> for 15 min. After purging, H<sub>2</sub>Se gas with a flow rate of 3 sccm was bubbled through the reactor for 15 min to saturate the p-xylene phase in the microemulsion with H<sub>2</sub>Se. The pressure of the reactor was maintained at 0.5-1 psi. The microemulsion flow rate was set at 1.5 mL/min and was kept constant by monitoring the rate of increase in the fluid volume in a measuring flask collecting the outflowing liquid stream. The needle valves located at the top and bottom of the reactor were adjusted to keep the liquid level in the reactor constant and establish a steady flow of liquid through it. Samples were collected by draining some fluid into a vial connected to the liquid outlet every 10 min. After the reaction, the microemulsion flow was stopped and the gas stream was switched to N<sub>2</sub> to purge all unreacted H<sub>2</sub>Se from the reactor. The reactor was cleaned using acetone.

#### 4.2.3 Characterization of ZnSe QDs

The QD-loaded microemulsion samples were characterized using absorption and fluorescence spectroscopy. The absorption spectra of ZnSe QDs was obtained using Agilent Cary 5000 UV-Vis-NIR spectrophotometer. The photoluminescence spectra were collected using a Horiba Jobin Yvon Fluorolog-3 Spectrophotometer and an excitation wavelength of 330 nm. Gas chromatography (GC) with Plot Q column and thermal conductivity detector (TCD) was used to analyze the gas stream. Argon was used as the carried gas in the GC. The injection temperature of the gas was maintained at 250 °C, the oven temperature at 60 °C and the detector temperature at 250 °C.

## 4.3 Results and discussion

### 4.3.1 Optical properties of ZnSe QDs synthesized in the continuous flow reactor

The absorbance of a ZnSe QDs loaded microemulsion is shown in Figure 4.3. The ZnSe QDs synthesized using the microemulsion batch method had no obvious absorption peak, which could be due to high concentration of defects in the QDs.

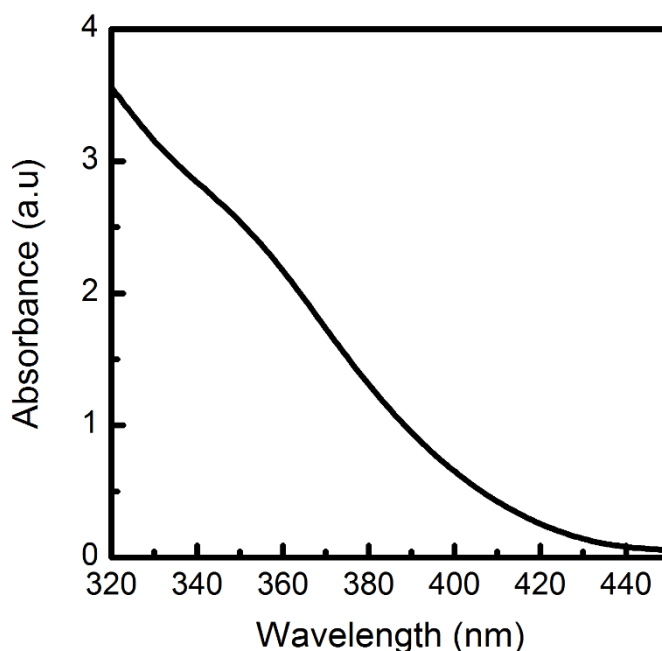


**Figure 4.3: Absorption spectra of the ZnSe QDs synthesized using the continuous flow reactor.**

The emission spectra of ZnSe QDs samples collected at different processing times are shown in Figure 4.4. All emission peaks are at 440 nm and correspond to an average particle size of 7 nm according to the peak PL wavelength vs. size correlation published by Mei et al[77]. The shoulders at around 400 nm can be attributed to the microemulsion background fluorescence. The size of the ZnSe QDs is controlled by the amount of ZnAc contained in the dispersed nanodomains (nanodroplets) of the microemulsion.

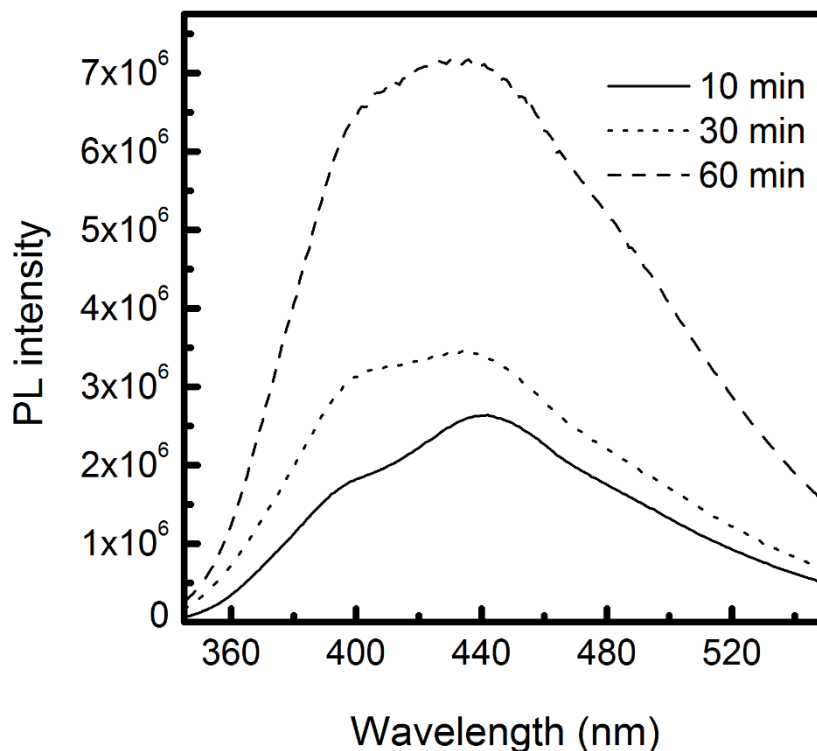


**Figure 4.4: Emission spectra of ZnSe QDs samples taken at different processing times.**

Since the average size of the ZnSe QDs are similar for different processing time, the absorbance at a certain wavelength could be used to compare the concentration of different samples. Figure 4.5 compares the absorbance at 355 nm, 370 nm and 400 nm for samples collected at different processing times. At different wavelengths, the trend of change in absorbance for different samples is maintained, suggesting that absorbance at certain wavelength could be used to represent the overall characteristic of the absorption spectrum. In the rest of this chapter, absorbance at 370 nm was used to compare the concentration of ZnSe QDs in different samples. The absorbance of the fully converted microemulsion is estimated to be around 1.4. As shown in Figure 4.6, when excess amount of H<sub>2</sub>Se is bubbled through the microemulsion at a flow rate of 3 sccm for the H<sub>2</sub>/H<sub>2</sub>Se gas stream, the absorbance of the microemulsion is initially 1.88. After storing the sample for 2 weeks, its absorbance decreased to 1.37. For another case

employing a  $H_2/H_2Se$  gas flow rate of 2 sccm, the absorbance slowly decreased from 1.45 to 1.32, which could be mostly attributed to the loss of the ZnSe QDs over time. One possible source of the absorbance increase when excess  $H_2Se$  is bubbled is the dispersion of very fine Se particles that are present in the gas tank and are too small to be captured by the inline filter used to clean the gas upstream of the reactor. These particles are dispersed in the p-xylene continuous phase and precipitate during storage to the bottom of the vial forming a layer of dark precipitate.

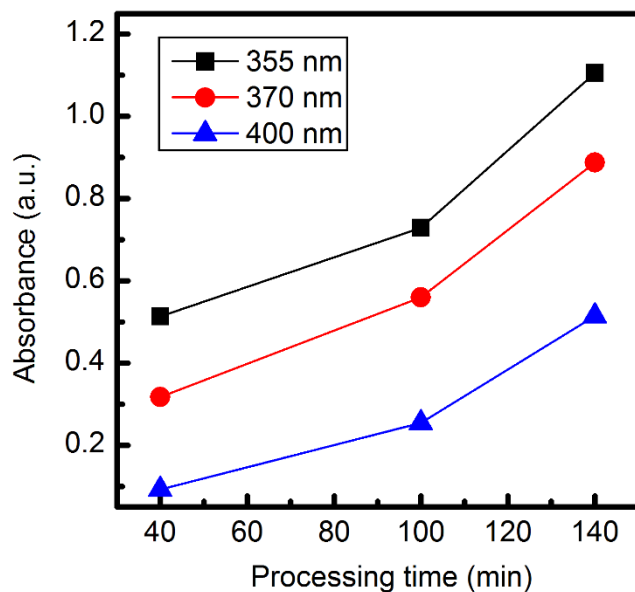


**Figure 4.5: Absorbance at 355 nm, 370 nm and 400 nm for ZnSe QD loaded microemulsion samples collected at different processing times.**

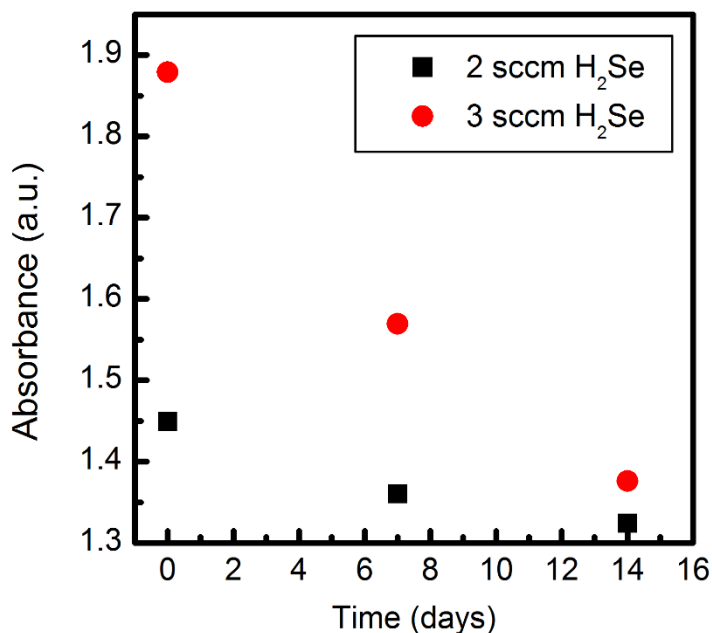


**Figure 4.6: Comparison of the time evolution of the absorbance for QDs synthesized using a gas stream flow of 2 sccm and 3 sccm H<sub>2</sub>/H<sub>2</sub>Se.**

#### 4.3.1 Optimization of operating conditions for reactor startup

Determining an efficient start-up strategy is important in order to reach steady state in a short time. Two reactor startup strategies were tested: One that started with the reactor containing unreacted microemulsion and a second that started with the reactor containing ZnSe QD loaded microemulsion.

In the first startup strategy, the reactor was loaded with unreacted microemulsion. Before starting the liquid flow, the reactor was operated under Batch Pre-Processing (BPP) mode, where H<sub>2</sub>Se was bubbled through the microemulsion at the flow rate of 4 sccm for 10 min to form ZnSe QDs. A continuous microemulsion flow was subsequently established with a rate of 1 mL/min and the H<sub>2</sub>Se gas stream flow rate was set at 1 sccm. Figure 4.7 shows the absorbance at 370 nm of the samples collected at different processing times. During 140 minutes of processing time, the absorbance increased linearly with processing time, indicating that the reactor did not reach steady state. To shorten the time required to

reach steady state, a possible method would be to increase the flow rate of  $H_2Se$  at the BPP step. However, this approach would consume a significant amount of  $H_2Se$ .

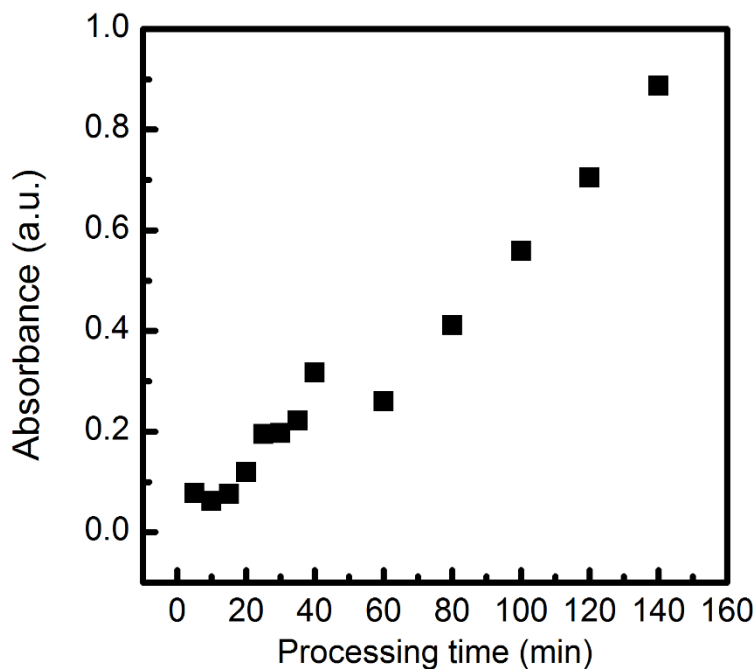


**Figure 4.7: Absorbance at 370 nm as a function of the processing time for the reaction that start with the blank microemulsion.**

A more attractive strategy is to start by filling the reactor with a QD-loaded microemulsion, followed by introduction of a continuous flow of blank microemulsion from the top of the reactor. To test this startup strategy, after filling the reactor with QD-loaded microemulsion, the unreacted microemulsion flow rate was set at 1.5 mL/min and the  $H_2/H_2Se$  flow rate was varied. Experiments with  $H_2/H_2Se$  flow rates of 1 sccm and 3 sccm was used to test the amount of  $H_2Se$  required to convert all of the ZnAc to ZnSe QDs and establish steady state.

Figure 4.8 shows the absorbance at 370 nm of samples collected while the reactor was running under this startup mode. For the case corresponding to a H<sub>2</sub>/H<sub>2</sub>Se flow rate of 3 sccm, the absorbance decreased in the first 30 min. The drop in the particle density could be due to the delay of the H<sub>2</sub>Se diffusion through the p-xylene phase. The absorbance increased after 30 min and reached a plateau as the processing time increased, which suggested that the ZnAc precursor in the microemulsion was fully converted under such conditions. For the case corresponding to a H<sub>2</sub>/H<sub>2</sub>Se flow rate of 1 sccm, the absorption decreased in the first 60 min and reached steady state afterwards, suggesting that only part of the ZnAc precursor reacted with H<sub>2</sub>Se to form ZnSe QDs.

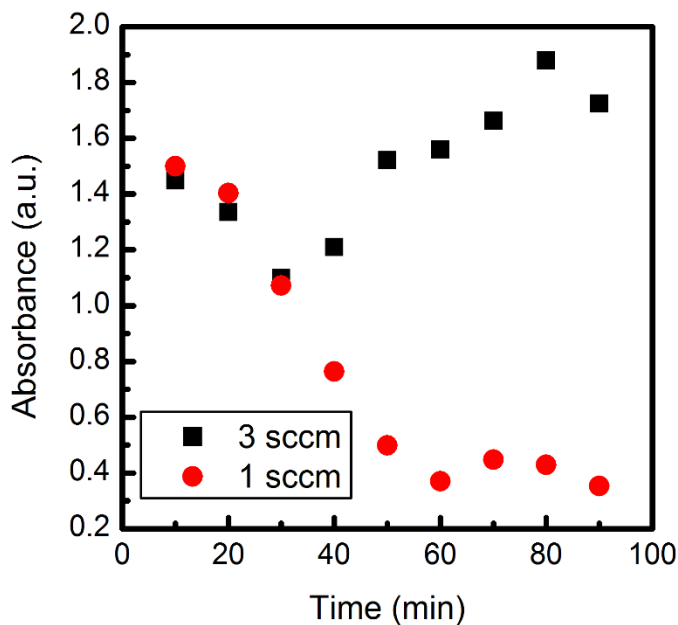


**Figure 4.8: Absorbance at 370 nm as a function of the processing time for the reaction that start with the ZnSe QDs loaded microemulsion. The flowrate of H<sub>2</sub>Se after establishing continuous flow is 1 sccm and 3sccm.**

#### 4.3.2 Effect of the packing bead diameter on QD concentration

The reactor column was packed with glass beads having diameter of 1 mm, 2 mm and 3mm in order to test the effect of packing bead size on QD formation. The corresponding open volume of the

reactor for each size of packing beads is approximately 50 mL, 60 mL and 70 mL, respectively. When the reactor was packed with 1 mm glass beads, steady continuous flow of the microemulsion could not be established so this type of packing was not used.

For the other two sizes of packing beads, the reactor was started by loading it with unreacted microemulsion and running under BPP conditions first. A continuous flow of microemulsion at 1 mL/min and a  $H_2/H_2Se$  gas flow rate of 1 sccm was subsequently established. Figure 4.9 compares the temporal evolution of the absorbance for ZnSe QDs synthesized from a reactor packed with 2 mm and 3 mm glass beads. After 40 min of processing time, the absorbance of the ZnSe QDs is higher when the packing beads size is smaller. The first 40 min correspond to the time needed to purge the initial unreacted microemulsion located below the reactor packed bed. When the packing bead size decreases the gas-liquid contacting area increases, which results in the increase in the particle concentration. The bead size of 2 mm was used in subsequent experiments as the optimal packing bead size.

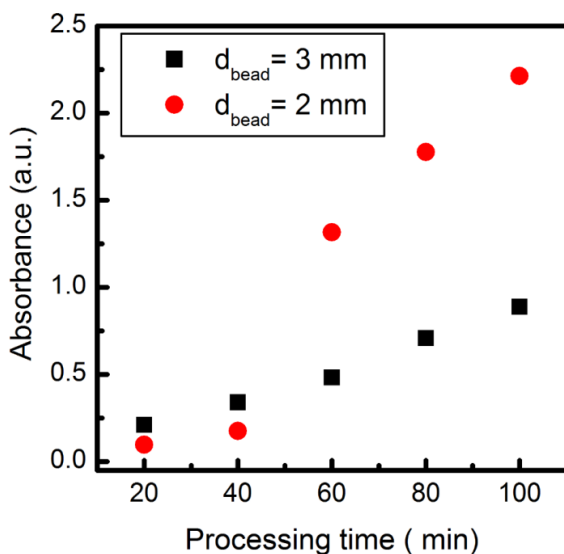


**Figure 4.9:** Absorbance at 370 nm as a function of the processing time for samples synthesized in a packed bed reactor containing a uniform size of glass beads with diameter of 3 mm and 2mm.

### 4.3.3 Optimization of operating conditions for steady state operation

The  $H_2/H_2Se$  gas flow rate was varied to explore its effects on establishing steady state operation. To further decrease the time to reach steady state,  $H_2/H_2Se$  gas with a flow rate of 3 sccm was bubbled to the reactor for 15 min after it was filled with a QDs loaded microemulsion.  $H_2/H_2Se$  gas flow rates of 1 sccm, 1.5 sccm and 2 sccm were used while the flow rate of the microemulsion was fixed at 1.5 mL/min. As shown in Figure 4.10, when the  $H_2/H_2Se$  gas flow rate is 2 sccm, the absorbance of the sample at different processing times only varies by a small amount, indicating that the reactor has reached steady state. When the gas flow rate was decreased to 1.5 sccm, the absorbance first dropped and then reached plateau after 40 min. This suggests that the reactor reaches a steady state after 40 min, but the ZnAc in the microemulsion is not fully converted to ZnSe QDs. The error bars represent the variation of data collected from two different experiments. It can be concluded that the optimal  $H_2Se$  flow rate for the conditions of this experiment is 2 sccm.

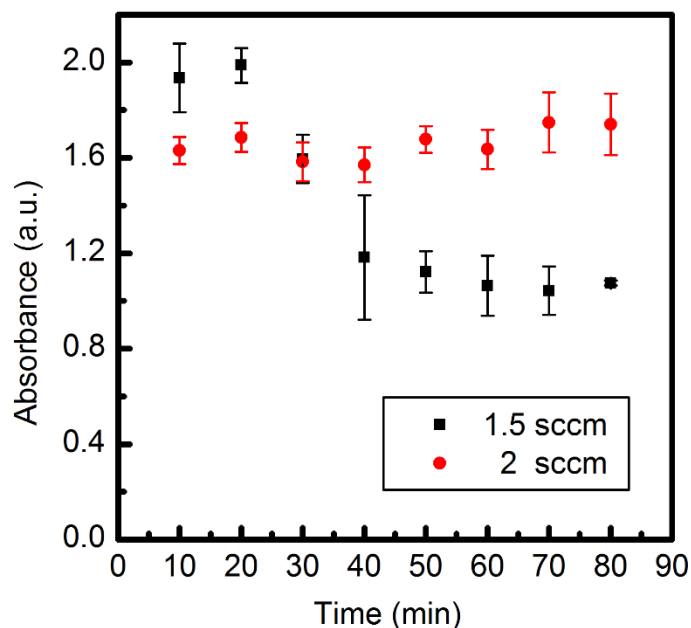


**Figure 4.10: Absorbance at 370 nm as a function of processing time from ZnSe QD-loaded microemulsion samples collected during continuous flow processing. The flow rates of the  $H_2/H_2Se$  gas streams used are: 1.5 sccm and 2 sccm.**

#### 4.3.4 Analysis of gas streams using gas chromatography

Gas samples with volume of 1 mL each were withdrawn from the inlet and outlet streams of the reactor under continuous counter-current flow conditions. The  $H_2/H_2Se$  flow rate was 1.5 sccm and the microemulsion flow rate 1.5 mL/min. The GC spectra are shown in Figure 4.11. For the sample withdrawn from the inlet of the reactor, the negative peak at 1.2 min probably corresponds to  $H_2$  as  $H_2$  form negative peak when its thermal conductivity is higher than the carrier gas argon. The peak at 1.5 min probably corresponds to residual  $N_2$  from the previous purging step. The peak at 11 min could be attributed to  $H_2Se$ . For the sample taken form the outlet of the reactor, the negative peak at 1.2 min is not prominent while the peak at 1.5 min greatly increases and the peak at 11 min disappears. It is possible that unreacted  $H_2Se$  is retained in the microemulsion and the gas in the outlet is mainly  $H_2$  and  $N_2$ .

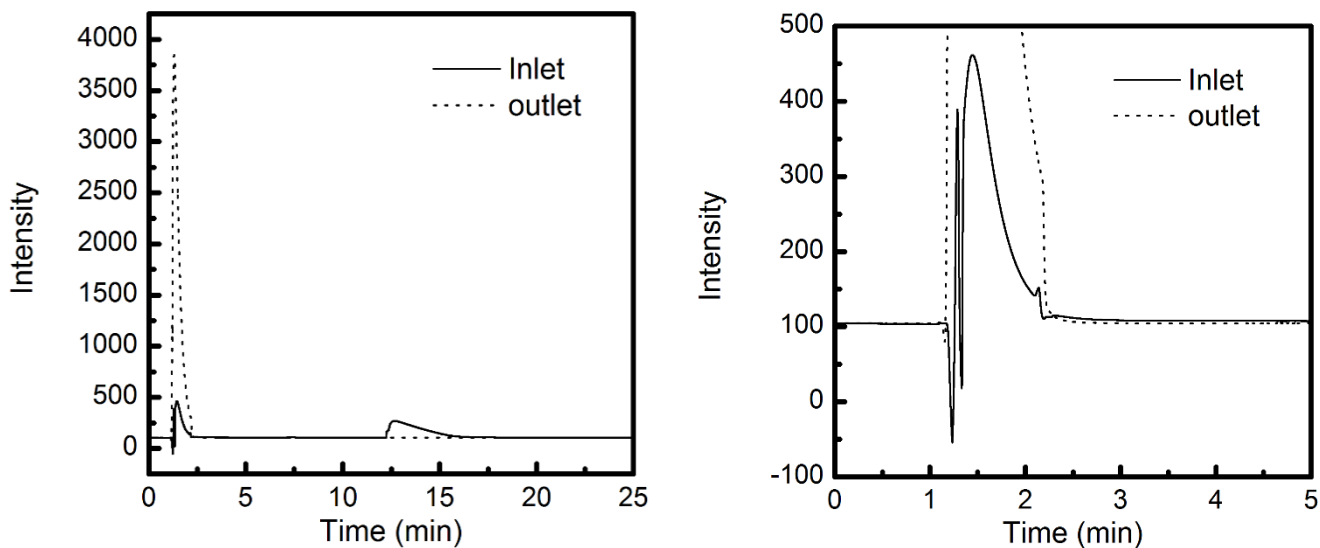


**Figure 4.11: (a) GC spectra from gas samples taken from the inlet (solid line) and outlet (dotted line) of the reactor. (b) The zoom in view of the GC spectra.**

#### 4.3.5 Effect of H<sub>2</sub>/H<sub>2</sub>Se Flow Rate on the Emission Intensity of ZnSe QDs

The as-prepared ZnSe QDs synthesized using batch processing exhibit no fluorescence and detectable emission intensity appears only after microemulsion is stored for 1 week. For ZnSe QDs synthesized in the continuous flow reactor, with the microemulsion flow rate set at 1.5 mL/min, the as-prepared QDs exhibit detectable emission when inlet gas flow rate is 1.5-3 sccm. As the gas flow rate is further increased, the emission intensity is significantly diminished. The comparison of the emission spectra for samples synthesized under H<sub>2</sub>/H<sub>2</sub>Se flow rates of 1.5 sccm and 4 sccm is shown in Figure 4.12. It is possible that the increased amount of impurities, such as Se particles, in the gas stream interferes with the light emitted from ZnSe QDs and reduces the observed emission intensity. During storage, the impurity particles precipitate from the microemulsion, and the PL emission is recovered.

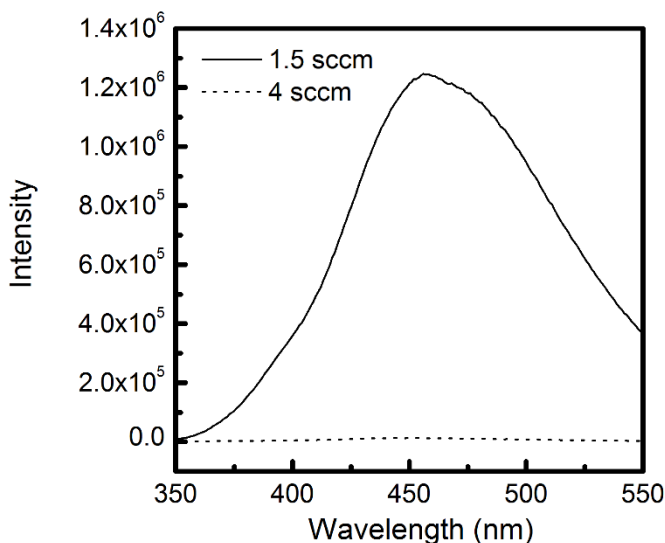


**Figure 4.12: Emission spectra of the sample synthesized under H<sub>2</sub>/H<sub>2</sub>Se flow rate of 1.5 sccm (solid line) and 4 sccm (dotted line).**

#### 4.3.6 Effect of Storing Conditions on the Stability of Microemulsion ZnSe QDs

While the as-prepared ZnSe QDs synthesized using excess amount of H<sub>2</sub>Se gas do not exhibit any fluorescence, significant fluorescence appears with time in storage and remains constant for months. It was found that for ZnSe QDs synthesized using the continuous flow reactor, the absorption and

fluorescence intensity decrease after weeks in storage when the  $\text{H}_2\text{Se}$  flow rate used in the reaction is lower than 3 sccm. When excess amount of  $\text{H}_2\text{Se}$  ( $>4$  sccm) was used, the fluorescence intensity of the particle was maintained after months of storage. It is possible that when an excess amount of  $\text{H}_2\text{Se}$  was used in the reaction, the acidic environment established in the aqueous phase prevents the decomposition of the ZnSe QDs or improves the stability of the microemulsion, thus preventing droplet-droplet coalescence and particle aggregation. To test this hypothesis, sodium bicarbonate with molar amount equal to that of the ZnAc precursor was added to the ZnSe QD-loaded microemulsion and the mixture was stirred overnight to form a homogeneous solution. After 1 day in storage, the emission of the sample was measured. As shown in Figure 4.13, after adding the sodium bicarbonate the fluorescence intensity of the ZnSe QDs decreases and the emission peak shifts to larger wavelengths. The red-shift suggested that the ZnSe QDs coalesce after introducing the base to the microemulsion. The decreased fluorescence could be due to the formation of larger particles or the decrease of the acidity in the aqueous phase.

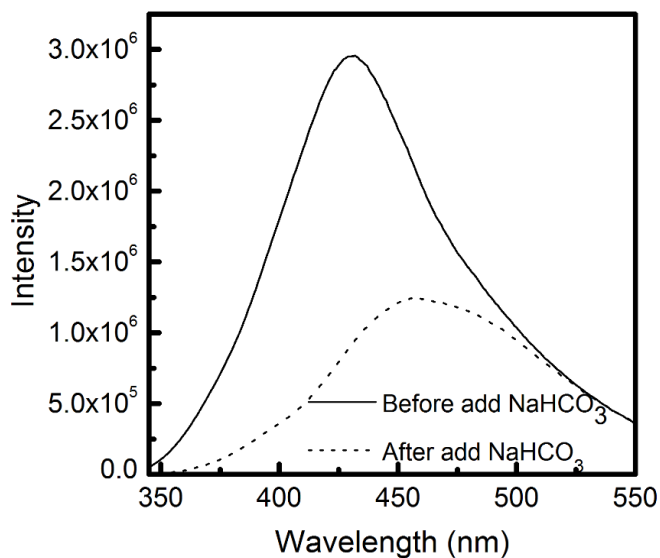


**Figure 4.13: Emission spectra of microemulsion ZnSe QDs before adding  $\text{NaHCO}_3$  (solid line) and after adding  $\text{NaHCO}_3$  (dotted line)**

#### 4.4 Conclusions

The startup and operating conditions of a continuous flow reactor were optimized. The time required for the reactor to reach steady state was significantly reduced when the reactor was started with ZnSe QD-loaded microemulsion. Packing beads with diameter of 2 mm were found to be optimal for improving the gas-liquid contacting area, while still maintaining continuous flow conditions. For batch operating conditions, the amount of H<sub>2</sub>Se/H<sub>2</sub> gas (5% H<sub>2</sub>Se in H<sub>2</sub>) required to produce 1 mg ZnSe QDs is 15 sccm. After optimizing the continuous flow conditions, the consumption of H<sub>2</sub>Se was reduced to 1 sccm per mg of ZnSe QDs. The fluorescence intensity greatly increased for the as-prepared QDs when the flow rate of H<sub>2</sub>Se was kept under 3 sccm for a microemulsion flow rate of 1.5 mL/min. However, their fluorescence emission intensity decreased with time in storage. For ZnSe QDs synthesized using excess H<sub>2</sub>Se, the fluorescence intensity was preserved during months in storage.

## CHAPTER 5

### PORTABLE TIME-DOMAIN LED FLUORIMETER FOR NANOSECOND FLUORESCENCE LIFETIME MEASUREMENTS

#### 5.1 Introduction

It has been demonstrated that MUA-capped ZnSe QDs exhibit an increase in fluorescence intensity after they are conjugated to biomolecules, such as single-stranded DNA and antibodies. The fluorescence intensity would further increase as the ssDNA on the surface of the QDs hybridizes with complementary ssDNA or the antibody binds to an antigen [63, 70]. This phenomenon enables the development of separation-free homogeneous immunoassays. Figure 5.1 illustrates the principle behind a ZnSe QD based homogeneous assay. The ZnSe QDs sensor was fabricated by conjugating the MUA capped ZnSe QDs with antibodies at 1:1 molar ratio. Two calibration lines were obtained, one corresponding to fluorescence intensity vs. ZnSe QDs sensor concentration and the second corresponding to the ZnSe QD-antibody sensor bound to the target antigen.

If the ZnSe QD biosensor is slowly added to a sample containing the target biomolecule, the fluorescence intensity of the QDs initially follows the biosensor + target calibration line and when the free target is depleted the fluorescence intensity of the sample departs from the biosensor + target calibration line and eventually merges with the biosensor only line. The concentration of the target biomolecule in the sample could be obtained from the point where the fluorescence intensity starts to depart from the biosensor + target calibration line.

The separation-free immunoassay has great potential for rapid point of care diagnostic applications. In addition to a rapid assay, point of care diagnostics also require the detection equipment to be portable and economical to manufacture. In this chapter, a ZnSe QD-based DNA biosensor was tested using a portable fluorimeter developed by the group of Prof. C. Salthouse in the Department of Electrical and Computer Engineering. The size of the portable fluorimeter is approximately equal to 3 stacked

iphone4 devices (Figure 5.2) and measures fluorescence lifetime, i.e. the rate at which light emitted from the sample decays after the excitation source is turned off.

The fluorescence lifetime is the time at which the intensity has decayed to 1/e of the original value. The decay of the intensity as a function of time is given by:

$$I_t = \alpha e^{-\frac{t}{\tau}}$$

Here  $I_t$  is the fluorescence intensity at time  $t$ ,  $\alpha$  is the pre-exponential factor, and  $\tau$  is the fluorescence lifetime. The PL decay kinetics are related to the radiative and nonradiative pathways that an exciton undergoes to achieve electron hole recombination and can be modified by changing the surface of the QD.

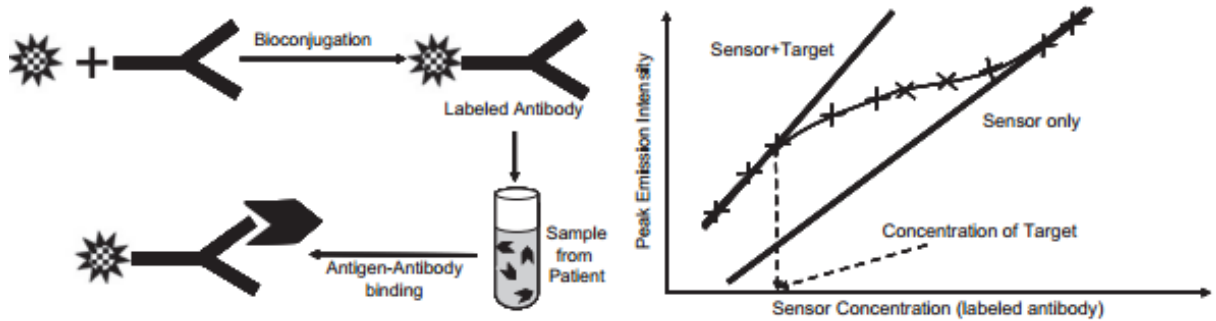


**Figure 5.1:** Schematic of the separation free homogeneous immunoassay based on ZnSe QDs[63].

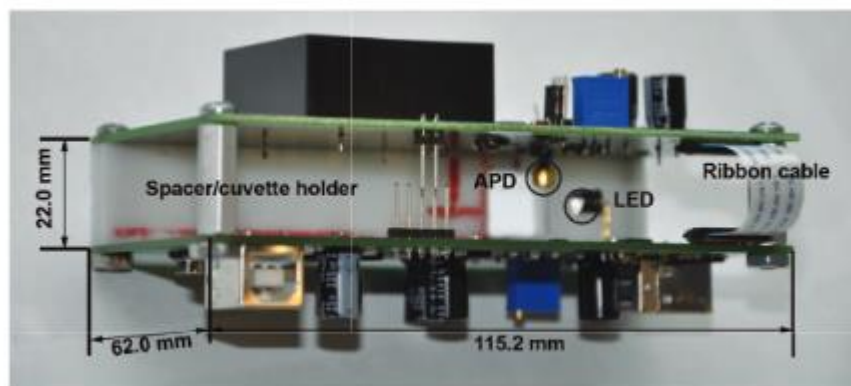


**Figure 5.2 Portable LED Fluorimeter[78] .**

## **5.2 Experimental Section**

### **5.2.1 Synthesis of ZnSe QDs**

ZnSe QDs were synthesized using the method reported by Hines[15]. Diethylzinc and selenium powder dispersed in trioctylphosphine (TOP) were injected into hot 1-hexadecylamine (HDA) at 300 °C and ZnSe QDs were grown in that mixture at 275 °C. Aliquots were extracted from the reaction mixture 20 min after precursor injection.

### **5.2.2 Surface modification of ZnSe QDs with mercaptoundecanoic acid**

The QDs were subsequently extracted from the reaction mixture, modified with 11-mercaptoundecanoic acid (MUA) and dispersed in PBS buffer using the protocol reported by Wang et al[70]. The final concentration of the MUA-capped ZnSe QDs is 2  $\mu\text{M}$ .

### **5.2.3 Bioconjugation of MUA capped ZnSe QDs with ssDNA**

QD-ssDNA conjugates were prepared by linking the carboxyl group of MUA to the amino group of amino-modified dC25 ssDNA. 5 mg of EDC was added to 1 mL MUA capped ZnSe QDs ( 2  $\mu\text{M}$  ) to activate the carboxyl group on the MUA, the solution was stirred slowly at room temperature for 30 min,

2 nM of the dC25 ssDNA was added to the mixture and incubate at room temperature for 4 hrs. The sample was stored in refrigerator for later use.

#### 5.2.4 Hybridization of ZnSe-ssDNA with complimentary ssDNA

The QDs-ssDNA conjugates were hybridized with complementary free dG25 ssDNA to obtain QD-dsDNA conjugates. 2 nM dG25 ssDNA was added to 1 mL of ZnSe-ssDNA solution (2  $\mu$ M), the mixture was kept in a 60 °C water bath for 30 min, and cool to room temperature to incubate for additional 2 hrs.

#### 5.2.5 Characterization

The fluorescence intensity was measured using a Flurolog-3 Spectrofluorometer (Horiba Jobin Yvon) with an excitation wavelength of 350 nm. All samples were subsequently analyzed using the portable time domain LED fluorimeter containing 2  $\mu$ M of ZnSe QD or ZnSe QDs-DNA conjugates in PBS buffer solution. Each sample containing ZnSe QDs was analyzed by using the LED TDF five times and the average lifetime as well as the standard lifetime error was calculated. For these measurements 365 nm LED was used to match the absorption peak wavelength of the sample (Figure 5.3)

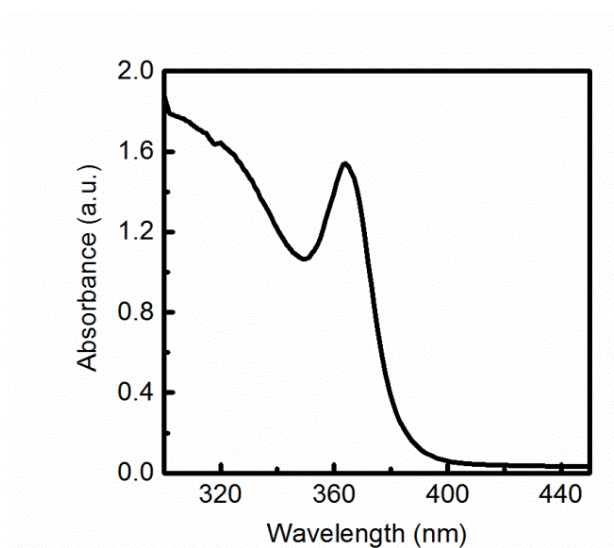


**Figure 5.3: Absorption spectra of MUA capped ZnSe Qdots dispersed in PBS buffer.**

## 5.3 Results and Discussion

### 5.3.1 Fluorescence intensity of MUA capped ZnSe QDs, ZnSe-ssDNA complex and ZnSe-dsDNA complex.

Figure 5.4 shows the fluorescent intensity of MUA capped ZnSe QDs, ZnSe-ssDNA complex and ZnSe-dsDNA complex. The peak emission wavelength of ZnSe QDs was 396 nm and their average size was estimated to be  $\sim 3$  nm using a reported correlation between QDs diameter and fluorescence emission peak wavelength. The peak emission intensity of the QDs increased by a factor of 5 after conjugation with ssDNA and by an additional factor of 1.5 after hybridization with complementary ssDNA. The increase of the fluorescence peak is attributed to the rearrangement of the capping layer and the electrostatic polar environment surrounding the QDs.

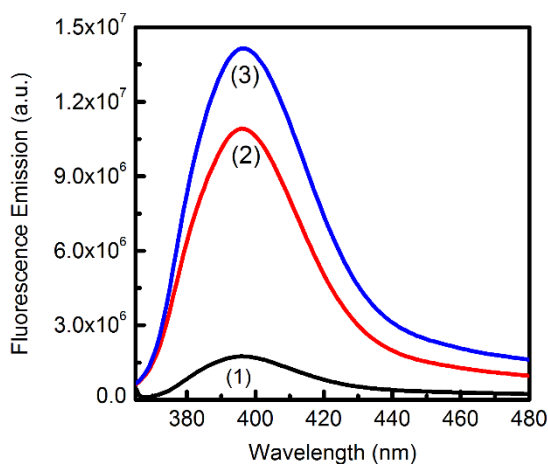


**Figure 5.4: Fluorescence emission spectra of MUA capped (1) ZnSe QDs, (2) QDs-ssDNA conjugates, and (3) QD-dsDNA conjugates dispersed in PBS buffer.**

### 5.3.2 Photoluminescence lifetime measurement of MUA capped ZnSe QDs, ZnSe-ssDNA complex and ZnSe-dsDNA complex.

Figure 5.5 shows the measured fluorescence lifetime and the corresponding error for each sample. The observed fluorescence lifetime of the QDs increased by 4 ns after conjugation with ssDNA and by an additional 2 ns after hybridization with complementary ssDNA. These changes in fluorescence lifetime

are consistent with the observed increase in peak emission intensity of the QDs after conjugation to ssDNA and dsDNA. The PL lifetime is related to the radiative and nonradiative pathways that an exciton undergoes to achieve electron hole recombination and can be modified by changing the surface environment. The changes of the ZnSe QDs surface upon conjugation to biomolecules can result in a change in PL lifetime.

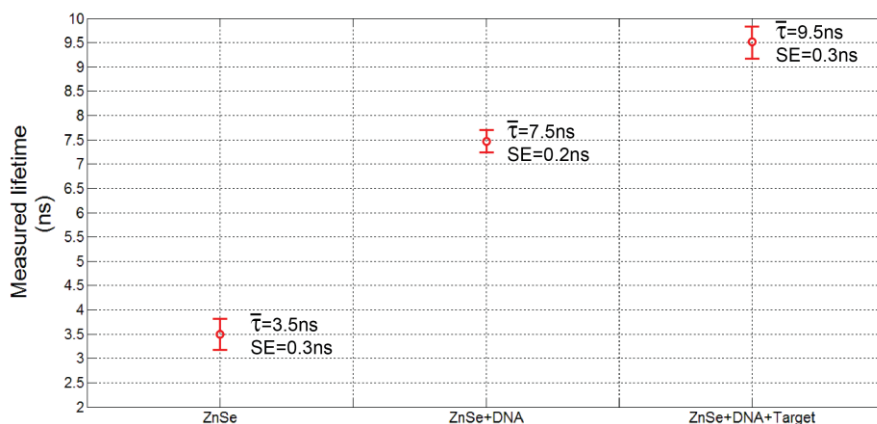


**Figure 5.5: Fluorescence lifetime of ZnSe QDs capped with MUA, conjugated with ssDNA, and conjugated with dsDNA resulting from hybridization of the ssDNA with complementary free ssDNA target.**

## 5.4 Conclusions

A ZnSe based DNA biosensor was fabricated using an established method and characterized using a novel portable LED fluorimeter. This work demonstrated that the variation in the photoluminescence lifetime could be used to detect the target biomolecule.

## CHAPTER 6

### CONCLUSIONS

This thesis focuses on the synthesis and biological applications of non-toxic Zn- and Sn-based QDs. ZnSe/ZnTe and ZnTe/ZnSe core/shell QDs were synthesized and the heterogeneous core/shell structures expanded the PL emission range of ZnSe QDs from UV-blue to the visible spectral region. To identify the most stable heterostructures of the core/shell QDs, the thermodynamic stability of ZnSe/ZnTe and ZnTe/ZnSe core/shell QDs during shell growth and thermal annealing was explored. By comparing the temporal evolution of the emission spectra and near surface composition of the core/shell structures, it was found that core/shell QDs favor the structures with a Te-rich surface. As a result, the ZnSe/ZnTe core/shell QDs are thermodynamically more stable than ZnTe/ZnSe core/shell QDs.

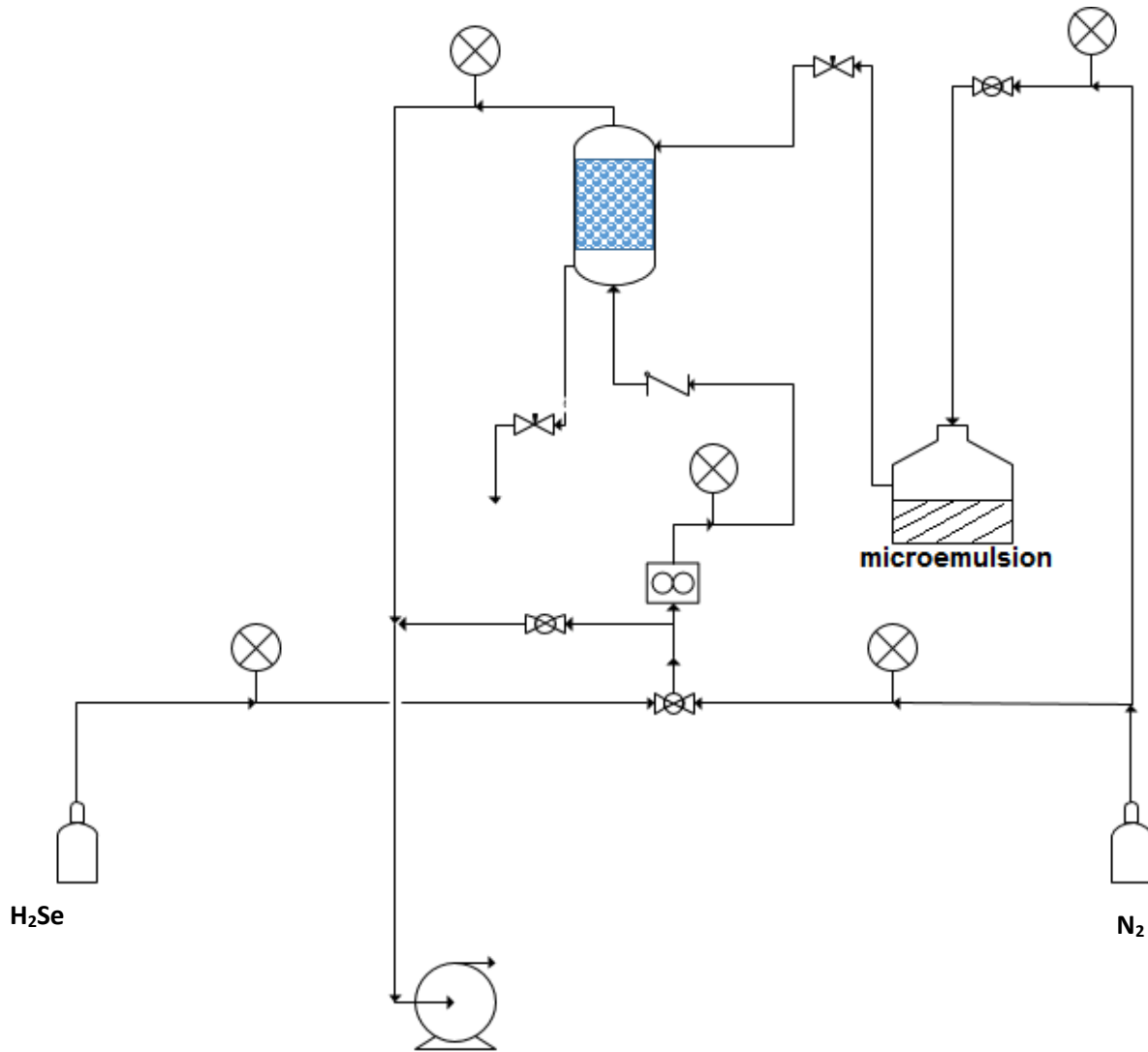
Small size (< 4nm) SnSe QDs was synthesized using an air-stable tin(II) chloride-oleylamine (OLA) complex and selenium powder dissolved in trioctylphosphine (TOP) as precursors. The growth rate and morphology of the nanocrystals were studied as functions of the processing conditions. Operating conditions that allow precise control over the final particle size and prevent particle aggregation were identified. The SnSe QDs were coated with a ZnSe shell, which enables them to be modified with 11-mercaptodecanoic acid and dispersed in aqueous solutions for biological applications.

A continuous flow pack-bed reactor was developed for the template-assisted synthesis of ZnSe QDs. The reactor startup strategy and continuous flow variables were optimized. The time required for the reactor to reach steady state is significantly reduced when the reactor is filled with a ZnSe QD-loaded microemulsion at startup. The optimal size of the packing beads was identified to improve the liquid gas contacting area and maintain a continuous flow. The H<sub>2</sub>Se conversion efficiency was improved 15 times in comparison with a batch reactor.

A ZnSe-based DNA biosensor was fabricated using an established method and characterized using a novel portable LED fluorimeter. This work demonstrated that the variation in the photoluminescence lifetime could be used to detect the target biomolecules.

# APPENDIX

## CONTINUOUS FLOW REACTOR PROCESS FLOW CHART



⊗ Pressure gauge

⊗ Ball Valve

⊗ Needle Valve

∇ Check Valve

⊞ Mass Flow Controller

## BIBLIOGRAPHY

1. Alivisatos, A.P., *Semiconductor Clusters, Nanocrystals, and Quantum Dots*. Science, 1996. **271**(5251): p. 933-937.
2. Adair, J.H., et al., *Recent developments in the preparation and properties of nanometer-size spherical and platelet-shaped particles and composite particles*. Materials Science and Engineering: R: Reports, 1998. **23**(4-5): p. 139-242.
3. Michalet, X., et al., *Quantum Dots for Live Cells, in Vivo Imaging, and Diagnostics*. Science, 2005. **307**(5709): p. 538-544.
4. Sony. *SONY ANNOUNCES 2013 BRAVIA TVS*. 2013; Available from: <https://blog.sony.com/press/sony-announces-2013-bravia-tvs/>.
5. Perry, T. *CES 2015: Placing Bets on the New TV Technologies*. 2015.
6. Nozik, A.J., et al., *Semiconductor Quantum Dots and Quantum Dot Arrays and Applications of Multiple Exciton Generation to Third-Generation Photovoltaic Solar Cells*. Chemical Reviews, 2010. **110**(11): p. 6873-6890.
7. Sargent, E.H., *Infrared photovoltaics made by solution processing*. Nat Photon, 2009. **3**(6): p. 325-331.
8. Wu, X., et al., *Immunofluorescent labeling of cancer marker Her2 and other cellular targets with semiconductor quantum dots*. Nat Biotech, 2003. **21**(1): p. 41-46.
9. Han, M., et al., *Quantum-dot-tagged microbeads for multiplexed optical coding of biomolecules*. Nat Biotech, 2001. **19**(7): p. 631-635.
10. Sun, Q., et al., *Bright, multicoloured light-emitting diodes based on quantum dots*. Nat Photon, 2007. **1**(12): p. 717-722.
11. Bailey, R.E., A.M. Smith, and S. Nie, *Quantum dots in biology and medicine*. Physica E: Low-dimensional Systems and Nanostructures, 2004. **25**(1): p. 1-12.
12. Shockley, W. and H.J. Queisser, *Detailed Balance Limit of Efficiency of p - n Junction Solar Cells*. Journal of Applied Physics, 1961. **32**(3): p. 510-519.
13. Nozik, A.J., *Quantum dot solar cells*. Physica E: Low-dimensional Systems and Nanostructures, 2002. **14**(1-2): p. 115-120.
14. Chu, M., et al., *The therapeutic efficacy of CdTe and CdSe quantum dots for photothermal cancer therapy*. Biomaterials, 2012. **33**(29): p. 7071-7083.

15. Hines, M.A. and P. Guyot-Sionnest, *Bright UV-Blue Luminescent Colloidal ZnSe Nanocrystals*. The Journal of Physical Chemistry B, 1998. **102**(19): p. 3655-3657.
16. Bang, J., et al., 2010. - **22**(- 1): p. - 240.
17. Pradhan, N. and X. Peng, *Efficient and Color-Tunable Mn-Doped ZnSe Nanocrystal Emitters: Control of Optical Performance via Greener Synthetic Chemistry*. Journal of the American Chemical Society, 2007. **129**(11): p. 3339-3347.
18. Pejova, B. and A. Tanusevski, *A Study of Photophysics, Photoelectrical Properties, and Photoconductivity Relaxation Dynamics in the Case of Nanocrystalline Tin(II) Selenide Thin Films*. The Journal of Physical Chemistry C, 2008. **112**(10): p. 3525-3537.
19. Chestnoy, N., et al., *Luminescence and photophysics of cadmium sulfide semiconductor clusters: the nature of the emitting electronic state*. The Journal of Physical Chemistry, 1986. **90**(15): p. 3393-3399.
20. Sarigiannidis, C., et al., *Vapor-Phase Synthesis and Surface Passivation of ZnSe Nanocrystals*. Journal of Nanoparticle Research, 2006. **8**(3): p. 533-542.
21. Shavel, A., N. Gaponik, and A. Eychmüller, *Efficient UV-Blue Photoluminescing Thiol-Stabilized Water-Soluble Alloyed ZnSe(S) Nanocrystals*. The Journal of Physical Chemistry B, 2004. **108**(19): p. 5905-5908.
22. Murray, C.B., D.J. Norris, and M.G. Bawendi, *Synthesis and characterization of nearly monodisperse CdE (E = sulfur, selenium, tellurium) semiconductor nanocrystallites*. Journal of the American Chemical Society, 1993. **115**(19): p. 8706-8715.
23. Georgios, N.K. and et al., *Water-based synthesis of ZnSe nanostructures using amphiphilic block copolymer stabilized lyotropic liquid crystals as templates*. Nanotechnology, 2006. **17**(13): p. 3121.
24. Cumberland, S.L., et al., *Inorganic Clusters as Single-Source Precursors for Preparation of CdSe, ZnSe, and CdSe/ZnS Nanomaterials*. Chemistry of Materials, 2002. **14**(4): p. 1576-1584.
25. Park, J., et al., *Synthesis of Monodisperse Spherical Nanocrystals*. Angewandte Chemie International Edition, 2007. **46**(25): p. 4630-4660.
26. Chan, W.C.W. and S. Nie, *Quantum Dot Bioconjugates for Ultrasensitive Nonisotopic Detection*. Science, 1998. **281**(5385): p. 2016-2018.
27. Aldana, J., Y.A. Wang, and X. Peng, *Photochemical Instability of CdSe Nanocrystals Coated by Hydrophilic Thiols*. Journal of the American Chemical Society, 2001. **123**(36): p. 8844-8850.
28. Bruchez, M., et al., *Semiconductor Nanocrystals as Fluorescent Biological Labels*. Science, 1998. **281**(5385): p. 2013-2016.
29. Dubertret, B., et al., *In Vivo Imaging of Quantum Dots Encapsulated in Phospholipid Micelles*. Science, 2002. **298**(5599): p. 1759-1762.

30. Choi, H.S., et al., *Renal clearance of quantum dots*. Nature Biotechnology, 2007. **25**(10): p. 1165-1170.
31. Walling, M.A., J.A. Novak, and J.R.E. Shepard, *Quantum Dots for Live Cell and In Vivo Imaging*. International Journal of Molecular Sciences, 2009. **10**(2): p. 441-491.
32. Xie, R., D. Battaglia, and X. Peng, *Colloidal InP Nanocrystals as Efficient Emitters Covering Blue to Near-Infrared*. Journal of the American Chemical Society, 2007. **129**(50): p. 15432-15433.
33. Hyun, B.-R., et al., *Near-Infrared Fluorescence Imaging with Water-Soluble Lead Salt Quantum Dots*. The Journal of Physical Chemistry B, 2007. **111**(20): p. 5726-5730.
34. Zhou, M. and I. Ghosh, *Quantum dots and peptides: A bright future together*. Peptide Science, 2007. **88**(3): p. 325-339.
35. van Embden, J., et al., *Review of the Synthetic Chemistry Involved in the Production of Core/Shell Semiconductor Nanocrystals*. Australian Journal of Chemistry, 2007. **60**(7): p. 457-471.
36. Kim, S., et al., *Type-II Quantum Dots: CdTe/CdSe(Core/Shell) and CdSe/ZnTe(Core/Shell) Heterostructures*. Journal of the American Chemical Society, 2003. **125**(38): p. 11466-11467.
37. Dabbousi, B.O., et al., *(CdSe)ZnS Core-Shell Quantum Dots: Synthesis and Characterization of a Size Series of Highly Luminescent Nanocrystallites*. The Journal of Physical Chemistry B, 1997. **101**(46): p. 9463-9475.
38. Li, J.J., et al., *Large-Scale Synthesis of Nearly Monodisperse CdSe/CdS Core/Shell Nanocrystals Using Air-Stable Reagents via Successive Ion Layer Adsorption and Reaction*. Journal of the American Chemical Society, 2003. **125**(41): p. 12567-12575.
39. Santra, P.K., et al., *Investigation of the Internal Heterostructure of Highly Luminescent Quantum Dot-Quantum Well Nanocrystals*. Journal of the American Chemical Society, 2008. **131**(2): p. 470-477.
40. Borchert, H., et al., *Investigation of ZnS Passivated InP Nanocrystals by XPS*. Nano Letters, 2001. **2**(2): p. 151-154.
41. Panda, S.K., et al., *Graded alloyed CdZnSe nanocrystals with high luminescence quantum yields and stability for optoelectronic and biological applications*. Journal of Materials Chemistry, 2011. **21**(31).
42. Lee, H., P.H. Holloway, and H. Yang, *Synthesis and characterization of colloidal ternary ZnCdSe semiconductor nanorods*. Journal of Chemical Physics, 2006. **125**(16).
43. Lu, W., et al., *Synthesis of Core/Shell Nanoparticles of Au/CdSe via Au-Cd Bialloy Precursor*. Langmuir, 2005. **21**(8): p. 3684-3687.
44. Xie, R.G., X.H. Zhong, and T. Basche, *Synthesis, characterization, and spectroscopy of type-II core/shell semiconductor nanocrystals with ZnTe cores*. Advanced Materials, 2005. **17**(22): p. 2741-+.

45. Turcosandroff, F.S., et al., *MOLECULAR-BEAM EPITAXY OF ZNSEI-XTEX TERNARY ALLOYS*. Applied Physics Letters, 1991. **58**(15): p. 1611-1613.
46. Brasil, M., et al., *EVOLUTION OF THE BAND-GAP AND THE DOMINANT RADIATIVE RECOMBINATION CENTER VERSUS THE COMPOSITION FOR ZNSEI-XTEX ALLOYS GROWN BY MOLECULAR-BEAM EPITAXY*. Applied Physics Letters, 1991. **58**(22): p. 2509-2511.
47. Ivanov, S.A., et al., *Type-II Core/Shell CdS/ZnSe Nanocrystals: Synthesis, Electronic Structures, and Spectroscopic Properties*. Journal of the American Chemical Society, 2007. **129**(38): p. 11708-11719.
48. Zhong, X., et al., *Composition-Tunable ZnxCd1-xSe Nanocrystals with High Luminescence and Stability*. Journal of the American Chemical Society, 2003. **125**(28): p. 8589-8594.
49. Powell, C.J. and A. Jablonski, *NIST Electron Inelastic-Mean-Free-Path Database - Version 1.2*. 2010, Gaithersburg, MD: National Institute of Standards and Technology.
50. Plass, R., et al., *Quantum Dot Sensitization of Organic-Inorganic Hybrid Solar Cells*. Journal of Physical Chemistry B, 2002. **106**(31): p. 7578-7580.
51. Lee, H., et al., *PbS and CdS Quantum Dot-Sensitized Solid-State Solar Cells: "Old Concepts, New Results"*. Advanced Functional Materials, 2009. **19**(17): p. 2735-2742.
52. McDonald, S.A., et al., *Solution-processed PbS quantum dot infrared photodetectors and photovoltaics*. Nat Mater, 2005. **4**(2): p. 138-142.
53. Konstantatos, G. and E.H. Sargent, *Colloidal Quantum Dot Photodetectors*. Infrared Physics & Technology, 2011. **54**(3): p. 278-282.
54. Lambert, T.N., et al., *Water-Soluble Germanium(0) Nanocrystals: Cell Recognition and Near-Infrared Photothermal Conversion Properties*. Small, 2007. **3**(4): p. 691-699.
55. Franzman, M.A., et al., *Solution-Phase Synthesis of SnSe Nanocrystals for Use in Solar Cells*. Journal of the American Chemical Society, 2010. **132**(12): p. 4060-4061.
56. Baumgardner, W.J., et al., *SnSe Nanocrystals: Synthesis, Structure, Optical Properties, and Surface Chemistry*. Journal of the American Chemical Society, 2010. **132**(28): p. 9519-9521.
57. Vaughn, D.D., S.-I. In, and R.E. Schaak, *A Precursor-Limited Nanoparticle Coalescence Pathway for Tuning the Thickness of Laterally-Uniform Colloidal Nanosheets: The Case of SnSe*. ACS Nano, 2011. **5**(11): p. 8852-8860.
58. Li, L., et al., *Single-Layer Single-Crystalline SnSe Nanosheets*. Journal of the American Chemical Society, 2013. **135**(4): p. 1213-1216.
59. Ma, L.L., et al., *The Fabrication of SnSe/Ag Nanoparticles on TiO<sub>2</sub> Nanotubes*. Materials Science and Engineering: B, 2013. **178**(1): p. 77-82.

60. Li, Z., et al., *Synthesis of Colloidal SnSe Quantum Dots by Electron Beam Irradiation*. Radiation Physics and Chemistry, 2011. **80**(12): p. 1333-1336.
61. Ning, J., et al., *Shape and size controlled synthesis and properties of colloidal IV-VI SnSe nanocrystals*. CrystEngComm, 2011. **13**(12): p. 4161-4166.
62. Wang, J., et al., *Detection of DNA Hybridization via Fluorescence Intensity Variations of ZnSe-DNA Quantum Dot Biosensors*. Analytical Letters, 2012. **45**(2/3): p. 227-241.
63. Wang, J. and T.J. Mountziaris, *Homogeneous Immunoassays Based on Fluorescence Emission Intensity Variations of Zinc Selenide Quantum Dot Sensors*. Biosensors and Bioelectronics, 2013. **41**(0): p. 143-149.
64. Li, L.S., et al., *High Quality ZnSe and ZnS Nanocrystals Formed by Activating Zinc Carboxylate Precursors*. Nano Letters, 2004. **4**(11): p. 2261-2264.
65. Jin, X., et al., *Shape Control of CdTe Nanocrystals Synthesized in Presence of in situ Formed CdO Particles*. Journal of Nanoparticle Research, 2011. **13**(12): p. 6963-6970.
66. Breus, V.V., C.D. Heyes, and G.U. Nienhaus, *Quenching of CdSe-ZnS Core-Shell Quantum Dot Luminescence by Water-Soluble Thiolated Ligands*. The Journal of Physical Chemistry C, 2007. **111**(50): p. 18589-18594.
67. Yan, C., et al., *Preparation and Characterization of Self-Assembled Monolayers on Indium Tin Oxide*. Langmuir, 2000. **16**(15): p. 6208-6215.
68. Reiss, P., J. Bleuse, and A. Pron, *Highly Luminescent CdSe/ZnSe Core/Shell Nanocrystals of Low Size Dispersion*. Nano Letters, 2002. **2**(7): p. 781-784.
69. Cao and U. Banin, *Growth and Properties of Semiconductor Core/Shell Nanocrystals with InAs Cores*. Journal of the American Chemical Society, 2000. **122**(40): p. 9692-9702.
70. Wang, J., et al., *DETECTION OF DNA HYBRIDIZATION VIA FLUORESCENCE INTENSITY VARIATIONS OF ZnSe-DNA QUANTUM DOT BIOSENSORS*. Analytical Letters, 2012. **45**(2-3): p. 227-241.
71. Pumera, M., *Nanomaterials meet microfluidics*. Chemical Communications, 2011. **47**(20): p. 5671-5680.
72. Zhao, C.-X., et al., *Nanoparticle synthesis in microreactors*. Chemical Engineering Science, 2011. **66**(7): p. 1463-1479.
73. Zhao, Y., et al., *Microfluidic Generation of Multifunctional Quantum Dot Barcode Particles*. Journal of the American Chemical Society, 2011. **133**(23): p. 8790-8793.
74. Kuriyedath, S.R., et al., *Lattice Monte Carlo Simulation of Cluster Coalescence Kinetics with Application to Template-Assisted Synthesis of Quantum Dots*. Industrial & Engineering Chemistry Research, 2010. **49**(21): p. 10442-10449.

75. Kuriyedath, S.R., et al., *Lattice Monte Carlo Simulation of Semiconductor Nanocrystal Synthesis in Microemulsion Droplets*. Langmuir, 2010. **26**(13): p. 11355-11362.
76. Georgios, N.K., et al., *Templated synthesis of ZnSe nanostructures using lyotropic liquid crystals*. Nanotechnology, 2005. **16**(10): p. 2372.
77. Mei, B.C., et al., *Dilution effects on the photoluminescence of ZnSe quantum-dot dispersions*. Applied Physics Letters, 2008. **93**(8): p. 083114.
78. Wang, H., et al., *A portable time-domain LED fluorimeter for nanosecond fluorescence lifetime measurements*. Review of Scientific Instruments, 2014. **85**(5): p. 055003.